Assessment of Mixing in Static Mixer Using Mean Age Theory

by

Kanishk Patel

A thesis submitted in partial fulfillment of the requirements for the degree of

Master of Science

Department of Mechanical Engineering
University of Alberta

© Kanishk Patel, 2021

Abstract

Static mixers are in-line motionless devices placed into a pipe to promote blending of miscible fluids or dispersion of immiscible liquids. These inserts are characterized by the mixing performance and the pressure drop they create. New designs of static mixers are continuously proposed to meet certain requirements of the final product. Instead of manufacturing prototypes of different designs and conducting costly experiments to assess the characteristics of inserts, it is suggested to use computational fluid dynamics (CFD) to visualize and quantify the performance of new insert designs. In this study, we demonstrate how CFD can be efficiently used to assess mixing via mean age theory for turbulent flow across a six element Kenics mixer.

In this study, the mixing assessment of the Kenics mixer was performed by evaluating the mean age distribution for a range of Reynolds numbers between 1 and 12 000 covering laminar, and turbulent flow regimes. Scalar plots of mean age were analyzed for each Reynolds number. Special emphasis was placed on the analysis of the turbulent flows. The frequency distribution of mean age was also evaluated at various cross-sections within the mixer for different Reynolds numbers. The surface average distribution of mean age revealed multi-modal distributions of the mean age for turbulent flows. Different visualisation techniques and a machine learning model (Gaussian Mixture Model) was used to find the Gaussian curves constituting the multi-modal distribution. The visualisation techniques pertaining to the field of data science were introduced into the field of CFD to allow for deeper insights.

‘Measure what is measurable, and make measurable what is not so‘

-Galileo Galilei

Acknowledgements

I feel deeply indebted to a great many people who have greatly inspired and supported me during my master's degree at the University of Alberta and the writing of this thesis. In particular, I would like to thank my promoter, Dr. Alexandra Komrakova for her invaluable guidance, encouragement, academic stimulus and generous help. From the inception to its completion, Dr. Komrakova has devoted so much into my study. I will always remember her encouragement to write and properly document everything before I dive deep into the rabbit hole with no end. Whenever I was stuck in the rabbit hole because of my immature visions of grandeur from very simplistic ideas she would pull me out and encouraged me to document the idea, vision and path to avoid getting stuck again. I will not forget those enjoyable and illuminating discussions that have led me to the final completion of this thesis. From Dr. Komrakova I have learned the art of management and writing along with the process of pursuing research in the field of Fluid Mechanics.

My gratitude also goes to Department of mechanical engineering at the University of Alberta for giving me this opportunity to pursue research. I am also grateful for the financial support provided by the Natural Sciences and Engineering Research Council of Canada (NSERC) and the support provided by the Westgrid (www.westgrid.ca) and Compute Canada (www.computecanada.ca) which enabled in part the numerical simulations.

I owe hugely to my dear parents, Navanit Patel and Jyoti Patel. Their permanent love and confidence in me have encouraged me to go ahead in my study and career. I also am thankful to my sister who always stood by me whenever I needed support.

Table of Contents

List of Tables

List of Figures

List of Symbols

Constants

ΔP	pressure drop across the mixer (Pa)
$\dot{m}$	mass flow rate (kg/s)
$\tilde{\mathbf{n}}$	normal direction vector
$\tilde{\mathbf{x}}$	position vector (mm)
$\mathbf{u}^{'}$	fluctuating velocity (m/s)
$\mathbf{U}$	mean velocity vector(m/s)
$\mathcal{D}$	diffusivity coefficient
$\overline{a}$	surface average of mean age across an $x - y$ plane (s)
$\overline{k}$	volume averaged turbulent kinetic energy (m^2/s^2)
τ_w	wall shear stress (Pa)
θ	tangential coordinate
$\tilde{a}$	age of molecules (s)
$\tilde{E}$	frequency distribution of age of molecules
$\vec{u}$	instantaneous velocity vector (m/s)
a	mean age (s)
AR	aspect ratio of Kenics element
C	concentration (kg)

CoV	coefficient of variance
D	diameter of pipe (mm)
$E(t)$	residence time distribution ($\frac{1}{s}$)
$F(t)$	cumulative residence time distribution ($\frac{1}{s}$)
g_s	surface based frequency distribution of mean age (1/s)
k	turbulent kinetic energy (m^2/s^2)
L	length of kenics mixer (mm)
L_e	length of kenics element (mm)
N	Number of grid elements
P	pressure (Pa)
Q_{in}	volume flow rate (m^3/s^2)
r	radius coordinate (mm)
Re	Reynolds number
s_k	skewness of residence time distribution
t	time (s)
U	velocity magnitude (m/s
U_{in}	inlet velocity (m/s)
U_{tan}	tangential velocity (m/s)
U_z	axial velocity (m/s)
w	thickness of kenics element (mm)
x	spatial coordinate (mm)
y	spatial coordinate (mm)
y^+	dimensionless wall distance

z spatial coordinate (mm)

Greek

α Wall proximity sensitive quantity

γ_2 variance of residence time distribution (s^2)

μ dynamic viscosity ($\mathrm{Pa \cdot s}$)

μ_t maximum turbulent viscosity ($\mathrm{Pa \cdot s}$)

μ_t turbulent viscosity ($\mathrm{Pa \cdot s}$)

$\overline{\alpha_e}$ average molecular age at outlet (s)

$\overline{\alpha_z}$ average molecular age on a $x - y$ plane (s)

$\bar{\varepsilon}$ volume averaged turbulent dissipation rate ($\mathrm{m^2/s^2}$)

ϕ Ratio of wall normal Reynolds stress to turbulent kinetic energy

ρ density ($\mathrm{kg/m^3}$)

σ_a^2 variance of mean (s)

σ_m molecular Schmidt number ($\mathrm{m^2/s}$)

σ_t turbulent Schmidt number ($\mathrm{m^2/s}$)

τ_m mean residence time distribution (s)

ε turbulent dissipation rate ($\mathrm{m^2/s^2}$)

Chapter 1

Introduction

Static mixers are motionless in-line inserts widely used in continuous processes as an alternative to mechanical agitators [1]. Compared to conventional agitators, they allow achieving similar or better mixing performance within less time and at a lower cost. Typically, several inserts are placed in-line and housed in a pipe. The geometries of these inserts are designed to promote the radial redistribution of the passing fluids, thereby enhancing mixing. Since the power requirement is limited to overcoming the pressure drop across the mixer length, these mixers in certain cases require lower energy consumption than, for instance, stirred tanks [2]. Also, the absence of moving parts leads to lower or no maintenance costs. As a result, a wide variety of static mixer designs have been proposed in order to meet certain mixing requirements in a specific application. Guidelines on how to select a proper static mixer for a specific process at given flow conditions can be found in Refs. [3], [4].

Regardless of a broad range of available static mixer designs, new designs are being actively developed to ensure high levels of mixing in novel applications (Ref. [5] and references within). Optimization of the proposed design is traditionally performed experimentally by trial and error considering previous experience [1]. Experimental investigation of each iteration of insert geometry can be time-consuming, expensive, and environmentally unfriendly (disposal of fluids and material of mixer prototypes) [3]. As an alternative and powerful addition to experimental investigation, numerical simulations using computational fluid dynamics (CFD) can be efficiently used to assess and optimize the mixing performance of proposed designs of static mixers and identify optimum operating conditions.

There are a number of studies on CFD simulations of static mixers that focus on laminar flow regime [6]–[8]. However, open literature lacks publications presenting CFD assessment of mixing effectiveness of static mixers in the turbulent regime. A numerical study by Lang *et al.* [9] reported the analysis of mixing process in the SMV static mixer at the Reynolds number of 426 000. This study is among the first that demonstrates the power of numerical simulations to gain deeper insight into the flow and mixing in static mixers. Van Wageningen *et al.* [8] assessed the capabilities of various CFD methods to study the dynamic flow in a Kenics mixer. The authors presented the results in terms of velocity profiles, power spectra, and flow structures for a range of Reynolds numbers from 10 to 1000. A general correlation for pressure drop across a Kenics mixer was proposed by Song and Han [10] using data generated by CFD simulations. Numerical simulations of turbulent flow in an industrial helical static mixer was performed by Rahmani *et al.* [11]. This study primarily shows how to extract information useful for mixing assessment. Flow patterns and mixing behavior of Kenics mixer were studied numerically by Kumar *et al.* [12]. The authors investigated the effect of the flow rate and the number of mixer elements on the hydrodynamics and pressure drop predictions over Reynolds numbers ranging from 1-25 000. Turbulent mixing and residence time distribution in high-efficiency vortex (HEV) mixers were studied using CFD by Habchi *et al.* [13] for the Reynolds numbers from 7500 to 15 000. Coroneo *et al.* [14] performed CFD simulations of corrugated static mixers for turbulent applications. A vigorous assessment of the adopted CFD approach was presented including analysis and validation of velocity profiles, turbulent quantities, and mixing effectiveness. A series of publications reporting on experimental and CFD studies of the pressure drop [15], the residence time distribution [16], and the mixing homogeneity [17] are available for selected static mixers operated in laminar and turbulent flow regimes. Based on the results of CFD simulations, Medina *et al.* [18] proposed a novel parameter (the M-number) to evaluate the performance of static mixers for turbulent applications.

The assessment of a mixer design typically involves characterization of the pressure drop across the mixer, flow patterns and structures, turbulence characteristics and evaluation of the temporal and spatial mixing effectiveness [3]. For the case of miscible liquids, which is a focus of the present study, spatial mixing refers to the homogeneity of the sample of fluid across a given cross-section and is often referred to as radial mixing [4]. The temporal mixing refers to the time spent by a molecule within the system and determines the mixing of fluid in the axial direction [19]. For closed systems (systems with singular inlet and outlet), spatial mixing can be quantitatively determined by the striation thickness in laminar flows [7] and by the coefficient of variation in turbulent flows [4]. When a novel insert design is being developed, experimental assessment of mixing at the stage of prototype development can be substantially improved by CFD simulations [11]. Building on these past works, the major goal of this thesis is to show how mean age theory can be used to quantitatively and qualitatively assess mixing performance of novel mixer designs that should operate in the turbulent regime.

1.1 Definition of Mixing

The first published quantitative assessment of mixing can be dated back to Danckwerts [20]. Since then a lot has changed and over the years many new concepts and parameters to assess mixing have been developed and validated. Though a recent publication by Kukukova *et al.* [21] highlights that the field of industrial mixing lacks a single rigorous definition of mixing which can be evaluated by experiments and quantified by theories and equations. Kukukova *et al.* [21] establishes that mixing can be appropriately assessed by determining three dimensions of mixing, namely being intensity of segregation, scale of segregation and the rate of change of segregation. The first dimension focuses on the instantaneous variation in the concentration. The second dimension defines the instantaneous length scales of the mixing and the third dimension defines the rate of reduction in segregation or increase in clustering of minor species. Recently Montante *et al.* [22] performed a quantitative analysis of mixing on SMV static mixer using CFD by assessing parameters that define mixing in three dimensions.

In the current study we keep the recent definition in mind to develop better mixing assessment tools that can more accurately and profoundly describe the performance of mixing in a static mixer.

1.2 Ways to Assess Mixing

The increase in computational power and its ease of accessibility has given rise to computational techniques to analyse mixing between two fluids. The most common techniques used to determine the mixing efficiency of a mixer involve evaluation of intensity of segregation using the Lagrangian particle tracking or injection of contaminant within the flow, which imitates the dispersed flow. The Lagrangian particle tracking involves injection of massless particles within the computational domain from a given point imitating the injection of dispersed phase within the continuous phase. The trajectories of the injected particles are analysed to evaluate mixing efficiency or zones of low and high mixing within the computational domain. Rahmani *et al.* [23] injected around 1225 million particles into a turbulent flow to evaluate not just the mixing efficiency but to also reveal the mixing patterns and their evolution with time. The injection of a large number of particles and their tracking demands high computational overhead and despite the significant computational demand they yet fail to capture the diffusive ability of the fluids. Hobbs and Muzzio [24] also used Lagrangian tracking of particles in a flow passing through a six element Kenics mixer to study mixing. They noticed the presence of small islands for the flows corresponding to the Reynolds of 100. The presence of such islands was identified as barriers to the efficient mixing.

1.2.1 Residence Time Distribution

In the later techniques, i.e. the injection of contaminant in the flow, the concentration of the injected species is measured at the outlet to obtain a distribution curve (also known as the residence time distribution (RTD)). The moments of the distribution are then analysed and compared to evaluate the efficiency of the mixer. The concentration of the contaminant can also be used to deduce the spatial mixing within the mixer by evaluating the coefficient of variance. The quantitative determination of temporal mixing can be performed by numerically evaluating residence time distribution of the system [4].

To estimate the RTD of a closed system (i.e with one inlet and one outlet), a small amount of tracer is injected into the system. Then the exit concentration of the tracer at the outlet, $C(t)$, is measured until the injected tracer is completely washed out from the system. The time during which it happens is denoted as t_∞. The "E-curve", or the distribution, is mathematically represented as follows:

$$E(t) = \frac{C(t)}{\int_0^{t_\infty} C(t)dt} \tag{1.1}$$

The first moment of the distribution determines the average amount of time spent by a fluid molecule within the system, i.e. the mean residence time τ_m:

$$\tau_m = \int_0^\infty tE(t)dt \tag{1.2}$$

The study carried out by Abou Hweij and Azizi [25] points out that RTD analysis could help reveal the existence of dead volumes or occurrence of channeling or bypassing within the device.

The second and the third moments of the curve determine the variance, γ^2, and the skewness, s_k, of the distribution, respectively, and are calculated as follows:

$$\gamma^2 = \int_0^\infty (t - \tau_m)^2 E(t) dt \tag{1.3}$$

$$s_k = \frac{\int_0^\infty (t - \tau_m)^3 E(t) dt}{\tau_m^3} \tag{1.4}$$

Using these quantities, we can assess the mixing performance of the system, for instance, by evaluating the coefficient of variance, $CoV = \gamma/\tau_m$, of the distribution. A CoV of zero indicates complete distributive mixing, whereas CoV of one indicates total segregation.

Stec and Synowiec [16] evaluate and compare the RTD obtained by injecting the contaminant within the Kenics and Koflo mixer over a range of Reynolds number. Sheoran *et al.* [26] provides a detailed review on the experimental determination of RTD using radio-tracers. The deviation of RTD from the desired ideals such as plug flow indicates the presence of stagnation zones, fluid short circuiting and bypassing or the re-circulation zones. These phenomena can adversely affect the quality of mixing, which can result in poor yield in chemical reactors, inadequate mass or heat transfer between the dispersed and continuous phase, fouling or degradation of polymers and bio-materials and creation of unnecessary byproducts [7], [16], [27], [28].

Despite this useful information, RTD posses several shortcomings. First, the RTD provides global information about the flow behaviour with no information about the local flow. If we were to determine the local information of the flow by evaluating RTD at every point in the mixer, it would require a large computational power on top of necessary computationally expensive unsteady flow simulations [27]. The shape of RTD may indicate the presence of back mixing, dead zones or fluid short circuiting, however it fails to provide any information regarding the location of these zones or regions. Second, RTD is not unique to reactor configuration i.e. two reactors/mixers with similar RTD can still yield different products given the reaction follows non linear kinetics [27]. More information on RTD and mixing assessment of Kenics mixer via

RTD is given in Appendix A.

Despite the popularity of both these techniques, i.e. injection of mass less particles or injection of contaminant within the flow, they fail to efficiently and accurately evaluate mixing within the mixer at high Reynolds number. For the case of high Reynolds number turbulent flows the Lagrangian particle tracking fails to capture the effects of turbulent diffusion [27]. The evaluation of concentration of the injected contaminant does seem like a more desirable option compared to the particle tracking however, it posses an added problem of numerical diffusion [29]. Also both these techniques require the use of time dependent solvers [27]. Hence, the size of time step governs the accuracy of the results.

1.2.2 Mean Age

One alternative to both these techniques is the assessment of mixing via mean age. The age of a fluid molecule is equal to time elapsed since the particle has entered the system. The average time required by a group of molecules (control volume, in case of continuum dynamics) to reach a certain location within the mixer is the mean age corresponding to that location. The concept of "age" was initially described by Danckwerts [30]. However, it was first used by Baléo and Le Cloirec [31] to computationally determine the spatial distribution of mean age for a turbulent flow across the channel containing a series of sudden expansions and contractions. Liu and Tilton [27] showed the efficacy of mean age distribution in assessing mixing over Lagrangian tracking and RTD.

Unlike RTD, spatial distribution of mean age can reveal the location of dead zones and short circuiting paths inside the vessel. Obtaining the mean age distribution for a given system is less computationally expensive than obtaining the RTD curve at the outlet. Liu and Tilton [27] shows that it required less than a minute to obtain mean age distribution on a computational domain with 6000 cells, whereas it required 8 hours to obtain RTD curves at a few spatial points in the domain.

Liu [28] used the mean age theory to obtain the spatial distribution of mean age across a six element Kenics mixer for a laminar flow. The study reveals how mean age distribution across the domain of a static mixer can be used to reveal the deviation of flow from the ideal flows, i.e a plug flow or an ideal mixing flow. The spatial distribution of mean age also reveals the transition of lamellar structures into complicated stretching and folding structures as the convection in the flow starts dominating. Hence showing that mean age distribution can reveal both radial and axial mixing. The mean age theory has been applied to continuous stirred tank [28], [32] and micro channel mixers [33] to reveal the efficacy of the mean age theory in evaluating mixing performance of the systems in axial and radial domains.

Since the extension of mean age theory by Liu and Tilton [27] it has been applied to various situations. Immonen [34] used the mean age theory in conjunction with CFD to measure the quality of air in car park, which was then used to optimize the amount of ventilation system for the car park [35]. Tran *et al.* [35] determined spatial homogeneity of materials in transport in a model stir casting system. The mean age theory was recently modified to accommodate the multiphase flows [36]. Russ and Berson [36] used the multiphase mean age theory to predict the just suspended speed of particle in the mixing tanks. Despite the wide application and usage of mean age theory, the studies involving assessment of static mixer via mean age theory in turbulent flows are very limited.

1.3 Objective

The objective of this work is to demonstrate what information about mixing can be obtained from the mean age analysis of turbulent flows. The mean age theory has been used in the past to analyse mixing in laminar flows. However, it has not been rarely used to analyse mixing in turbulent flows. In this thesis we show how mean age theory can be used to assess mixing qualitatively and quantitatively within a static mixer.

The flow is simulated across a Kenics mixer using STAR-CCM+, Siemens PLM [37], a commercial CFD package that is used to simulate physics of the flow. This mixer design is chosen since there are several published numerical and experimental studies of it that will be used for validation purposes [7], [11], [12], [38]. The peripheral objectives of this study are:

1. To numerically evaluate and visualize the flow across static mixer in laminar, transitional and turbulent flow regime.

2. Compare mixing phenomenon by analysing mean age distribution across the mixer for flows in laminar, transitional and turbulent regime.

3. To visually assess if mean age theory can reveal flow features like re-circulation zones, stagnation zones, etc.

4. To predict and locate zones of adverse mixing using mean age theory.

5. To demonstrate how machine learning tools can be used to better understand the results obtained by mean age theory.

1.4 Thesis Organization

Chapter 2 describes the methodology that was used to obtain the simulation results and the distribution of mean age. Chapter 3 provides the validation and verification for the numerical simulation and an in depth analysis into the flow field obtained via these numerical simulations. Once we have analysed the flow field and validated the numerical results we dive into the analysis of mean age distribution, presented in Chapter 4. The final Chapter 5 provides a brief summary of the work that has been described in this thesis.

The thesis also contains two Appendices, Appendix A and B. The first Appendix highlights how Residence time distribution can be used to assess the mixing efficiency of the mixer used in this study. The second Appendix shows how a mean age simulation can be setup using STAR-CCM+ [37].

Chapter 2

Methodology

2.1 Overview

The current chapter provides insight into the computational modelling required to develop a virtual functioning model of a six element Kenics mixer. The first section describes in detail the modelling of the flow across the six element Kenics mixer which is followed by a detailed description of the methodology used to generate the computational grid. The final section provides the mathematics behind the mean age theory and also explains it implementation in STAR-CCM+ [37].

2.2 Problem Statement

In this study, we simulate the flow of liquid through a static mixer containing six Kenics elements placed consecutively in a pipe with an internal diameter $D = 12.7$ mm. The length of the element (L_e) and thickness (w) of each element are 22.5 mm and 2 mm, respectively. The inlet and outlet are extruded in the normal direction by $12D$ and $16D$, respectively, to allow the flow to develop and avoid back-flow (Figure 2.1). The density and dynamic viscosity of the working liquid, which is water, are 998.2 kg/m^3 and 10^{-3} Pa $\cdot$ s, respectively.

2.2.1 Governing Equations

The mass conservation equation for the steady, incompressible flow can be written as

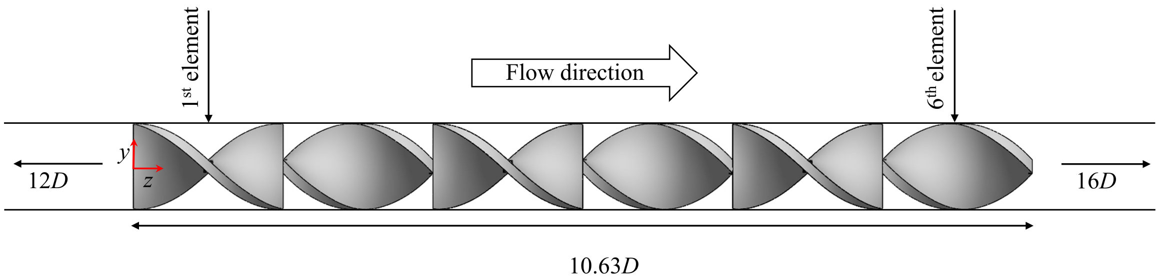

Figure 2.1: The computational domain on which laminar and turbulent flows were simulated.

$$\nabla \cdot \vec{u} = 0 \tag{2.1}$$

The momentum conservation equation for an incompressible steady laminar flow in absence of body force is given as follows

$$\rho \vec{u} \cdot \nabla \vec{u} = -\nabla P + \mu \nabla^2 \vec{u} \tag{2.2}$$

The turbulent flow regime is numerically evaluated by solving the Reynolds averaged Navier Stokes (RANS) equations. The RANS approach involves dissociation of instantaneous velocity, $\vec{u}$, into average and fluctuating components, thereby eliminating the need to fully resolve the flow [39]. The equations 2.3 and 2.4 represent averaged mass and momentum equations for incompressible flow in vector notation. The mean and fluctuating component of velocity is denoted by $\vec{U}$ and $\vec{u'}$, respectively.

$$\nabla \cdot (\vec{U}) = 0 \tag{2.3}$$

$$\rho \nabla \cdot (\vec{U}\vec{U}) = -\nabla p + \mu \nabla^2 \vec{U} - \rho \nabla \cdot (\overline{\vec{u'}\vec{u'}}) \tag{2.4}$$

2.2.2 Turbulence Modeling

To compute turbulent flows with the RANS equations it is necessary to employ turbulence models to address the closure problem: additional equations are necessary to estimate the components of the Reynolds stress tensor [40]. Various turbulence modelling techniques can be found in the literature [39]. In this study, three different turbulent models have been used to evaluate the flow across the static mixer: Realizable $k-\varepsilon$ [41], Elliptic-Blending (EB) $k-\varepsilon$ [42] and Reynolds stress model [43]. The results obtained by different turbulence models on different grids are contrasted with each other in Chapter 3.

The Realizable $k-\varepsilon$ model and the EB $k-\varepsilon$ model both resort to Boussinesq's hypothesis [44] to resolve the turbulence closure problem, i.e. approximation of Reynolds's stresses ($\overline{\vec{u}'\vec{u}'}$). Like the Realizable $k-\varepsilon$ model the EB $k-\varepsilon$ model also solves two additional transport equations of turbulent kinetic energy and turbulent dissipation rate for estimating turbulence parameters. However unlike the Realizable $k-\varepsilon$ model it solves two additional equation for estimating two non dimensional variables, ϕ and α. The variable ϕ represents the ratio of wall normal Reynolds stress to turbulent kinetic energy (thus being a measure of the near-wall turbulence anisotropy) and the, α, is a wall proximity sensitive quantity (i.e. it takes the value 0 at a wall and 1 in the far field) [45].

The Reynolds stress model (RSM) follows an alternative approach. It solves six additional transport equations, one for each term in the Reynolds stress tensor [41], [46], [47] along with transport equation for another quantity that would provide approximation for the length-scale or time-scale of the turbulence. The RSM model should be preferred when non isotropic effects are important. The turbulence encountered within the turbulent boundary layer is always non isotropic, the isotropic eddy viscosity models such as $k-\varepsilon$ and EB $k-\varepsilon$ models handle such non isotropic flow well in the near wall regions [23]. However $k-\varepsilon$ models give a poor representation when strong curvature and swirling flows induce non isotropic effects within the flow. Henceforth RSM has also been used to simulate turbulent flow across the Kenics mixer.

2.2.3 Solvers

A finite volume segregated flow solver was used. The pressure velocity coupling was achieved by using the SIMPLE algorithm [48]. To achieve higher accuracy, third order schemes were used for spatial discretisation of the convective term. The evaluation and reconstruction of gradients at the faces and center of volume elements were obtained using hybrid Gauss least squares method [49]. A gradient limiter Venkatkrishnan [50] was used to assert confidence on the values of reconstructed gradients by keeping a check on unrealistic gradient values. The turbulent parameters are evaluated by solving the necessary transport equations depending on the choice of turbulent models. The algebraic forms of discretised equations are evaluated by Algebraic Multi Grid linear solver with a Gauss-Siedel relaxation scheme and a strict convergence tolerance of 10^{-5} or lower.

2.2.4 Boundary Conditions

No-slip boundary condition is implemented at the walls and the solid surface of the static mixer. A constant flow rate is specified at the inlet boundary with a fully developed velocity profile. The fully developed profile of velocity, turbulent kinetic energy and dissipation rate are evaluated by simulating a pipe flow with initial conditions evaluated based on the Reynolds number of the flow. The turbulent boundary conditions at the inlet are defined by specifying a profile of turbulent kinetic energy, k, and turbulent dissipation rate, ε, corresponding to a the respective velocity profile. The constant mass flow rate, $\dot{m}$ for each simulated case alongside Reynolds number, $Re = \frac{\rho U_{in} D_0}{\mu}$ is given in the Table 2.1.

2.2.5 Convergence Criteria

For all simulated cases, it was made sure that the absolute residuals of the continuity and momentum equation dropped below 10^{-5}. For the case of turbulent flows the asymptotic values of averaged turbulent kinetic energy and dissipation rate were

Table 2.1: Mass flow rates for simulated cases

Re	$\dot{m}$ [kg s]	U_{in} [m s^{-1}]
1	9.98×10^{-6}	7.89×10^{-5}
10	9.98×10^{-5}	7.89×10^{-4}
100	9.98×10^{-4}	7.89×10^{-3}
1000	9.98×10^{-3}	7.89×10^{-2}
5069	5.06×10^{-2}	4.00×10^{-1}
6843	6.83×10^{-2}	5.40×10^{-1}
9504	9.48×10^{-2}	7.45×10^{-1}
10391	1.04×10^{-1}	8.20×10^{-1}
12000	1.20×10^{-1}	9.47×10^{-1}

tracked along with the residuals of momentum and continuity equations. A strict asymptotic criteria was followed to make sure that the values of turbulent kinetic energy and turbulent dissipation energy have converged across the entire domain. The asymptotic criteria was employed such that the difference between the maximum and minimum value within the 10 consecutive iterations is less than 10^{-5}.

2.3 Mesh

Mesh generation is the crucial step of any computational simulation as effective numerical processes for CFD problems depend upon the grid quality [11]. To systematically assess the effect of mesh refinement in the core and near wall region four different orthogonally structured grids are developed using mesh generation software, ICEM Ansys Inc. [51]. The coarsest grid A contains 73 152 elements followed by grids B, C and D containing 922 632, 8 969 904 and 16 013 004 elements respectively. Figure 2.2 shows a cross section of each grid perpendicular to axial flow. Though the four grids are systematically refined by reducing the size of volume element, the topology of the mesh is different in the wall region. A standard approach to measure the fineness of the mesh in near wall region is to monitor the normal distance between the solid wall and the center of computational cell adjacent to the solid wall, y, in terms of dimensionless distance, $y^+ = y\sqrt{\rho\tau_w}/\mu$. τ_w is the wall shear stress magnitude, ρ and μ represent density and viscosity of the single phase flow.

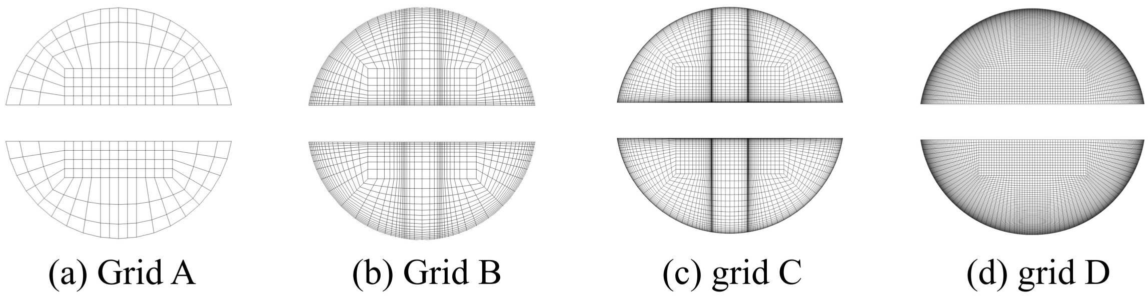

Figure 2.2: Cross-sectional view of structured Grids.

The approximate initial values of y^+ calculated using the inlet velocity, U_{in} Equation 2.5 for the above mentioned grids are shown in Table 2.2. The discrepancy in wall refinement is maintained to assess the effect of wall treatment on mixing analysis. Wall function are semi-empirical formulas used to bridge gap between the viscosity affected region and the fully turbulent flow, obviating the need to resolve the viscosity affected near wall region and to modify turbulence models to account for the presence of wall [14].

$$y^+ = \frac{y\sqrt{0.0296Re^{-1/5}U_{in}^2}}{\nu} \tag{2.5}$$

For the grids with $y^+ < 1$ no wall function is used and the flow is resolved in the boundary layer region as well as in the core region of the static mixer. For the rest of the grids a two layer all y^+ wall treatment is used, which is a combination of blended wall function along with the two layer formulation of the underlying turbulence model. The blended wall function or all y^+ wall treatment uses a standard wall functions proposed by Launder and Spalding [52] to impose algebraic values of turbulent kinetic energy and dissipation rate in the cell centroids closest to the wall. The imposed vales are a function of y^+ and vary depending on the wall refinement. A two layer

Table 2.2: Mesh refinement parameters

grid	Approximated y^+	Elements
A	≈ 63.54	73 152
B	≈ 3.81	922 632
C	≈ 0.67	8 969 904
D	≥ 10	16 013 004

approach imposed on top of all y^+ wall treatment however solves for the budget of turbulent kinetic energy in the near wall region and imposes specific values of turbulence dissipation rate at the centroids of the near-wall cells.

2.3.1 Mesh Generation

The mesh generation procedure for an orthogonal structured mesh involved the use of out of the box technique. Each grid i.e A, B, C, D was generated in 8 different parts, one each for six Kenics elements and 2 for the inlet and outlet extrusions. These separate grids were then combined using interfaces to create a computational domain for six element Kenics mixer. The tedious way of mesh generation provided more control over refinement of grid and prevented occurrence of skewed elements within the grid. It also allowed for refinement in specific regions to capture the necessary flow phenomenon and mixing. However to make sure that the combination of grids via interfaces is efficient, the grids had to be symmetric in x and y axis. To do so a surface mesh with an O-grid shown in Figure 2.3 was first developed. The coloured bold lines overlaying the mesh were segmented into the nodes. The length k_n is equal to the thickness of the Kenics element. The vertical and horizontal length of the nodes in proximity to Kenics elements are controlled by segmentation of V_n and H_n. The line, l_n, is segmented accordingly to control the wall refinement in proximity to pipe walls. The subscript n represents the number of segments for the respective line. The inlet surface mesh can then be extruded to length L_{ie} to form an inlet extrusion creating the first grid part shown in Figure 2.4. The end of the extrusion is then carefully divided into three surface grids shown in Figure 2.5. The bottom and the above surface grid marked in yellow colour was then twisted around a straight line starting at the center of the ending surface of the inlet extrusion and extending a normal distance L away from the ending surface grid. A standard Kenics element is twisted by 180° around the axial axis. A twist per each extruded layer of mesh was specified. For a layer with constant spacing twist angle per spacing required to achieve a cumulative of 180° is equivalent to 180° divided by the number of mesh extrusion layers, N_{KM}. The thickness of each extrusion layer is estimated based on the element size of the inlet surface. The central strip marked in green colour marks the surface of leading edge of a Kenics element. A similar twisted extrusion is performed on the strip to obtain a solid Kenics element which will act as a solid obstacle to the fluid flow passing around it.

The mesh for the other five Kenics element is then created by translation and rotation of part 2. The final grid part i.e outlet extrusion was also created by mirroring the inlet extrusion about the center of the Kenics mixer. All the grids are then connected via internal interfaces. A complete assembled grid with all the interfaces is shown in Figure 2.6.

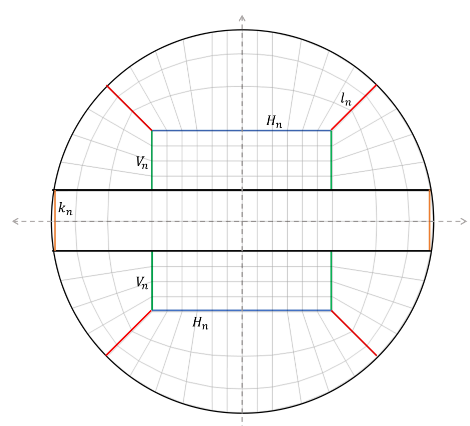

Figure 2.3: Butterfly mesh on inlet surface

Using the above mentioned grid generation procedure a total of four different grids

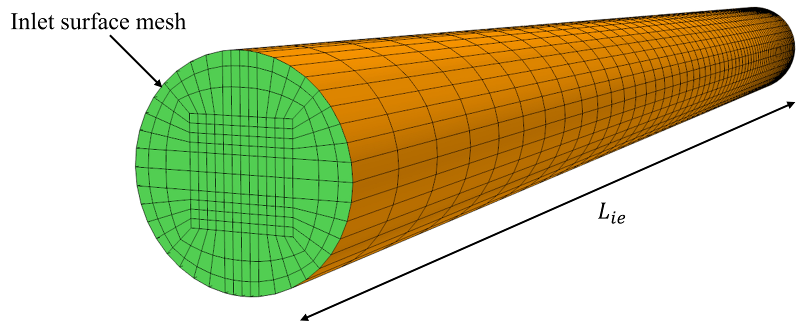

Figure 2.4: Extruding surface mesh

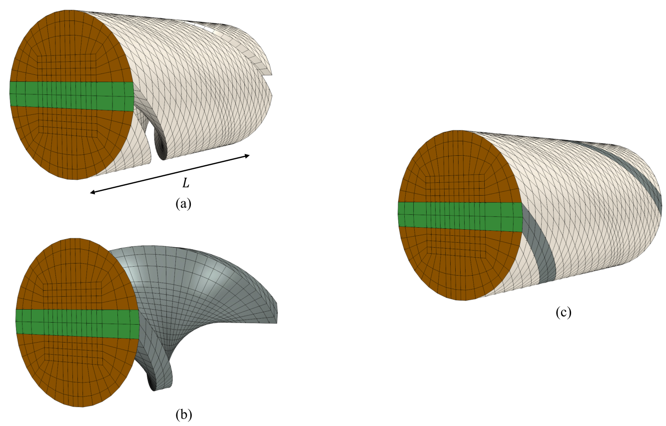

Figure 2.5: extrusion of surface mesh to Kenics element

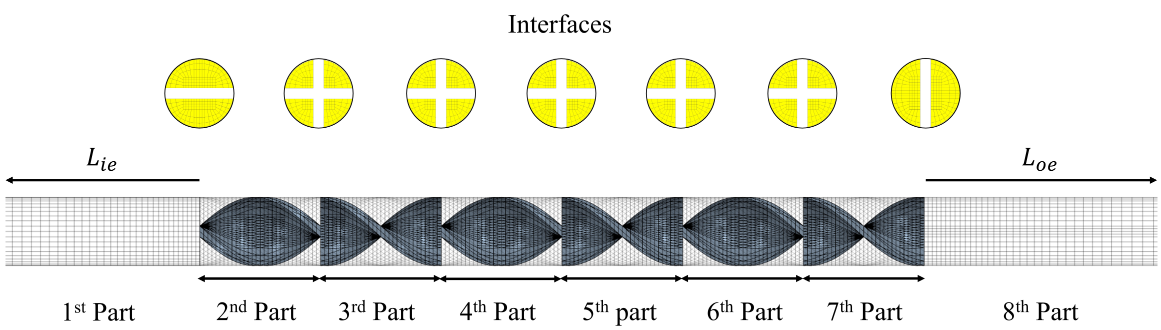

Figure 2.6: Assembled structured mesh

have been generated. The inlet surface mesh for each grid besides an $x-$ normal grid view is shown in Figure 2.7.

2.3.2 Grid Generation Challenges

The major hurdle in generating a mesh for Kenics element was its geometry. The wall refinement along the helical wall of Kenics element and the trailing and leading edges

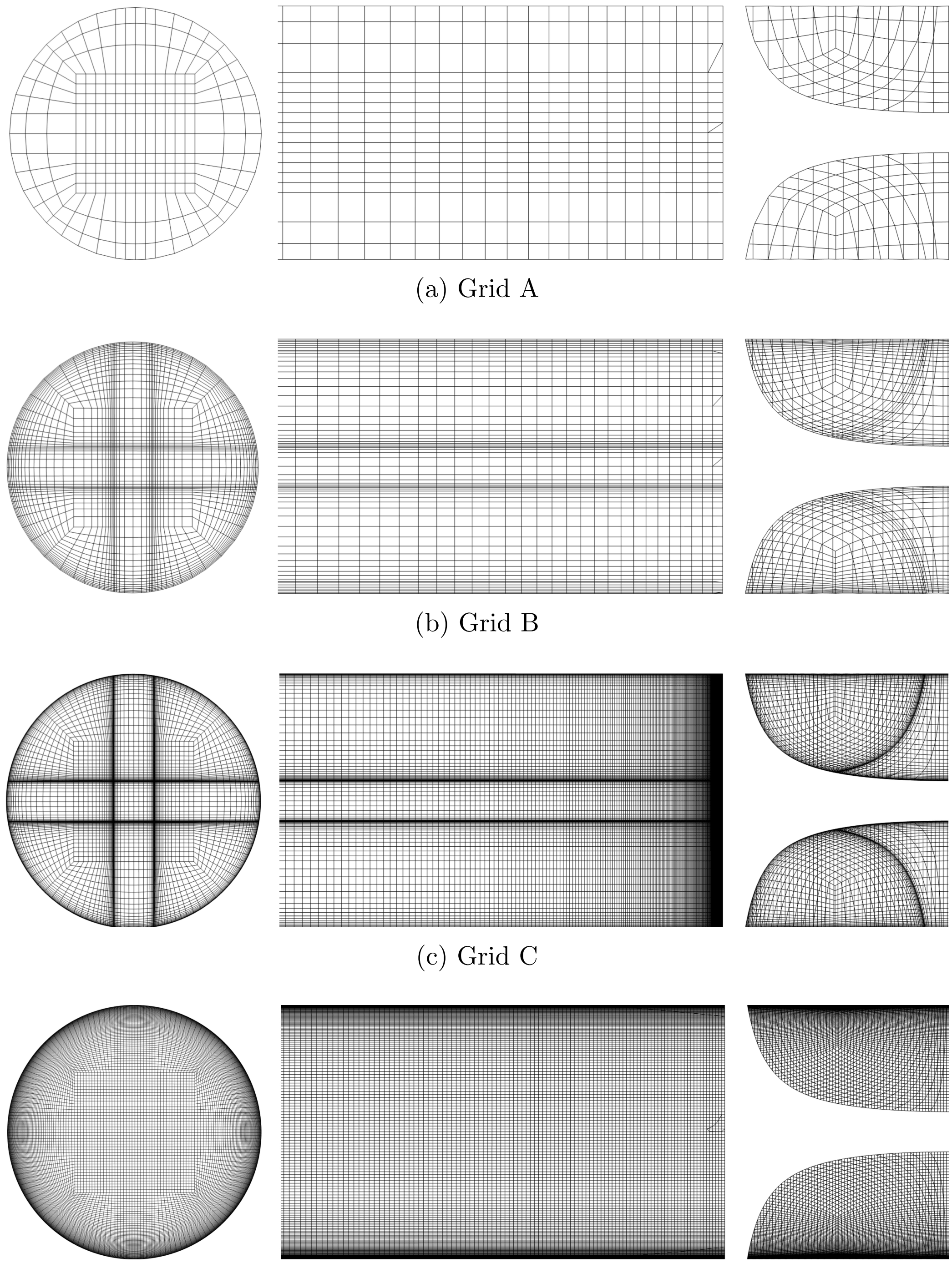

(a) Grid A

(b) Grid B

(c) Grid C

(d) Grid D

Figure 2.7: Structured grids

of these elements was particularly challenging to achieve. In the above section we mentioned that we used an O-grid to allow for a symmetric mesh that can be twisted along the wall of the Kenics element. In Figure 2.3 it can be seen that the grid has two regions. The square region at the center which contains hexahedral elements. The region two contains elements with curved surfaces to emulate the surface of a circular cylinder. The transition of elements from region one to region two results in skewed elements. It is safe to assume that it will not cause a significant numerical error as the dominant direction of the flow is perpendicular to these skewed transition. The efforts were also made to mitigate skewness, i.e. maintaining growth rate and aspect ratio of elements within the acceptable limits and size reduction of volume elements to avoid skewed elements in general.

Another challenge was to achieve wall refinement along the leading and trailing edge of the Kenics elements. To do so extrusion of surface mesh in the axial direction must be non uniform. The thickness of elements in axial direction should gradually increase, with layer close to the leading and trailing edges of Kenics elements having thickness equal to 10^{-5} ($y+ \approx 1$). A gradual increase is necessary to prevent a large number of elements which would then make the simulations computationally intensive. A closer look at Figure 2.2 reveals that out of the four grids only Grid C was equipped with a wall refinement at the edges. A thick dense region before the start of Kenics element in Figure 2.2c can be observed.

Grid C is equipped with wall refinement along all the solid surfaces. It was used to simulate flow for all Reynolds number cases except for cases that involved laminar flow.

2.4 Mathematical Representation of Mean Age

As Danckwerts [53] states that the Equation A.1, generally used for determining residence time distribution at the outlet can also be applied to any spatial location within the system to evaluate age of the particle. The Equation 2.6 mathematically represents the evaluation of age at any given location within the system. $\tilde{E}$ represents the frequency distribution of the age of molecules at the local point of interest $\tilde{\mathbf{x}}$. The fraction of molecules having age between $\tilde{a}$ and $\tilde{a} + d\tilde{a}$ is $\tilde{E}da$.

$$\tilde{E} = \frac{\int_0^\infty C(\tilde{\mathbf{x}}, \tilde{a})dt}{\int_0^\infty C(\tilde{\mathbf{x}}, t)dt} \tag{2.6}$$

The average of the frequency distribution given by, $\tilde{E}$, can be represented as the mean age, $a(\tilde{\mathbf{x}})$, at any local point $\tilde{\mathbf{x}}$. The Equation 2.7 represents spatial mean age distribution.

$$a(\tilde{\mathbf{x}}) = \frac{\int_0^\infty tC(\tilde{\mathbf{x}}, t)dt}{\int_0^\infty C(\tilde{\mathbf{x}}, t)dt} \tag{2.7}$$

Determining frequency distribution of ages of particles at each specific location either experimentally or numerically is resource intensive. The early literature by Spalding [54] and Sandberg [55] provide a much easier way to compute spatial distribution of mean age by employing a steady state transport equation. The computation of $a(\tilde{\mathbf{x}})$ using CFD in a turbulent channel was shown as an example by Baléo and Le Cloirec [31]. However more recently, the expansion of the mean age theory and its feasible application to complex incompressible flows across mixers has been shown by Liu and Tilton [27].

Following the work of Liu and Tilton [27] a scalar transport equation for the concentration of dispersed phase, C, (given by Equation 2.8) can be manipulated to obtain a differential equation for determining the spatial distribution of mean age.

$$\frac{\partial C}{\partial t} + \nabla \cdot (\vec{U}C) = \nabla \cdot (\mathcal{D}\nabla C) \tag{2.8}$$

Where diffusivity coefficient, $\mathcal{D}$, is defined by the linear diffusivity model as given by Equation 2.9.

$$\mathcal{D} = \frac{\mu}{\sigma_m} + \frac{\mu_t}{\sigma_t} \tag{2.9}$$

where σ_m is the molecular Schmidt number and σ_t is turbulent Schmidt number. The molecular Schmidt number, σ_m, was fixed to a value of 10^{10} m^2/s. It is not a critical value, since the contribution of molecular diffusion i.e μ/σ_m, to the overall tracer dispersion process is expected to be small for turbulent flows [14]. Moreover the purpose of the paper is to assess the effect of convection and turbulence rather than mixing due to molecular diffusion. The commonly suggested value of 0.7 for the turbulent Schmidt number is adopted in the present study [14], [56].

Multiplying Equation 2.8 by t and integrating over time yields Equation 2.10. As time is independent of the spatial coordinate it's derivative with respect to spatial coordinate will be zero. Hence Equation 2.8 can be manipulated to obtain Equation 2.10.

$$\int_0^\infty t\frac{\partial C}{\partial t}dt + \int_0^\infty \nabla \cdot (t\vec{U}C)dt = \int_0^\infty \nabla \cdot \mathcal{D}\nabla(tC)dt \tag{2.10}$$

The first term on the left hand side can be integrated by parts as given in Equation 2.11.

$$\int_0^\infty t\frac{\partial C}{\partial t}dt = tC|_0^\infty - \int_0^\infty Cdt \tag{2.11}$$

Spalding [54] mentions that for an incompressible flow across a closed system, the amount of concentration added over any amount of time must be constant i.e spatially invariant.

$$I = \int_0^\infty Cdt \tag{2.12}$$

The first term on the right hand side of Equation 2.11 will be zero as t tends to infinity [27]. With $tC|_0^\infty = 0$, substituting Equation 2.11 in Equation 2.10 and dividing by I yields Equation 2.13.

$$-1 + \nabla \cdot \vec{U}\left[\frac{\int_0^\infty tCdt}{\int_0^\infty Cdt}\right] = \nabla \cdot \mathcal{D}\nabla\left[\frac{\int_0^\infty tCdt}{\int_0^\infty Cdt}\right] \tag{2.13}$$

To obtain the above equation, we have exploited the fact that $\vec{U}$ and $\mathcal{D}$ are invariant with time along with the fact that I is spatially invariant. The quantity in square brackets can now be expressed as the mean age, a, giving the conservation equation for mean age as Equation 2.14.

$$\nabla \cdot (\tilde{\mathbf{U}} a) = \nabla \cdot \mathcal{D} \nabla a + 1 \tag{2.14}$$

The mean age, $a(x)$ is the first moment of the distribution of the amount of time taken by the particle to reach a local point. The higher moments of the distribution can also be evaluated by deriving the steady state transport equations for the same in a similar manner described above.

For the n^{th} moment of the distribution t in Equation 2.10 can be replaced by t^n giving out Equation 2.15.

$$\int_0^\infty t^n \frac{\partial C}{\partial t} dt + \int_0^\infty \nabla \cdot (t^n C \vec{U}) dt = \int_0^\infty \nabla \cdot \mathcal{D} \nabla (t^n C) dt \tag{2.15}$$

Applying integration by parts on the first term yields

$$\int_0^\infty t^n \frac{\partial C}{\partial t} dt = t^n C|_0^\infty - \int_0^\infty n t^{n-1} C dt \tag{2.16}$$

The first term on the right hand side of Equation 2.16 has to be zero for the mean age to exit locally [27]. Then substituting the first term in Equation 2.15 using Equation 2.16 and dividing the equation by I we get Equation

$$- \left[\frac{\int_0^\infty n t^{n-1} C dt}{\int_0^\infty C dt} \right] + \nabla \cdot \vec{U} \left[\frac{\int_0^\infty t^n C dt}{\int_0^\infty C dt} \right] = \nabla \cdot \mathcal{D} \nabla \left[\frac{\int_0^\infty t^n C dt}{\int_0^\infty C dt} \right] \tag{2.17}$$

The n^{th} moment of the mean age is equivalent to $M_n = \frac{\int_0^\infty t^n C dt}{\int_0^\infty C dt}$. Therefore Equation 2.17 can be written as

$$\nabla \cdot (\vec{U} M_n) = \nabla \cdot \mathcal{D} \nabla M_n + n M_{n-1} \tag{2.18}$$

By determining the second moment of the mean age distribution, i.e M_2, the variance σ^2 can be determined using Equation 2.19.

$$\sigma^2 = \frac{\int_0^\infty (t^2 - a^2)Cdt}{\int_0^\infty Cdt} = M_2 - a^2 \tag{2.19}$$

The coefficient of variance, which estimates the mixing at any local point can be determined by the ratio of square of variance to the mean age, i.e, $CoV = \sigma/a$.

Mean Age Frequency Distribution

Consider a differential volume $dv(a)$ in the flow domain with mean age in the range of a and $a + da$. The fraction of the volume with mean age in the range out of the total volume of the flow domain is a function of a [32]. This function, $g(a)$, can be represented in Equation 2.20.

$$g(a)da = \frac{dv(a)}{V} \tag{2.20}$$

In order to comprehend the mean age frequency distributions ability to characterize mixing of the flow, we must look at the two ideal flows: the plug flow and the ideal mixer flow. For a plug flow within a pipe of length L in absence of molecular diffusion and complete segregation with a constant velocity U, the mean age at a distance z from the inlet can be defined as $a = z/U$ and similarly $da = dz/U$. The differential volume with mean age between a and $a + da$ can also be written as $dv = Adz$ where A is the cross sectional area. We then obtain a frequency distribution function for plug flow (Equation 2.21).

$$g(a) = \frac{1}{V}\frac{dv}{da} = \frac{U}{L} = \frac{1}{\tau}, a \in [0, \tau] \tag{2.21}$$

$$g(a) = 0, a > \tau \tag{2.22}$$

For an ideal mixer, the molecular age t everywhere inside the reactor is the same as that at the exit and has an exponential distribution as given in Equation 2.23.

$$\psi = \frac{1}{\tau}\exp(-t/\tau) \tag{2.23}$$

The frequency distribution of mean age at any given cross section can be derived by assuming that the axial length of the volume element, i.e dz is the same irrespective of the x and y position of the volume elements. Therefore the differential volume $dv(a)$ can be written as $dzds(a)$. Where $ds(a)$ refers to the differential cross sectional surface area of the elements with mean age between a and $a+da$. The total volume V can also be written as Sdz, given all the volume elements have similar normal length dz and S is the total surface area of the elements having mean age between a and $a+da$. Hence a frequency distribution of mean age at any given surface as a function of a, $g_s(a)$ is given by Equation 2.24.

$$g_s(a)da = \frac{ds(a)}{S} \tag{2.24}$$

The distribution of mean age at any given cross section or surface S at any axial coordinate z, can be used to define the areas with younger and older age.

2.4.1 Relating Moments of Residence Time Distribution and Age

Liu and Tilton [27] points out that the theoretical mean residence time ($\tau = V/Q$) for a closed system is equivalent to the flow averaged mean age on the exit surface (S_e) of the system, i.e $\overline{a_e}$. Infact the moments residence time are equivalent to moments of age at the exit surface, i.e $\overline{t^n} = \overline{M_{n,e}}$. Where n refers to the n^{th} moment. Following the work of Liu and Tilton [27], the amount of concentration leaving the outlet can be given as

$$C_{out}(t) = \frac{\int_{S_e} uC(\vec{x},t)dA}{\int_{S_e} C(\vec{x},t)dA} \tag{2.25}$$

$$\overline{t^n} = \int_0^\infty t^n E(t)dt = \frac{\int_0^\infty t^n C_{out}(t)}{\int_0^{t_\infty} C_{out}(t)dt} \tag{2.26}$$

Substituting the value of C_{out} from Equation 2.25 into Equation 2.26 yields,

$$\overline{t^n} = \frac{\int_0^\infty t^n \int_{S_e} uC(\vec{x},t)dA}{\int_0^{t_\infty} \int_{S_e} uC(\vec{x},t)dAdt} \tag{2.27}$$

Using the property of spatial invariance Equation 2.27 can be written as

$$\overline{t^n} = \frac{\int_{S_e} u[\int_0^\infty t^n C(\vec{x},t)dt / \int_0^\infty C(\vec{x},t)dt]dA}{\int_{Se} udA} \tag{2.28}$$

Henceforth the above equation can be written as below to prove that the mixing cup mean exit age is equivalent to τ.

$$\overline{t^n} = \frac{\int_{S_e} uM_n dA}{\int_{Se} udA} = \overline{M_{n,e}} \tag{2.29}$$

It must be noted that in the present study, injection of the scalar for obtaining the residence time distribution was performed at a location closer to the leading edge of the first element. A theoretical mean age for this scenario, τ_I can be defined as ratio of fluid occupied between the point of injection till the outlet (V_I) to the volume flow rate of the fluid within the system (Q). It should also be kept in mind that the τ_m is not equivalent to the mixing cup average of mean age nor is it equivalent to τ and τ_I. The reason for τ_m in-equivalence to τ is due to the injection location of the scalar being other than the inlet of the system. The reasons for τ_m in-equivalence to τ_I have been interpreted by Abou Hweij and Azizi [25]. The results will further describe this discrepancy in detail.

2.4.2 Variance of Age

The main purpose of the variance of age is to provide a measure that allows for quantification of mixing. The mean age theory provides ways to evaluate variance of residence time distribution and the variance of age.

Variance of Residence Time Distribution

One measure of mixing in the mixer is the measure of variance around the residence time of the system at the exit. It can be mathematically quantified as given by Equation 2.30 given below [57].

$$\overline{\sigma_e^2} = \frac{1}{\tau^2}\int_0^\infty (1-\tau^2)^2 E(t)dt = \frac{\overline{M_{2,e}} - \tau^2}{\tau^2} = \frac{2}{} \tag{2.30}$$

It must be noted that the variance of RTD curve obtained from a point source represented by γ_2 is different from $\overline{\sigma_e^2}$. As $\overline{\sigma_e^2}$ represent the variance of distribution across the theoretical mean time. $\overline{\sigma_e^2}$ represents variance of distribution for an instance when the tracer is injected at the inlet along with flow. $E(t)$ in Equation 2.30 represents the RTD curve obtained for the case when the tracer is injected along with the flow at inlet.

Evaluating Variance of Age

The distribution of age at any given cross section can be assessed by evaluating the variance of age. The variance of mean age can be defined as below.

$$\sigma_a^2 = \frac{\overline{a^2} - \overline{a}^2}{\overline{a}} \tag{2.31}$$

The overline on a indicates mass flow averaging over surface. The definition is similar to statistical variance of any scalar quantity.

2.4.3 Evaluating Mean Age Distribution

The mean age distribution in the domain was determined by the solving scalar transport equation for a steady state with the source term equal to unity (see Equation 2.14). The following boundary conditions were used: $a = 0$ was set at the inlet since it is assumed that the point of injection coincides with the inlet; no penetration and zero gradient boundary conditions were set at the solid walls and the outlet, respectively. The finest grids C and D were used to perform simulations for a range of Reynolds number defined in Table 2.1. The steps for setting up the simulation to evaluate the mean age are shown in Appendix B.

2.5 Summary

In this section we described in detail the methodology that was used to perform numerical simulations along with the mathematical expressions and derivations for mean age. The incompressible steady flow field for laminar and turbulent flow was evaluated using STAR-CCM+ [37] on a computational grid generated using ICEM Ansys Pvt. Ltd. [51]. Four different type of grids were created with each grid being more refined than the previous one. The topology of the grid in the near wall region is different in all four grids to allow for analysis into the effect of wall refinement on the evaluation of flow field using STAR-CCM+ [37]. A new way of analysing mean age distribution via surface averaged distribution of mean age is mathematically represented. A derivation for relating residence time distribution and mean age is also presented to justify the capability of mean age for analysing mixing within the mixer. Further we present derivation for evaluation of variance of age and explain how it can help assess mixing within the mixer. We present the methodology that was used to simulate the mean age distribution in STAR-CCM+ [37] in Appendix B.

Chapter 3

Flow Analysis

3.1 Overview

The incompressible flow was simulated across a six element Kenics mixer. The simulated flow cases corresponded to the Reynolds of 1, 10, 100, 1000, 5069, 6843, 9504, 10391 and 12000. In the current chapter we start by validating the numerical results and then qualitatively and quantitatively compare the velocity field obtained for the various simulated cases.

3.2 Model Verification and Validation

To ensure that numerical simulations can produce accurate results to assess mixing performance, it is necessary to verify and validate the numerical model with respect to modelling and numerical settings. To assert confidence in to our results we start by presenting the convergence of flow field parameters (i.e. velocity and turbulence parameters). More confidence in the numerical results was obtained by simulating several cases 1) to study the effect of mesh (mesh independence study) on prediction of the pressure drop, flow resolution, and major quantities related to turbulence; 2) to investigate the effect of the turbulence model choice on estimation of turbulence quantities; 3) to validate pressure drop estimation by comparison to available reference data.

3.2.1 Convergence

The convergence of numerical simulations was guaranteed by tracking the residuals of momentum and continuity equations. For the cases pertaining to the turbulent flow the convergence was asserted also by tracking the volume averaged quantities (i.e. parameters averaged over the volume of the computational grid).

Residuals

The residual history for the numerical simulation performed using Reynolds Stress Model for the flow corresponding to Reynolds of 12000 on four different grids discussed in Chapter 2 are shown in Figure 3.1. The residuals are normalised with respect to the maximum residual value over the respective iteration. The number of iteration required to achieve convergence is the lowest for Grid A, approximately 500. The Grid C requires a maximum number of iterations for the continuity and the momentum equation to converge, approximately 5500 iterations. A more smoother convergence was obtained on Grid C compared to other grids. This is due to the fact that the Grid C is refined in the near wall region such that the value of y^+ is below unity (Refer to Section 2.3). Grid D with approximately twice the number of volume elements than Grid C provides a quicker convergence at the expense of higher residual values.

The residual history for the numerical simulations performed using Realizable $k-\varepsilon$ and EB $k-\varepsilon$ model on Grid C to evaluate the turbulent flow corresponding to the Reynolds of 12000 are shown in Figure 3.2. It can be observed that Realizable $k-\varepsilon$ model tends to converge faster than the EB $k-\varepsilon$ model which evaluates erratic residuals even after a staggering 6000 iterations. However, the residual values are higher for the flow simulated via Realizable $k-\varepsilon$ model. In general both the turbulence

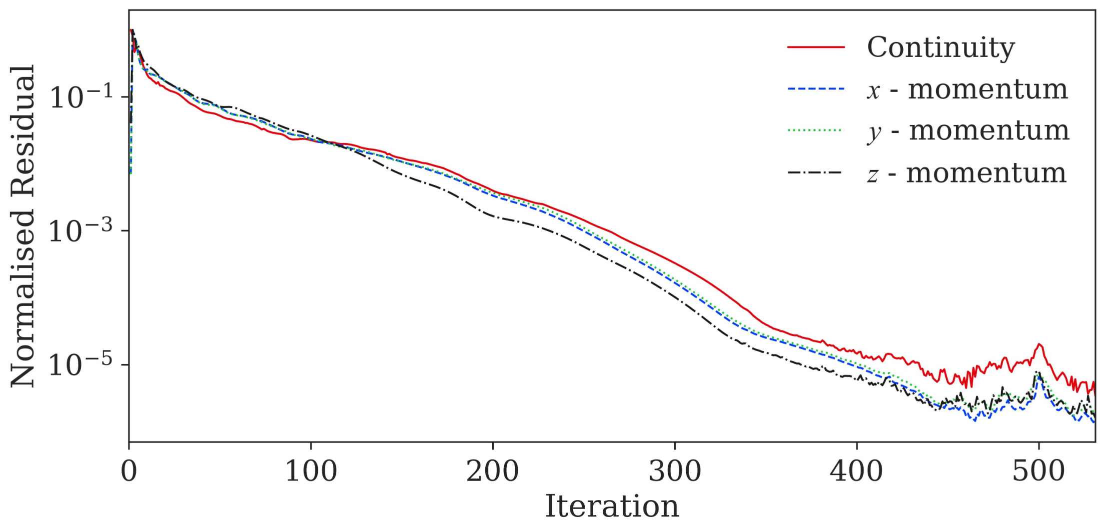

(a) Grid A

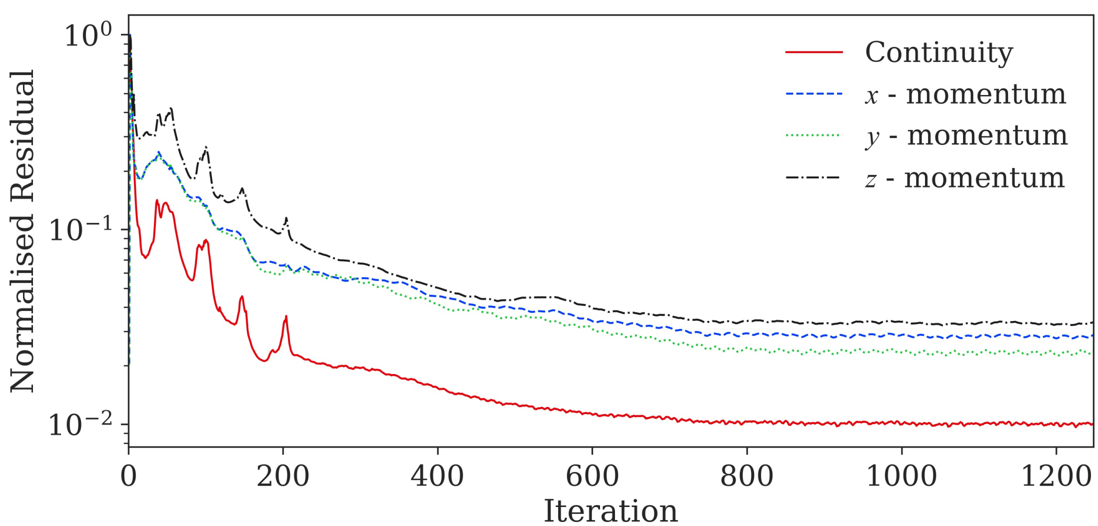

(b) Grid B

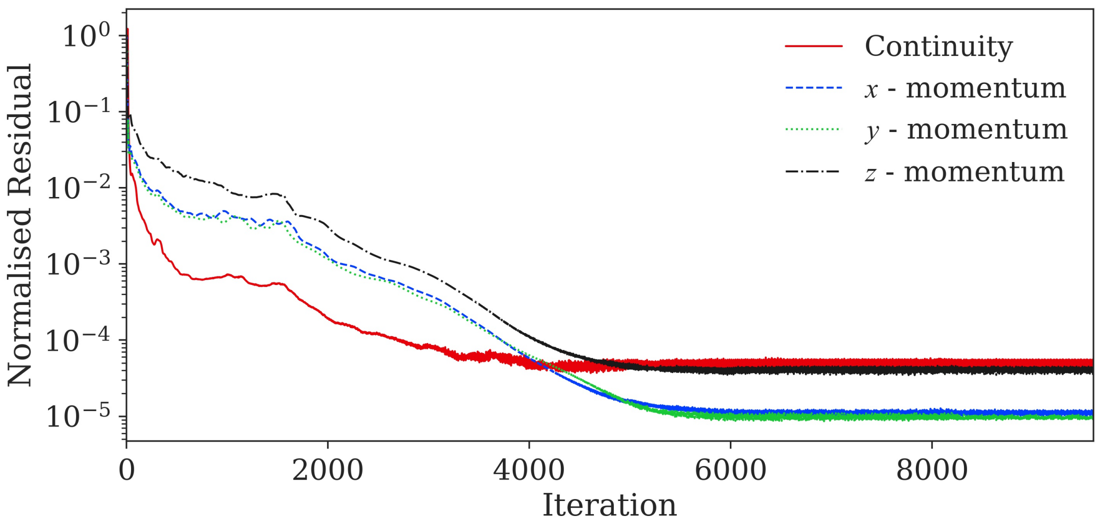

(c) Grid C

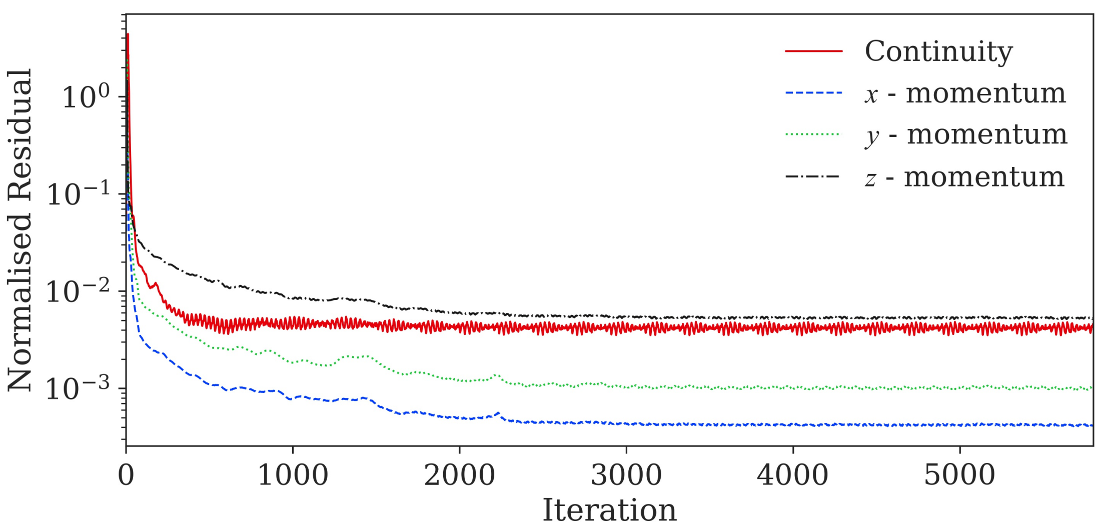

(d) Grid D

Figure 3.1: The residual history for the numerical evaluation of flow via Reynolds Stress model on Grids A, B, C and D are shown.

models fail to provide a smoother convergence when compared to the flow simulated using Reynolds Stress Model on Grid C (Figure 3.1c).

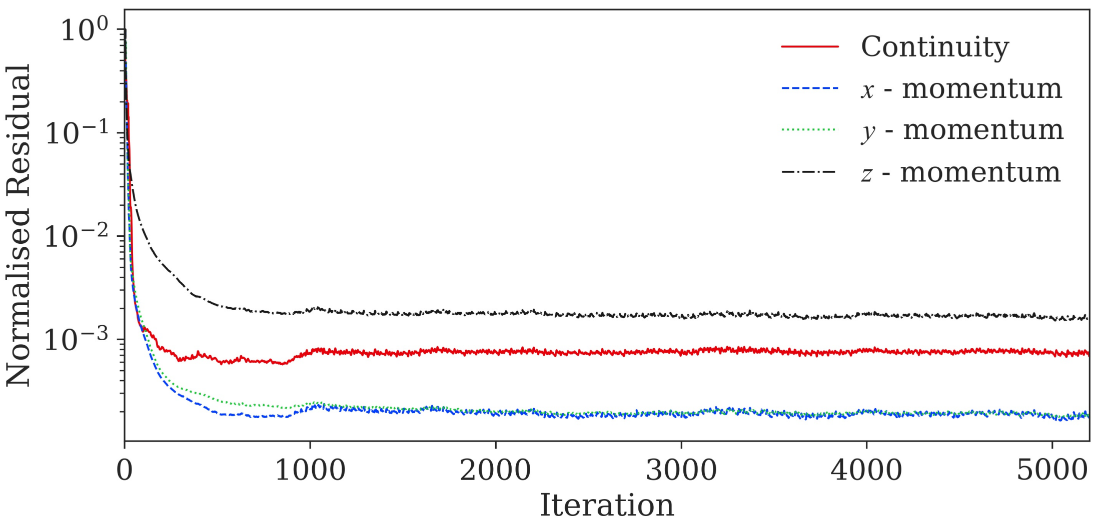

(a) Realizable $k - \varepsilon$

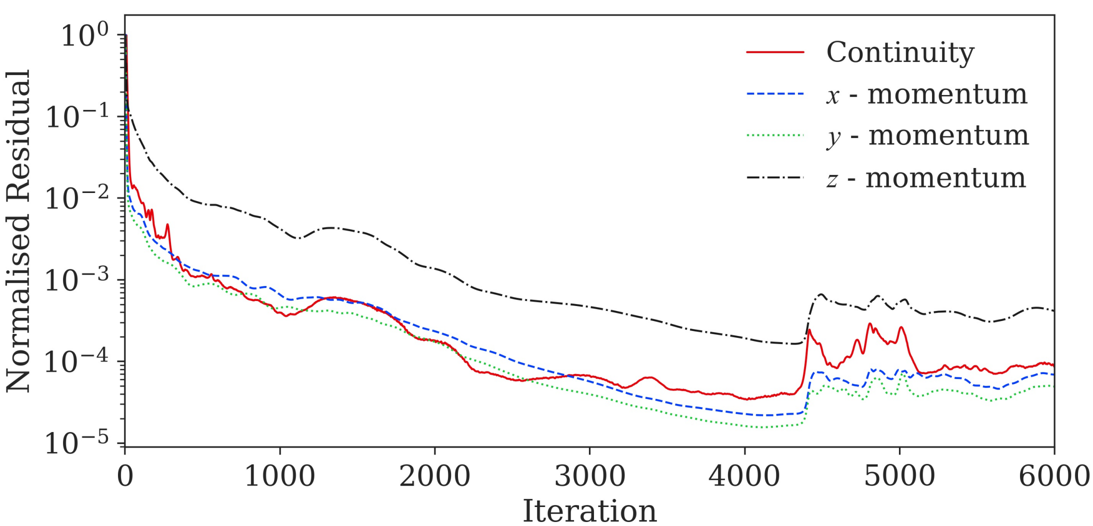

(b) EB $k - \varepsilon$

Figure 3.2: the residual history for the numerical evaluation of flow via two different turbulent model, namely Realizable $k - \varepsilon$ and EB $k - \varepsilon$ are shown above

The residual history for the numerical simulations performed using the Reynolds stress model on Grid C for various turbulent Reynolds number flows are shown in

Figure 3.3. Flow field corresponding to the Reynolds of 6843 requires the highest number of iterations to converge, approximately 8000 iterations, whereas the flow field corresponding to the Reynolds of 9504 requires the least amount of iterations to converge, approximately 3000 iterations.

A linear correlation between the number of iterations and the number of volume elements or the Reynolds number of flow can not be observed. Henceforth we evaluate

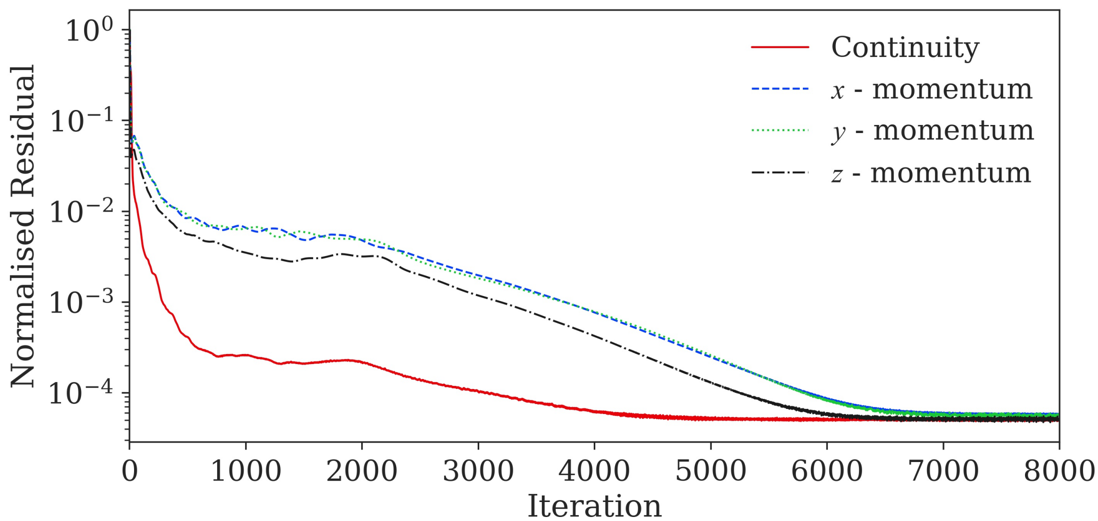

(a) $Re = 5069$

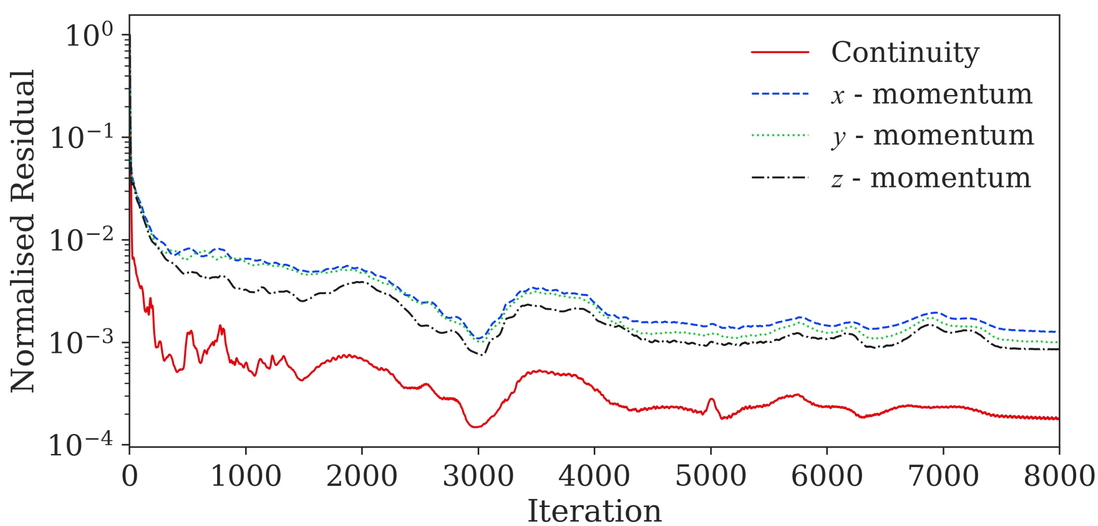

(b) $Re = 6843$

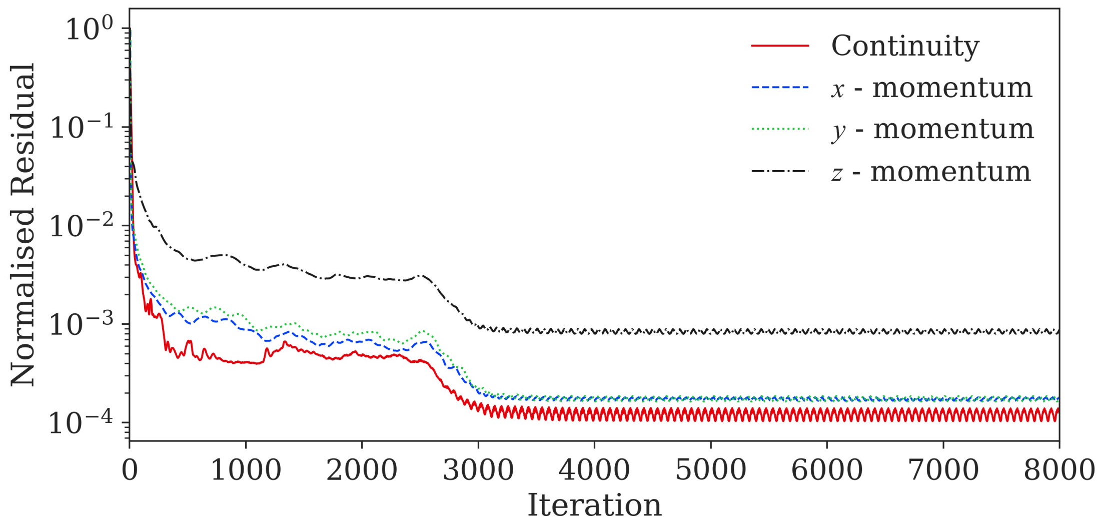

(c) $Re = 9504$

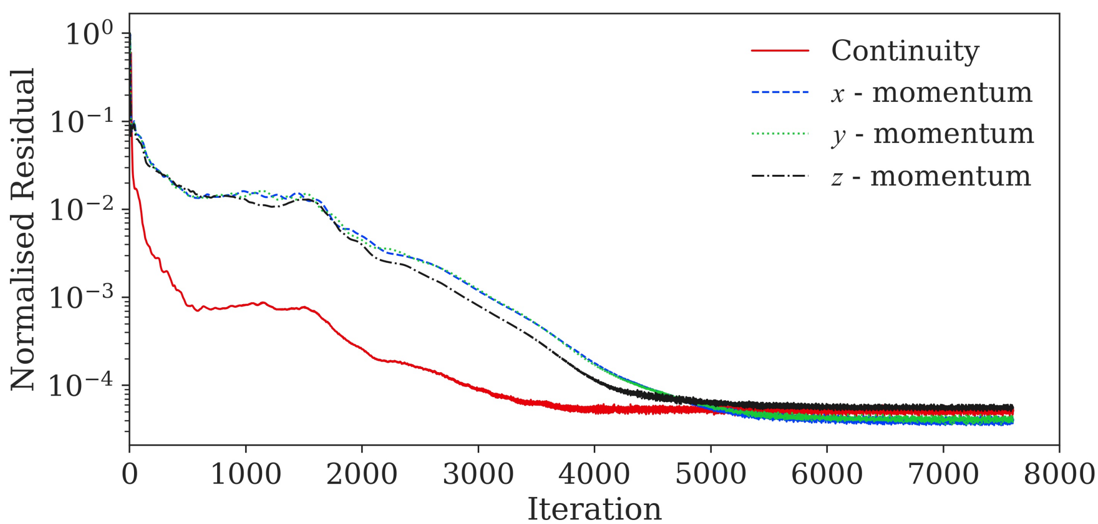

(d) $Re = 10391$

Figure 3.3: The residual history for the different Reynolds number flows in turbulent regime are shown above. RSM model was used to simulate flows across the Kenics mixer.

the volume average quantities across the computational domain in the upcoming section to assert more confidence in to the numerical simulations.

Volume Average Quantities

For all the simulated cases volume averaged velocity, υ, turbulent dissipation rate, $\overline{\varepsilon}$, and turbulent kinetic energy, $\overline{k}$, are evaluated at each iteration to track convergence. The volume averaged quantities are measured over the volume occupied by liquid in a computational domain starting at a normal distance of four diameters from the leading edge of first element and ending at a normal distance of four diameters from the leading edge of last element. The number of iteration for υ to reach an asymptotic point is dependent upon the number of grid elements. A total of 200 iteration are required on grid A for υ to become asymptotic for flow corresponding to Reynolds number of 12000. Grids B requires almost four times as many iterations as Grid A, while grid D requires approximately 4000 iterations for υ to become asymptotic, this can be seen in Figure 3.4a. The convergence of flow velocity amongst different turbulent modes is justified by Figure 3.4b. The EB $k-\varepsilon$ requires the highest number of iteration for υ to become asymptotic. The convergence of υ predicted by RSM at different Reynolds number is also shown in Figure 3.4c. The number of iterations required for volume average quantities to become asymptotic is positively correlated with the magnitude of Reynolds number. This can be clearly observed from the prediction of $\overline{\varepsilon}$ at different Reynolds number by Reynolds stress model depicted in Figure 3.5c. However, a correct solution is not necessarily followed by a converged numerical solution henceforth a grid sensitivity analysis using three different turbulent models on four different grids is performed for flow across Kenics mixer.

A similar trend is observed in $\overline{\varepsilon}$ and $\overline{k}$. Figure 3.5 shows the convergence of volume averaged turbulent dissipation rate for different grid size (Figure 3.5a), turbulent models (Figure 3.5b) and Reynolds number of the flow (Figure 3.5c).

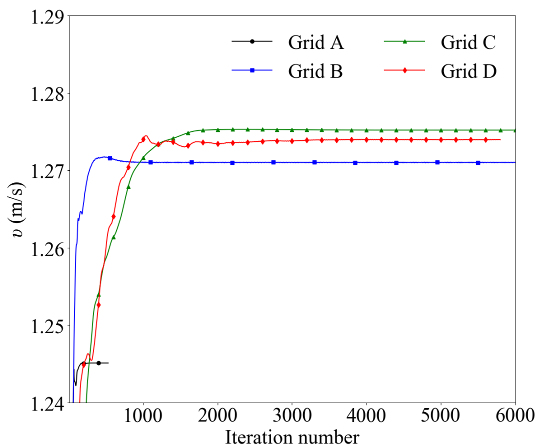

(a) Prediction of volume average velocity across iterations for different grids

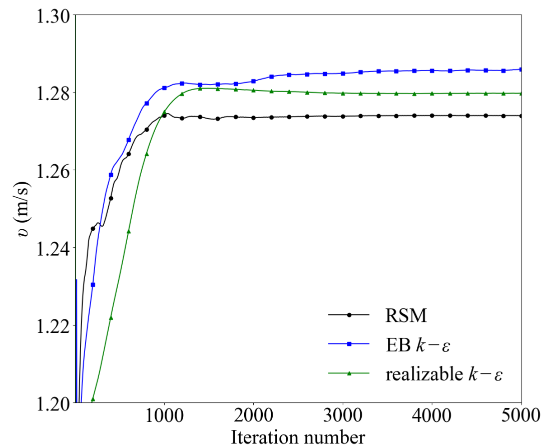

(b) Prediction of volume average velocity across iterations by different turbulent models on Grid C.

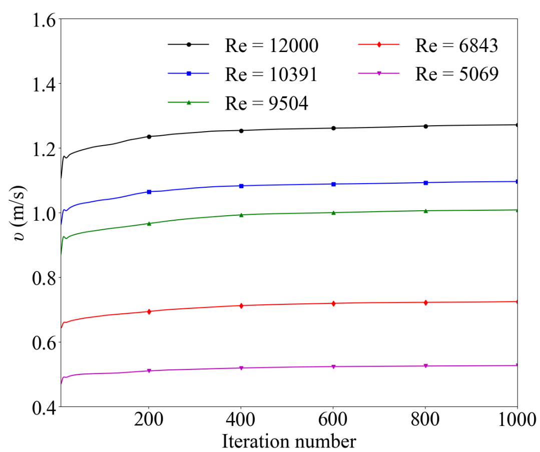

(c) Prediction of volume average velocity across iterations for different Reynolds number flow by RSM on Grid C.

Figure 3.4: Convergence of volume averaged velocity, υ.

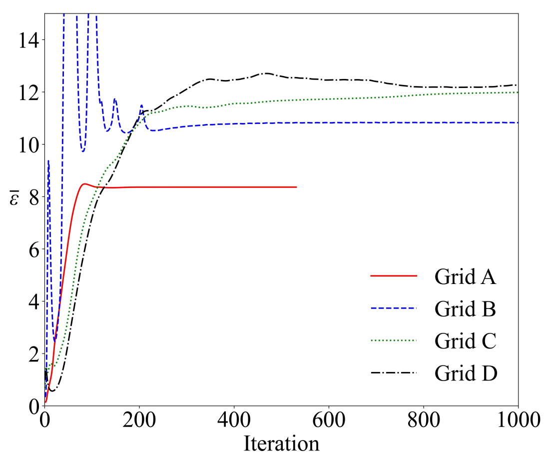

(a) Prediction of volume average dissipation rate across iterations for different grids.

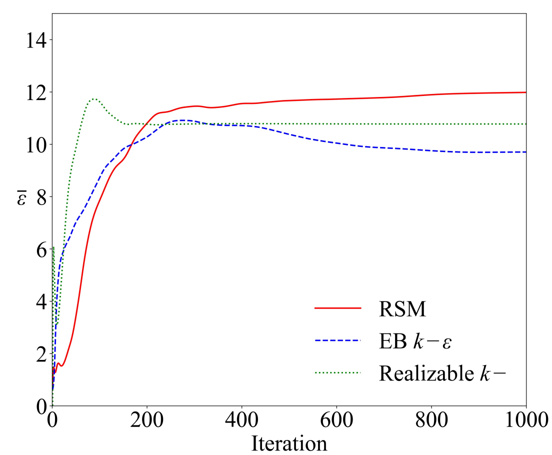

(b) Prediction of volume average dissipation across iterations by different turbulent models on Grid C.

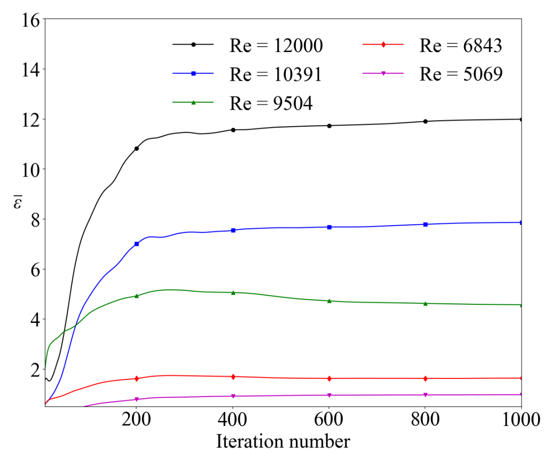

(c) Prediction of volume average dissipation rate across iterations for different Reynolds number flow by RSM on Grid C.

Figure 3.5: Convergence of volume averaged velocity, $\bar{\varepsilon}$.

3.2.2 Mesh Independence

Grid sensitivity analysis was carried out by numerically simulating flow at the highest Reynolds number of 12 000 on four grids A, B, C and D (see Figure 2) using the realizable $k-\varepsilon$, the EB $k-\varepsilon$, and the RSM turbulence models. The pressure drop across the mixer was evaluated as the difference between the average pressure at two cross-sections in the mixer: the upstream cross-section was located at a distance of D from the leading edge of the first element and the downstream cross-section was at a distance D from the trailing edge of the last element. The pressure drops as a function of the number of cells for different turbulence models are shown in Figure 3.6. Pressure drop, ΔP, levels off with increase of the total number of cells in each case which indicates that the numerical solution becomes mesh independent. The realizable and EB $k-\varepsilon$ models predict similar value of pressure drop equal to $4.6 \cdot 10^3$ Pa/m. The pressure drop predicted by the RSM model on grid D is $\approx 16\%$ greater than the one predicted by the other two models.

The radial velocity profiles along a vertical line placed at $z/D \approx 10.79$ mm after the edge of the sixth mixer element obtained on four grids are shown in Figure 3.7 (a). The RSM turbulence model was used in each case. The velocity profile obtained on grid A is not resolved. As mesh gets denser, the profiles follow similar trends. The Grid B and C fail to resolve peaks of velocity around $x/D \approx \pm 0.2$. This anomaly can be attributed to poor mesh quality in the core regions for Grid B and C when compared to Grid D.

The effect of the turbulence model on the radial velocity profile is shown in Figure 3.7 (b). Grid D was used for these cases. Overall, the trend is similar. The maximum percent deviation between the values is 7 %. The velocity profiles corresponding to EB $k-\varepsilon$ model and RSM reveals ups and downs in in the velocity magnitude in the core region unlike the Realizable $k-\varepsilon$ model. The presence of low velocity region at the center is revealed more boldly by the Reynolds stress model.

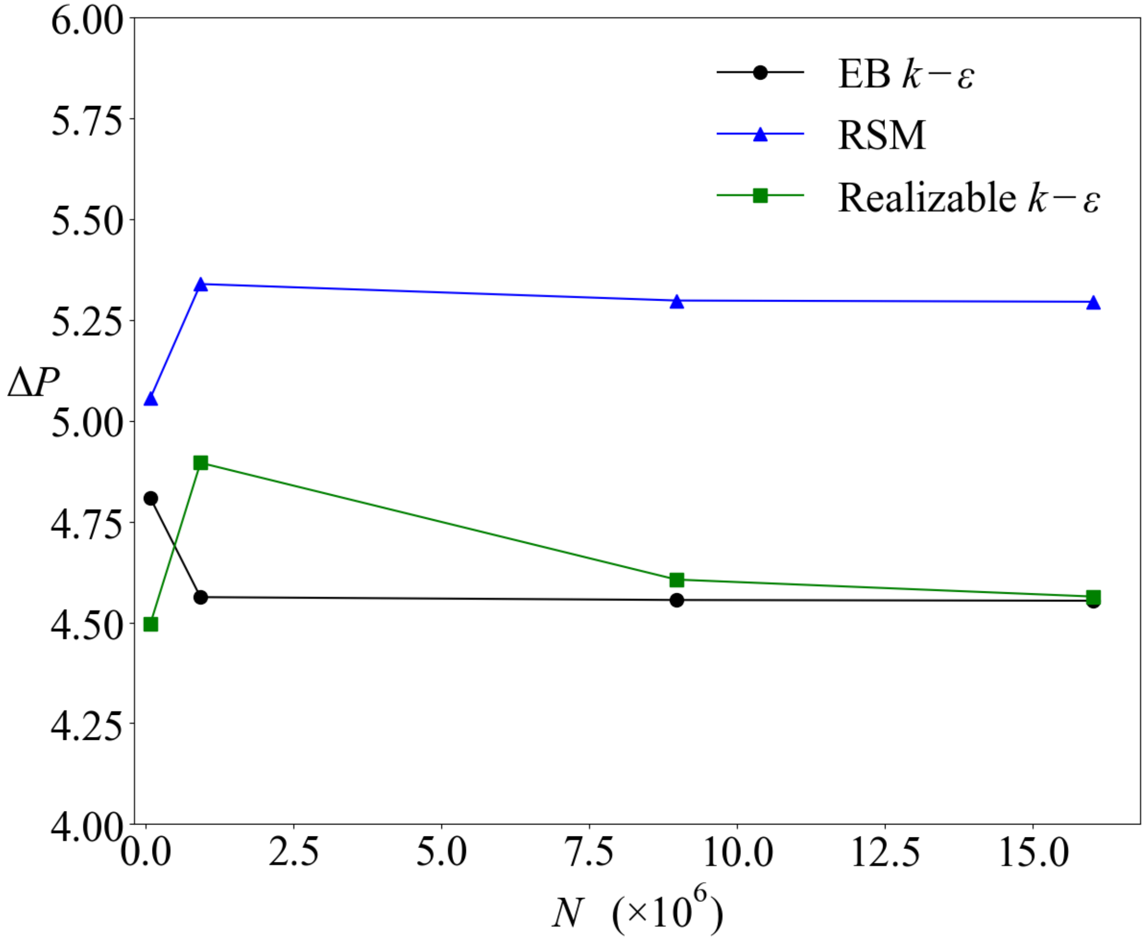

Figure 3.6: Pressure drop, ΔP, in kPa as a function of number of grid elements, N. The pressure drop becomes asymptotic as the N increases, for all three turbulent models.

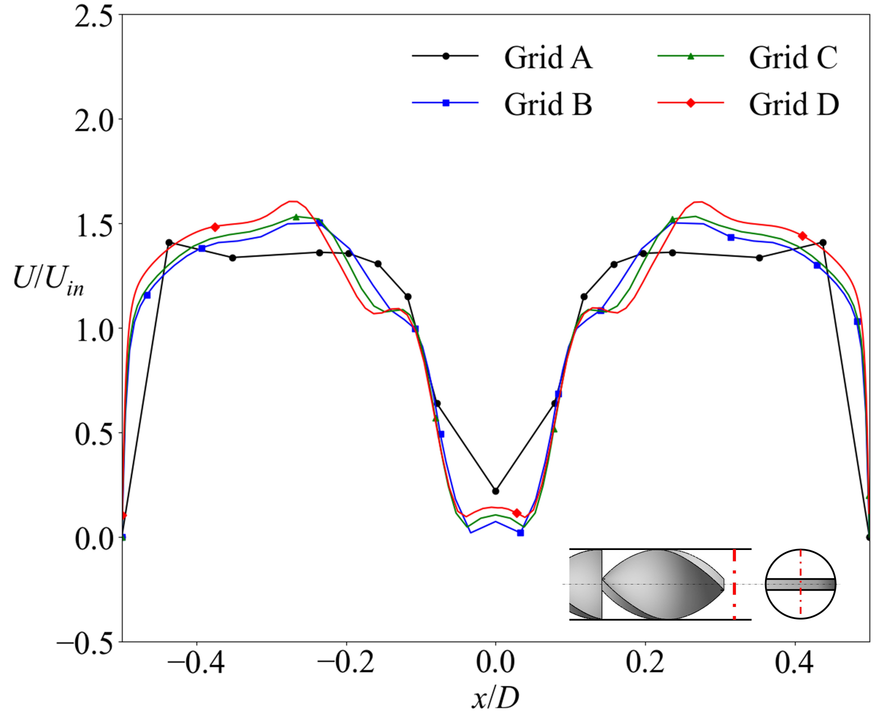

(a)

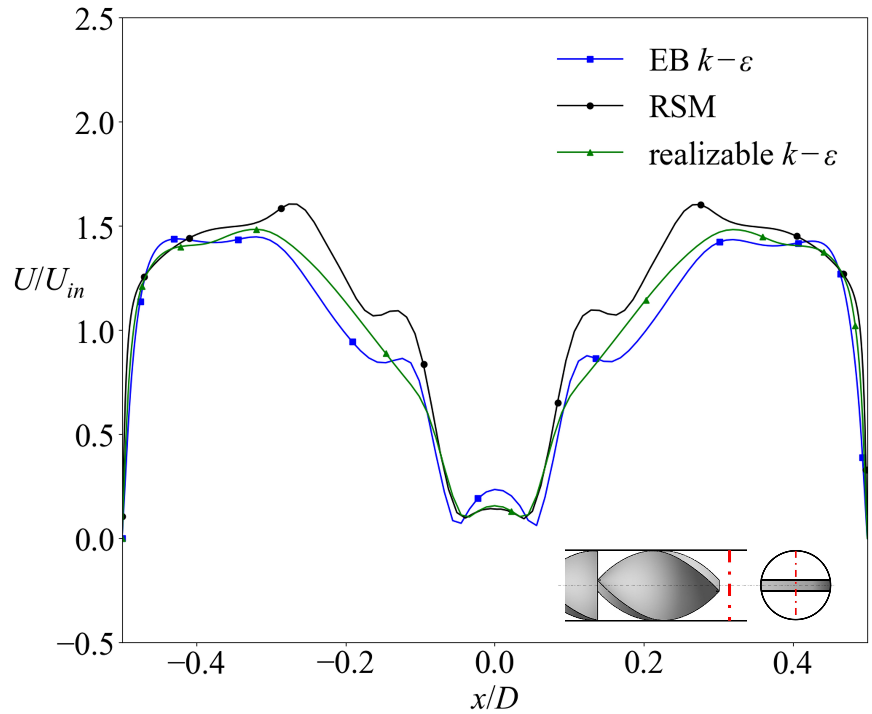

(b)

Figure 3.7: Velocity magnitude across the diameter of pipe passing through $z = 10.79D$ for flow corresponding to a $Re = 12000$. (a) prediction of velocity magnitude on different grids by Reynolds stress turbulence model. (b) Prediction of velocity magnitude by different turbulence models.

3.2.3 Estimation of Turbulence Quantities

The tracer concentration distribution is mainly determined by the local turbulent viscosity ratio, μ_T/μ (the ratio between turbulent viscosity and molecular viscosity of the fluid, Eq. (4), by turbulent kinetic energy, k, and by dissipation of turbulent kinetic energy, ε [14]. For that reason, we studied the effect of the mesh resolution and choice of the turbulence model on prediction of these turbulence quantities.

The numerical results for volume-averaged energy dissipation rate, $\overline{\varepsilon}$, turbulent kinetic energy, $\overline{k}$, and turbulent viscosity ratio, μ_T/μ, obtained using four grids and three turbulence models at Re=12 000 are shown in Table 3.1. The estimated $\overline{\varepsilon}$ increases with the grid refinement for three turbulence models. The change in the value of $\overline{\varepsilon}$ predicted by RSM levels off as the grid is refined. Coroneo *et al.* [14] outlines that the magnitude of average turbulent kinetic energy predicted by realizable $k-\varepsilon$ model across a corrugated mixer is higher compared to other turbulent models. In the present study we observe a similar trend. The magnitude of $\overline{k}$ predicted by realizable $k-\varepsilon$ is 3.3% and 14.1% greater than the one predicted by RSM and EB $k-\varepsilon$ model on grid D, respectively. The RSM model predicts results with a higher accuracy.

The predictions of maximum turbulent viscosity ratio, μ_T^{max}/μ vary widely with turbulence model. The realizable $k-\varepsilon$ predicts almost twice the μ_T^{max}/μ predicted by other two turbulent models. A larger degree of fluctuations is observed with change in grid refinement for realizable $k-\varepsilon$ model when compared to other two turbulent models.

Figure 3.8 shows color maps of turbulent kinetic energy on the cross-section located at the middle of the fourth mixer element. A significant difference of k values in the near wall region can be noticed in grid A and B. A thin layer of lower kinetic energy around the wall develops as the mesh is refined. The difference between the maximum and minimum turbulent kinetic energy tends to increase as the grid is refined. This can be further seen by appearance of an oval shaped local zone of high turbulent

Table 3.1: Dependence of turbulence parameters on spatial grid and RANS model for the flow at $Re = 12\ 000$

Grid	EB $k-\varepsilon$			RSM			Realizable $k-\varepsilon$		
	$\overline{\varepsilon}$	$\overline{k}$	μ_T^{max}/μ	$\overline{\varepsilon}$	$\overline{k}$	μ_T^{max}/μ	$\overline{\varepsilon}$	$\overline{k}$	μ_T^{max}/μ
A	5.75	0.034	71.45	8.36	0.033	92.91	4.8	0.027	130.97
B	8.46	0.04	70.27	10.82	0.036	67.79	10.77	0.035	132.67
C	9.23	0.033	68.43	12.10	0.037	68.85	11.50	0.037	112.26
D	11.16	0.035	70.50	12.34	0.039	62.87	12.50	0.04	151.46

kinetic energy on either side of the Kenics mixer as we move from coarse to refined grid. The local zones of lower turbulent kinetic energy depicted by dark blue regions also become clearer as the grid is refined.

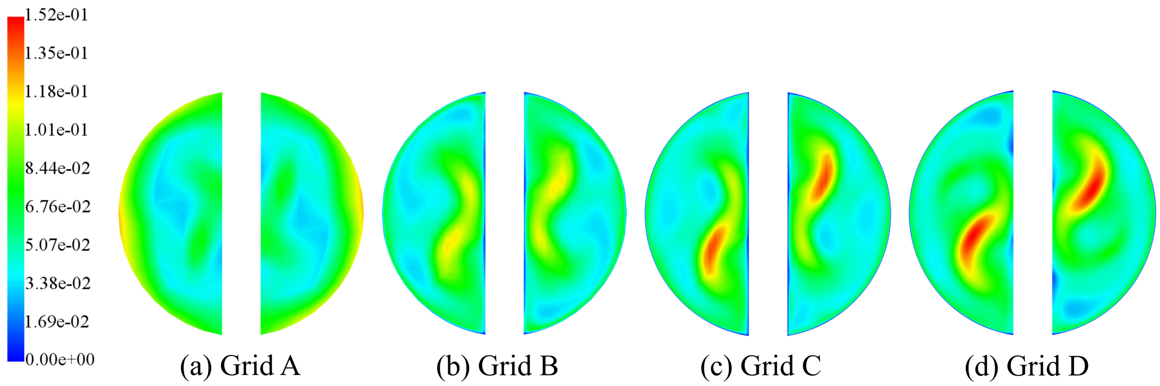

Figure 3.8: Contour plot of turbulent kinetic energy predicted by RSM on different grids on an $x-y$ plane located at $z/D = 6.2$. The Reynolds number of the flow is 12000.

Grid C and RSM turbulence model were used to perform simulations to assess the prediction of the average energy dissipation rate. The magnitude of $\overline{\varepsilon}$ obtained numerically is compared to the experimental value obtained by Forte *et al.* [38] for a six element Kenics mixer with similar geometrical dimensions. The authors used the equation suggested by Berkman and Calabrese [58] to estimate $\overline{\varepsilon}$ using the pressure drop across the mixer that reads as follows:

$$\overline{\varepsilon} = \frac{U_{in}\Delta P}{\rho L} \tag{3.1}$$

where L is length of the static mixer containing inserts and ΔP is the pressure drop measured across the length L.

The comparison of average energy dissipation rate ($\overline{\varepsilon}$) obtained by simulating flow using RSM is compared with experimental values obtained by Forte *et al.* [38] is shown in Figure 3.9. The data by Forte *et al.* [38] was extrapolated to a Reynolds of 12 000 (shown by a green dashed curve). The maximum deviation between the numerical and experimental results is within 9%.

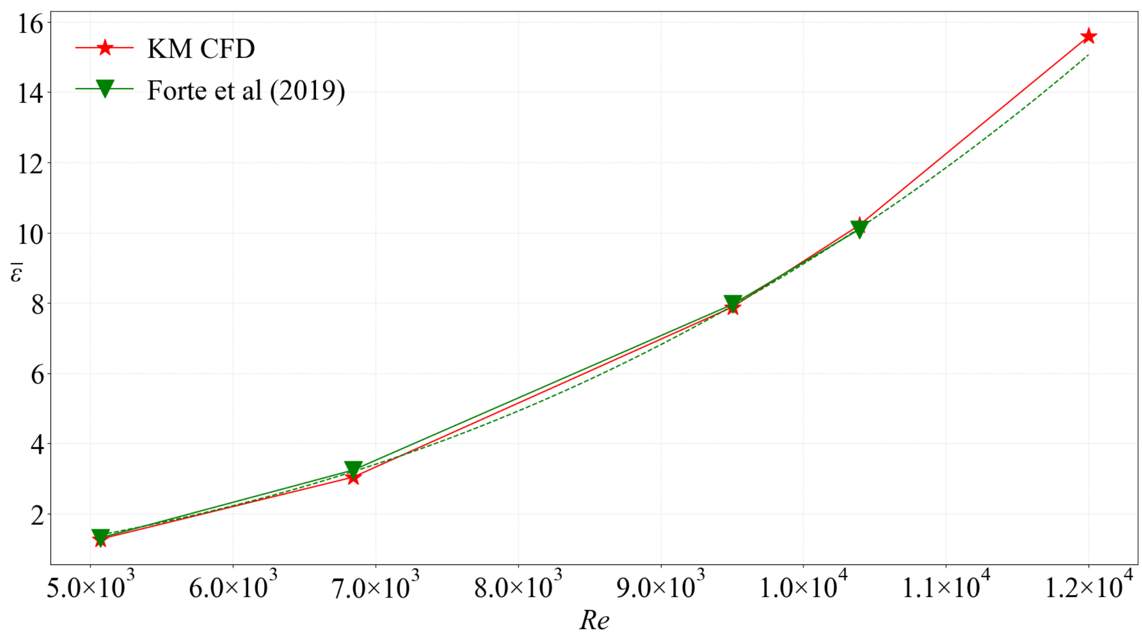

Figure 3.9: Average energy dissipation rate $\overline{\varepsilon}$ in m^2/s^3 as a function of the Reynolds number.

3.2.4 Pressure Drop

Pressure drop estimation is a crucial step for determining the pumping costs. It depends on the design of the inserts and the flow parameters. Pressure drop correlations for Kenics mixers with varied L_e/D ratio over a range of Reynolds numbers are available in References [10], [16], [59]–[64].

In this study, the pressure drop across the six element Kenics mixer is evaluated to validate our numerical code for a flow corresponding to the Reynolds number of 1, 10, 100, 1000, 5069, 6843, 9504 and 10391.

For Kenics elements, the flow across the static mixer is laminar if $Re < 50$ and turbulent if $Re > 1000$. In the intermediate range, $50 < Re < 1000$, complex but fairly reproducible behaviour can be expected [3]. The exact value of Re at which the transition of flow regime occurs is dependent on the design of inserts. For the Kenics mixers, the transition from laminar to turbulent flow begins at $Re = 43$ given the ratio of L_e/D is 0.8 and delays to $Re \approx 55$ for $L_e/D = 1$ [3]. The Kenics inserts used in this study have an aspect ratio of 1.77, hence it is safe to assume laminar flow below $Re = 100$ and a fully turbulent flow for $Re \geq 1000$.

The pressure drop across the mixer obtained for laminar and turbulent flow is shown in Figure 3.10a and 3.10b, respectively. The drop in pressure for $Re = 1$ is ≈ 0.17 Pa and ≈ 5300 Pa for the Reynolds number of 12 000.

At lower values of Reynolds number i.e. $Re < 100$, the pressure drop correlation provided by Pahl and Muschelknautz [60] appropriately describes the CFD data obtained in this study as the maximum deviation is within 2 %. At higher Reynolds number flows within the laminar and transitional regime, the CFD data on pressure drop is more appropriately described by Šír and Lecjaks [65]. The difference in the existing experimental data on pressure drop by Šír and Lecjaks [65] and Pahl and Muschelknautz can be explained by the variation in the geometry of the mixer. For instance, the aspect ratio i.e $AR = L_e/D$ of mixer used for study by Šír and Lecjaks [65]is larger than the one used in the study by Pahl and Muschelknautz [60]. A more detailed investigation into existing pressure drop correlations and reasoning for variation amongst them is provided by Kumar *et al.* [64].

For turbulent flow across the Kenics mixer the pressure drop correlations available in the existing literature are relatively scarce. The pressure drop obtained using CFD is compared to the reference data given in Refs. [16], [38], [64] on a logarithmic curve in Figure 3.10b. The rate of increment in pressure drop with respect to Reynolds number of the flow is similar to the one predicted experimentally by Stec and Synowiec [16] and Forte *et al.* [38]. The maximum deviation between the slope of a straight line on log-log plot for CFD data and the experimental data by Forte *et al.* [38] is less than 2 %. The deviation of CFD data on pressure drop from the experimental results of Stec and Synowiec [16] and Kumar *et al.* [64] can be attributed to the difference in geometrical parameters of the Kenics elements.

As a summary, based on model validation we will use grid C and RSM turbulence model to perform simulations of the flow in turbulent flow regime ($Re \geq 1000$). To resolve laminar flow, simulations are carried out on grid D to minimize the numerical diffusion. The choice of grid for simulating turbulent flow is dictated by the necessity to have wall refinement. For the case of laminar flows the grid with highest number of elements is used to reduce false diffusion. RSM was preferred over the other two models to simulate turbulent flow due to it more accurate prediction of pressure drop and turbulent quantities compared to other two turbulent models. The error in prediction of pressure drop, ΔP, by RSM is 38.67% whereas for the case of $k - \varepsilon$ based turbulence models it is $\approx 47\%$. The error can not be considered significant as the experimental values of ΔP are subject to a 20 percent deviation due to presence of syringe that was used to inject the dispersed phase in case of experiments. In case of CFD we did not have such an obstacle and henceforth it is safe to assume that the ΔP predicted by the turbulence models is within acceptable limits.

The pressure drop across a homogeneous, isothermal, incompressible, Newtonian fluid flow in a circular tube can be given by Equation 3.2.

$$\Delta P = \frac{2f\rho U_{in}^2}{D} L = \frac{2f\rho U_{in}^2}{D} L_e N \tag{3.2}$$

Where, L is the length of the tube with diameter D. N refers to the number of Kenics inserts and L_e is the length of single Kenics element. Note that $U_{in} = \frac{Re\mu}{\rho D}$. The friction factor or f generally a function of Re is determined experimentally or using CFD. For a laminar flow across smooth pipe $f = Re/16$, for turbulent flow $f = 0.079Re^{-0.25}$. Though for a pipe with obstruction or say Kenics inserts the magnitude of f will be higher and the transition of flow from laminar to turbulent will occur at lower Reynolds number. In general it has been observed that the flow behaviour static mixer is laminar for $Re < 50$ and turbulent for $Re > 1000$. In the intermediate range, $50 < Re < 1000$, complex but fairly reproducible behaviour can be expected [3]. Although exact value of Re at which transitions of flow regime occur are dependent upon the design of inserts. For Kenics mixers the transition of laminar to turbulent begins of 43 given the ratio of L_e/D is 0.8 and delays to $Re \approx 55$ for $L_e/D = 1$. The Kenics inserts used for analysis in this article have an aspect ration of 1.77, hence it is safe to assume a laminar flow below $Re = 100$ and a turbulent flow above $Re = 1000$.

Similar correlations for the pressure drop across the Kenics mixer in terms of friction factor have been established for a range of Reynolds number. Table 3.2 presents an extensive list of pressure drop correlations for Kenics mixer. It must be noted that the geometry of Kenics mixer in all the mentioned literature is not similar. A comparison of friction factor predicted by the CFD and existing literature across six element Kenics mixer subjected to laminar flow is shown in Figure 3.10a. The literature available on the pressure drop correlations for turbulent flow is almost non existent as the high dependency of pressure drop on the geometry mixers along with a myriad number of other factors makes it impossible to predict a trend that fits all. The work by Song and Han [10] to develop a general correlation for pressure drop across a Kenics mixer predicted a constant friction factor for flows corresponding to a Reynolds's number above 3,143, given aspect ratio of the mixer ($AR = L_e/D$) is 1.77. However Song and Han [10] assume a zero thickness inserts and henceforth fails to provide a realistic measure of pressure drop. Kumar *et al.* [64] also provides a pressure drop correlation based on friction factor for a flow corresponding to a Reynolds's number between 1 and 25000. However, the experimental data is obtained across a standard Kenics mixer ($AR = 1.5$) with either 3, 9 or 25 elements. Some of the recent work by Stec and Synowiec [15] on comparison of performance by three different types of static mixer and the study of Forte *et al.* [38] though focused on oil-water dispersions, provide an estimate of pressure drop in a turbulent flow across a six element Kenics mixer but both fail to establish a general correlation for pressure drop. The pressure drop predicted using CFD across a six element Kenics mixer for a turbulent flow is compared with the pressure drop predictions by the above mentioned literature in Figure 3.10b.

Table 3.2: Friction factor correlations for Kenics mixer

Correlation	Reynolds Number	Aspect Ratio	Reference
$f = \frac{77.76}{Re} + \frac{10.88}{Re^0.5}$	$Re < 1000$	1.5	Grace (1971)[59]
$f = \frac{85.5}{Re} + 0.34$	$Re < 2300$	1.5	Sir and Lecjaks (1982)[65]
$f = (213.5 + 224/AR)/Re + 4.775/AR - 0.549$	$Re < 2300$	2.0 - 5.0	Lecjaks et al. (1987)
$f = \frac{115.2}{Re} + 0.5$	$Re \leq 20$	1.36	Cybulski and Werner (1986)[61]
$f = \frac{6.592}{Re^{0.5}}$	$100 \leq Re \leq 1000$	1.36	Cybulski and Werner(1986)[61]
$f = 118.56/Re + 16.64Re^{-0.2}/AR^{1.04}$	$Re \leq 700$	1.5 - 2.5	Joshi et al. (1995)[62]
$f = 320Re^{-0.86}AR^{3.889}$	$Re \leq 100AR^{2.15}$	1.5 - 2.5	
$f = 32Re^{-0.36}AR^{2.814}$	$100AR^{2.15} \leq Re \leq 1000AR^{2.15}$	1.5 - 2.5	H.S. Song et al. (2005)[10]
$f = 2.449 \times 10^{-4}Re^{0.75} + 1.16051Re^{-0.25}$	$100 \leq Re \leq 10^4$	1.5	V. Kumar et al. (2008)[64]

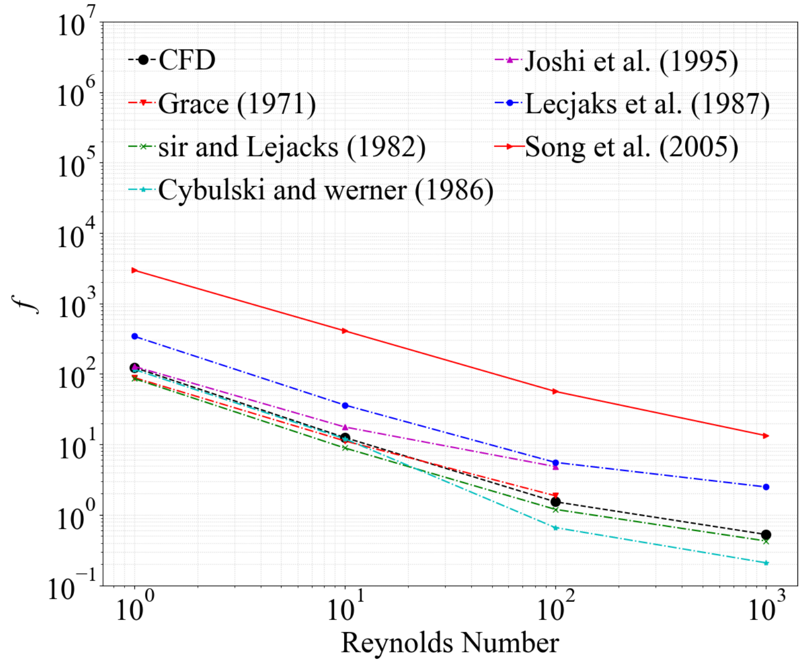

(a) friction factor, $Re \leq 1000$

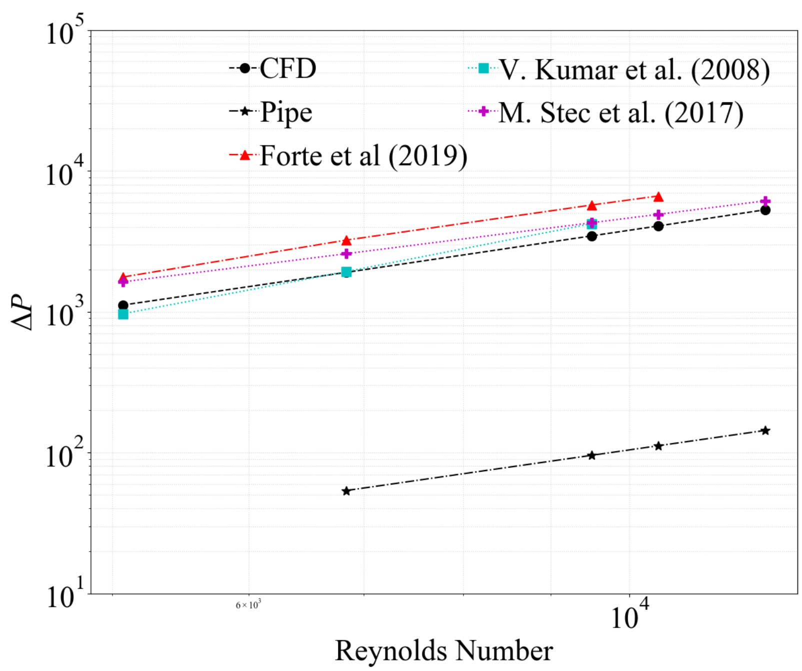

(b) Pressure drop across a six element Kenics mixer, $5000 \leq Re \leq 12000$

Figure 3.10: Comparison of pressure drop across the Kenics mixer for all simulated cases.

3.3 Visualisation of Flow in Static Mixer

Velocity vector plots in a cross section located in the middle of the fourth mixer element (z = 78.75 mm) at different Reynolds numbers are shown in Figure 3.11. An organized flow is seen in Figure 3.11(a) for $Re = 1$. The transition from laminar to turbulent flow results in splitting of a single zone of strong cross sectional flow into multiple zones of high and low velocity as seen in Figures 3.11 (b) and (c) for Re = 1 000 and Re = 12 000, respectively. A strong cross sectional flow is also observed in the corners of the mixer elements. This flow gets stronger with the increase in axial flow velocity which is consistent with the observations reported by Rahmani *et al.* [23].

The velocity profiles corresponding to the Reynolds number of 10, 100, 1 000 and 12 000 are plotted along different radial lines perpendicular to the surface of the third mixer element in Figure 3.12. The axial velocity magnitude, U_z, at any given location is normalized by the inlet velocity, U_{in}. The increase in velocity magnitude as we move away from the leading edge towards the trailing edge of the element can be observed for each Reynolds number. For $Re = 10$, the velocity profiles are close to parabolic and become fully developed within a distance of $0.25L_e$ from the leading edge of the element. As the Reynolds number increases to 100, the profile of velocity deviates from the parabolic shape, with its peak shifted away from the wall of the mixer element. The variation in flow profile diminishes after a distance of $0.5L_e$ from the leading edge of the mixer element. For turbulent flows at Re = 1 000 and Re = 12 000, the velocity profiles flatten out along with the reduction in the thickness of the boundary layer profile closer to the walls.

The presence of stagnation zones or low velocity regions within the mixer are visually demonstrated in Figure 3.13 by plotting the scalar plots of velocity magnitude along a normal plane passing through the center of the mixer. The plots are normalized by U_{in}. The stagnation zones can be seen at the leading and trailing edges

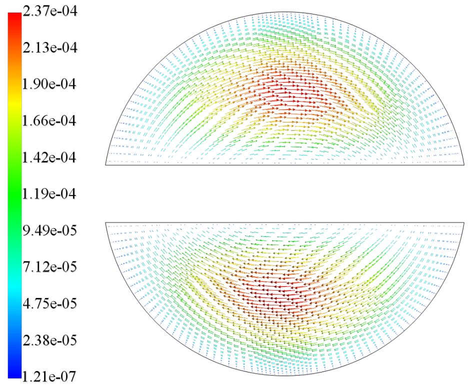

(a) $Re = 1$

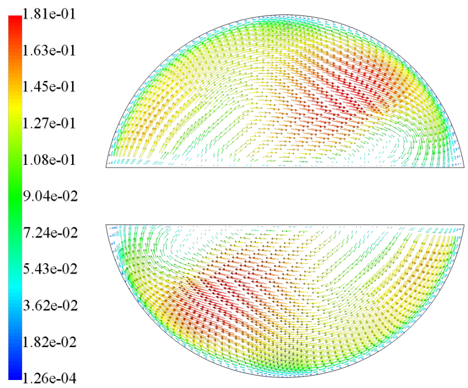

(b) $Re = 1000$

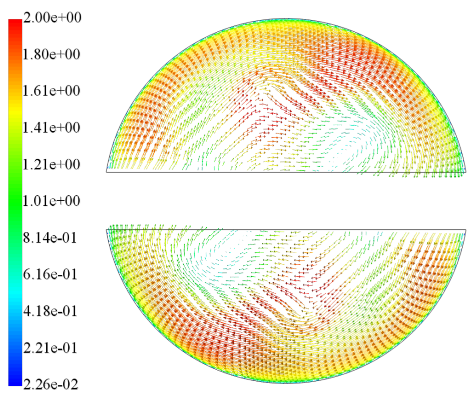

(c) $Re = 12000$

Figure 3.11: Vector plots of the velocity magnitude on an $x - y$ plane located at the middle of the fourth element, $z/D \approx 6.2$. Note the difference in the color bar scale.

of the elements (blue areas). There is a formation of a large stagnation zone at the end of the sixth element (see red squared area in Figure 3.13). As the Reynolds number of the flow increases, the length of this stagnation zone also increases. This effect is shown in Figure 3.14 (b) where a magnitude of negative axial velocity at the center increases as the Reynolds number of the flow increases (see Figure insert). The presence of negative axial velocity depicts flow in opposite direction indicating development of a re-circulation zone behind the trailing edge of the sixth element.

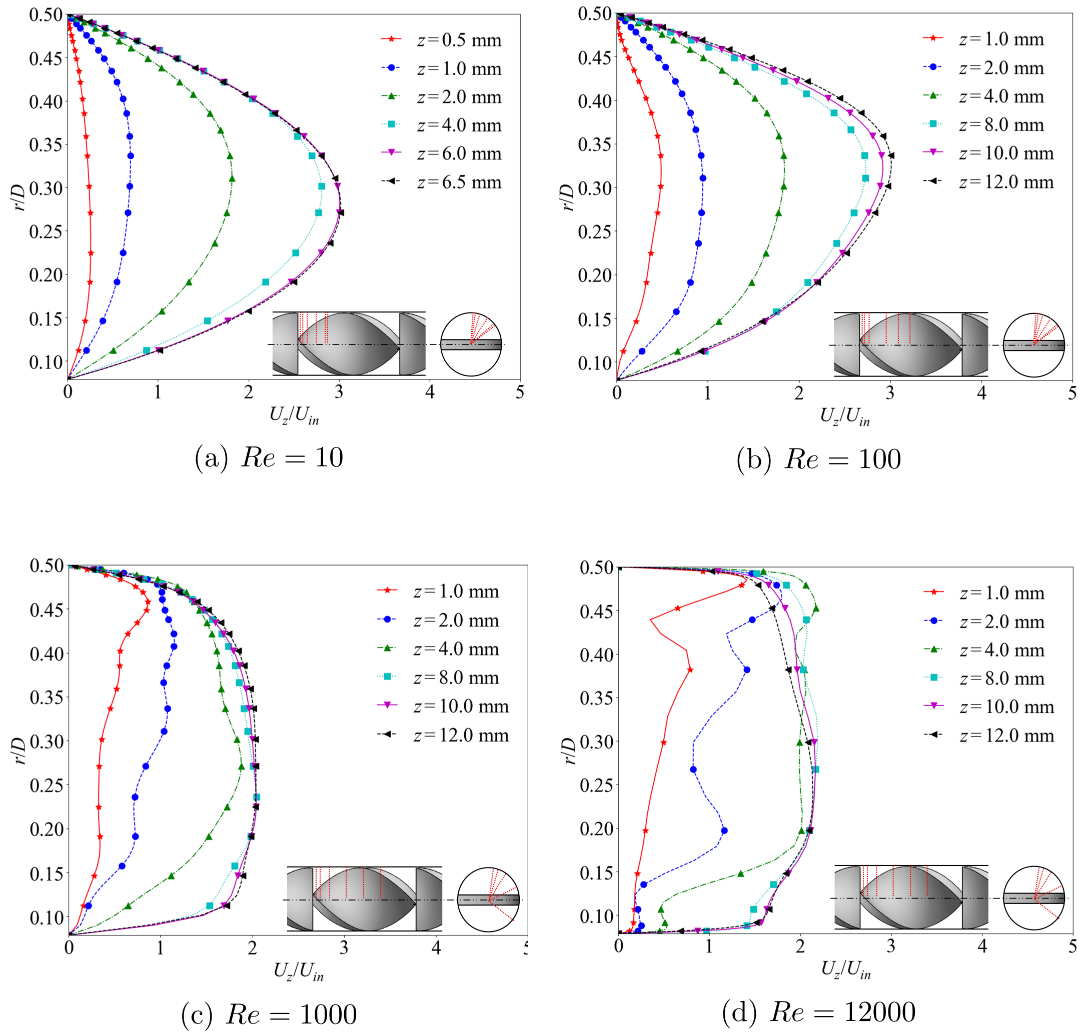

(a) $Re = 10$ (b) $Re = 100$

(c) $Re = 1000$ (d) $Re = 12000$

Figure 3.12: Scaled axial velocity distribution, U_z/U_{in}, across the radial lines normal to the surface of the third Kenics element. The Figure shows development of velocity profile as we move away from the leading edge of the Kenics element for different Reynolds number flows.

A strong cross sectional flow is demonstrated by red regions in a scalar plot corresponding to $Re = 1$ (see Figure 3.13). As the Reynolds number increases, the red regions fade. For the case of laminar flow regime, the strength of the cross sectional flow increases with the increase in Reynolds number Liu. To quantify this effect, we calculate the ratio of maximum value of axial velocity to the inlet velocity (U_z/U_{in}). It is 1.96 for $Re = 1$ and increases to 2.2 and 2.53 for flows $Re = 10$ and 100, respectively. For $Re = 1000$ the ratio drops to 1.69 and reduces to 1.5 for flows in the turbulent regime. Figure 3.14 shows U_z/U_{in} along a line at $z/D = 10.79$ mm for the flow in the Kenics mixer and pipe flow. For the flow in the Kenics mixer at $Re = 1\,000$ the axial strength of the flow reduces and the profile of velocity flattens as discussed above. For the case of turbulent flow a flattened velocity profile across the pipe is observed. The variation in the axial velocity profile at different Reynolds numbers is almost none. A closer look however reveals that the increment in Reynolds number is resulting in a more flatter curve as the slope of the profile closer to the walls becomes steeper. This phenomenon can be seen more clearly in a small plot located at the bottom right corner of the Figure 3.14b.

For the case of turbulent flow across the Kenics mixer the magnitude of U_z/U_{in} is approximately 1.3 times higher than that of a pipe flow due to presence of Kenics elements. For a laminar pipe flow the maximum value of U_z/U_{in} remains constant at 2 [39].

The Kenics mixer is designed to homogenize the fluid by redistributing it in radial and tangential direction [3]. The mixing elements with clockwise and counter clockwise helical twists placed alternatively promote rotation of fluid such that it follows the helical twist in the Kenics element and hence, increases the tangential component of velocity, U_{tan}. For convection dominated flows U_{tan} will approach zero at some distance after the mixer. The higher the Re, the longer this distance is. Figure 3.15 shows U_{tan}/U_{in} on a line passing through $x = D/4$ and $y = D/4$, along the flow direction for the flows corresponding to Reynolds numbers of 1, 100 and 12 000. At $Re = 1$, the tangential velocity before and after the mixer approaches zero. For $Re = 100$ and higher, a substantial amount of momentum is transferred into the

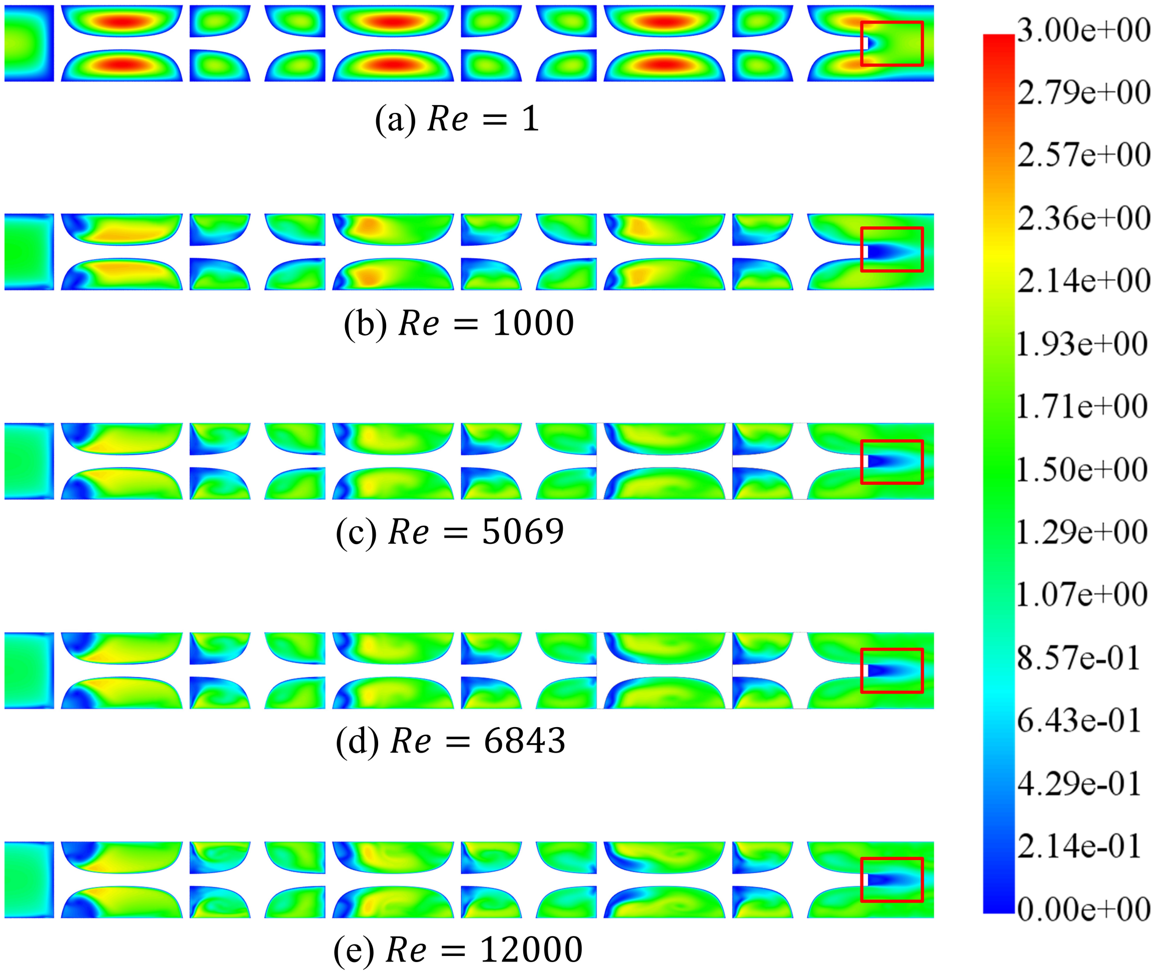

Figure 3.13: Scalar plots of normalized velocity magnitude (U/U_{in}) on an $x-z$ plane passing through the center of the pipe. The plots reveal the variation in zones of stagnant fluid as the flow regime changes from laminar to turbulent.

tangential direction, hence, promoting mixing even downstream the mixer.

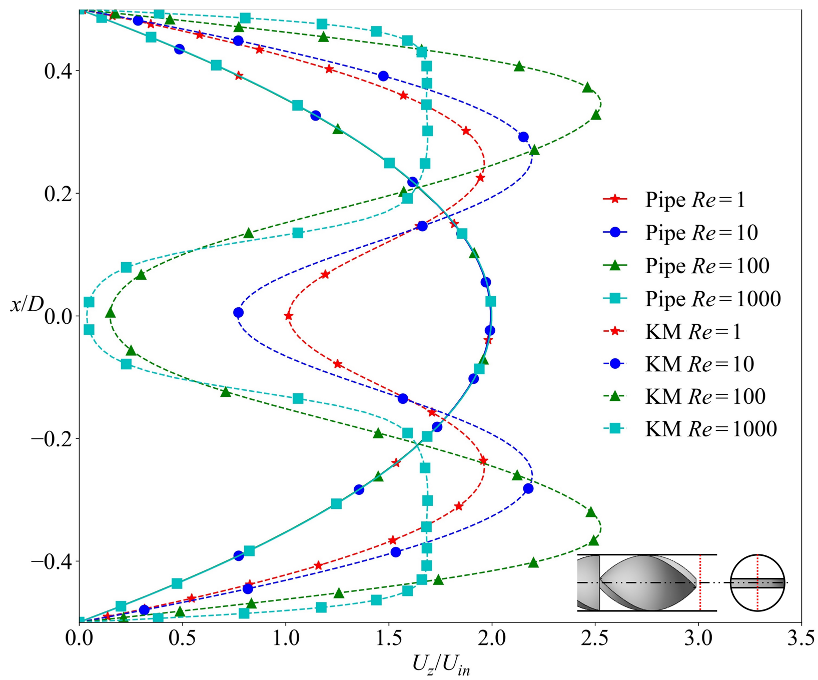

(a)

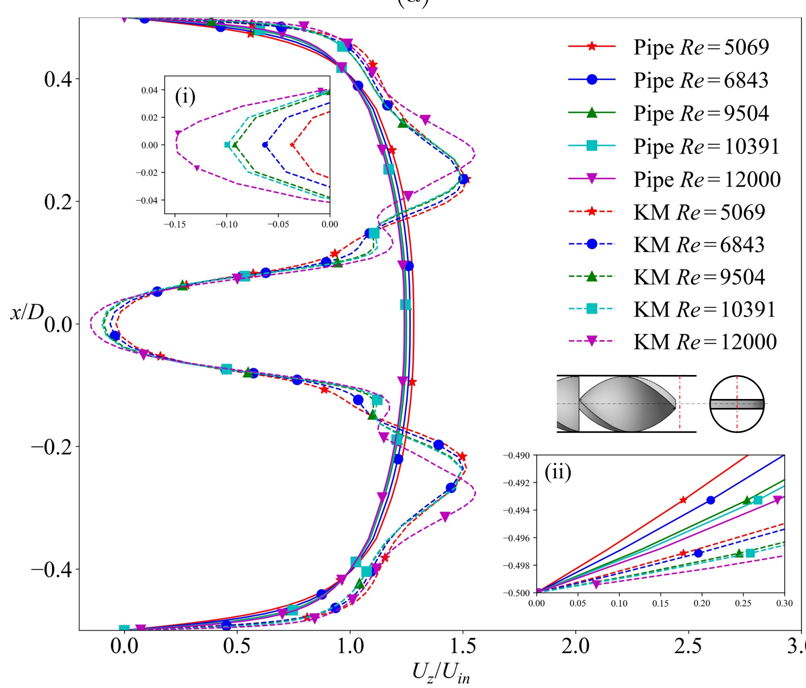

(b)

Figure 3.14: Profile of mean axial velocity, u_x, across the diameter of pipe at $z/D = 10.79$. (a) shows velocity profiles of pipe and Kenics mixer flows corresponding to $Re \leq 1000$ and (b) shows the same for $Re > 1000$.

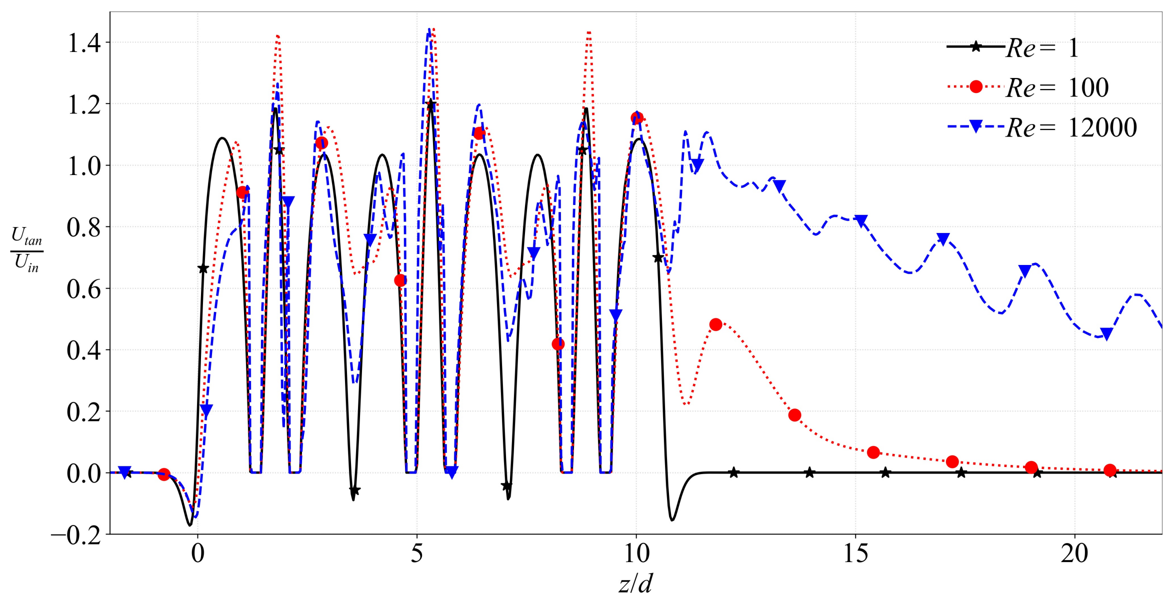

Figure 3.15: Scaled tangential velocity (U_{tan}/U_{in}) profiles as a function of normalized axial coordinate (z/D). The presence of Kenics elements induce a periodic rise and fall in the tangential velocity across the mixer. The variation in the behaviour of tangential velocity after the Kenics mixer across different flow regimes can be noticed.

3.4 Summary

In the current section we verified and analysed the flow field obtained via numerical simulation performed using STAR-CCM+ [37]. A convergence of numerical simulations was assured by tracking residuals and the volume averaged quantities, volume average velocity, turbulent dissipation rate and turbulent kinetic energy.

The numerical simulations have been verified by performing a mesh independence analysis and comparing the values of pressure drop and turbulent dissipation rate with the experimental results. Turbulent dissipation rate, turbulent viscosity ratio and turbulent kinetic energy were measured on four different grids for three different turbulence models. The susceptibility of mesh and turbulence model on prediction of these turbulent quantities is also identified. It is observed that the Reynolds stress model provided more consistent results at the expense of higher computational resources. The visualisation of velocity field using scalar plots reveals the presence of regions with low velocity which could be potential zones for adverse mixing phenomena. The tangential velocity imparted to the fluid due to the helical shape of the Kenics element is also visualised via a line plots. The helical motion of fluid can be identified as one potential reason for good radial mixing while creating small patches of adverse mixing.

Chapter 4

Mean Age Distribution

4.1 Overview

In the current chapter we touch base on the previous work of Liu [33] by visualising mean age distribution on a range of Reynolds number within the laminar flow regime. We also extend the analysis to turbulent flows by evaluating mean age distribution over a range of Reynolds number within the turbulent flow regime (Refer to Table 2.1). The first section presents a visual comparison between the mean age distribution obtained for a range of Reynolds number in Laminar and turbulent flow regime. This is followed by the analysis of frequency distributions of mean age. The final section presents data driven analysis with the use of machine learning algorithms, to deduce zones of higher and lower mean age and find a correlation between the mean age distribution and velocity magnitude.

4.2 Spatial Distribution of Mean Age

The spatial distribution of the mean age on a $(x - z)$ plane passing through the center line of the mixer (that is $y = 0$) is shown in Figure 4.1 for different Reynolds numbers. The distribution is normalized by the average molecular age at the outlet. For clear visualisation, the colorbar is cut at $0.5\overline{\alpha_e}$. At creeping ($Re = 1$) and laminar ($Re = 10$) flows, there are distinct striations formed by older aged fluid (thick red areas stretching in the direction of the flow) which is consistent with observations made by Liu [57]. The striations are carried forward in the axial direction with minor or no distortion even downstream of the mixer. This indicates that the axial mixing is negligible. As the Reynolds number increases to $Re = 100$, the striations get distorted as seen in Figure 4.1 (c). Liu [57] attributes this disappearance of simple lamellar structures and appearance of chaotic stretching and folding to the development of the secondary flows. It is necessary to note that the distortion of striation at $Re = 100$ continues even after the sixth element.

At $Re = 1000$, the striations are no longer visible as they are instantly distorted by the strong recirculating regions and secondary flows within the first mixer element. The regions of older aged fluid become scarce.

As the Reynolds number of the flow is further increased, a strong separation between the younger and older aged fluid created by the presence of striations in the laminar flows disappear. The disappearance of regions of older aged fluid from the mean age distribution of turbulent flows indicates a higher degree of axial mixing. This fact will be later quantified in the paper. Overall, just based on scalar plots given in Figure 3.13, the distribution of the mean age does not change substantially as the Reynolds number is above $Re = 5069$. However, there are important differences occurring after the mixer and these are related to the development of the stagnation zone.

The development of the stagnation region after the sixth element is shown by a black box in Figure 4.1. An older aged fluid is seen within the stagnation zone for each Reynolds number. At $Re = 1$ and $Re = 10$, a long streak of older fluid at the center surrounded by fluid of younger age extends in the direction of the flow without any radial or axial distortion. This happens because the viscosity of the fluid dominates over convection and, hence, prevents the distribution of momentum within the fluid molecules. At $Re = 100$, the distribution of the mean age in the stagnation zone is distorted. The reason for this distortion can be attributed to convection [57].

At $Re = 1000$, there is a small pocket of the older fluid stretched in the direction

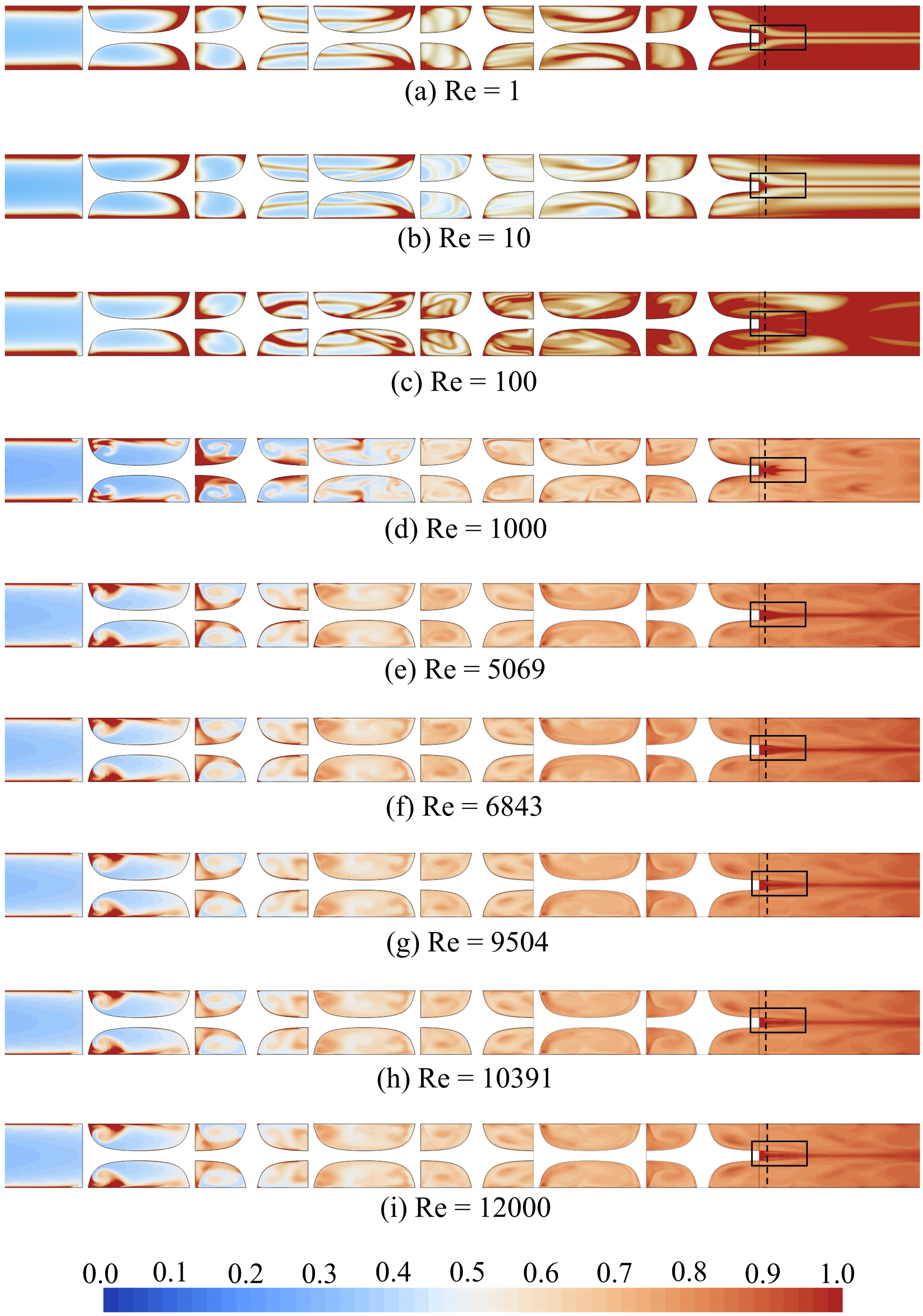

Figure 4.1: normalized mean age distribution, $a/0.5\overline{\alpha_e}$, in the $(x-z)$ plane passing through the center line of the mixer.

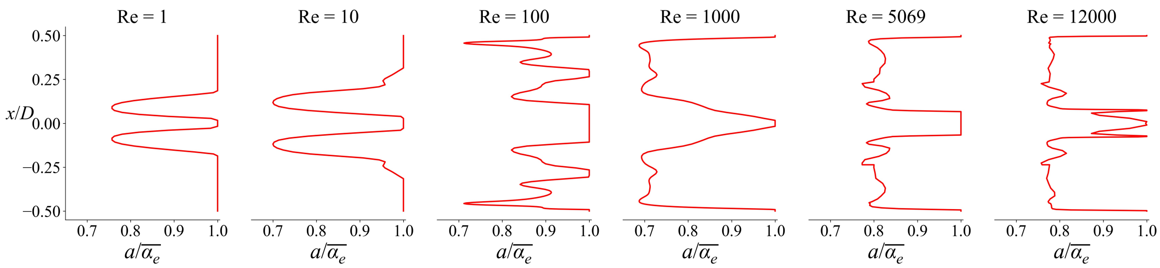

Figure 4.2: Magnitude of scaled mean age, $a/\overline{\alpha_e}$, across the black dashed line shown in Figure 4.1 is shown for different Reynolds number flows. The black dashed line runs across the diameter of the pipe at a normalized axial coordinate equal to $z/D = 10.79$.

of the flow resembling a stagnation region behind a solid object. As the flow becomes more turbulent (Re increases), the length of the stagnation region increases. Therefore, for turbulent flows, we observe a long streak of older aged fluid starting at the trailing edge of the sixth element. The mean age along the $y-$axis at $z = 10.79D$ which falls into stagnation zone is shown in Figure 4.2. The age distribution close to the center of the pipe corresponding to $Re = 5069$ and $Re = 12000$ is different. For the case of $Re = 5069$ the magnitude of $a/\overline{\alpha_e}$ at the center remains close to unity. At $Re = 12000$ we observe peaks and valleys in the distribution of mean age. It is important to reveal these regions of older aged fluid created due to stagnancy as they can affect the quality of mixing [4].

To analyse the change of simple lamellar structures into chaotic folding structures, evolution of the spatial distribution of the mean age within mixer elements is presented in Figures 4.3 to 4.11 for all cases. The values of mean age were normalized by the average molecular age of the fluid at the respective cross section. For better visualisation of striations, the colorbar cut off is at $a/\overline{\alpha_z} = 2$. The rows present variation in mean age spatial distribution as the flow passes through each mixer element. Each row contains eleven cross sections within a given element.

The first element of the mixer splits a single fluid stream into two as seen in the first row of Figure 4.3 and 4.4. As these streams flow, a boundary layer develops along the element's walls and give rise to a layer of older fluid at the walls. As these two streams approach the second element, the wall layer of older fluid remains and a new wall layer close to walls of the second mixer element is created along with division of existing region of younger fluid (see second row of the Figure 4.3 and 4.3).

As we move from left to right, four regions of younger fluid, two on either side of the Kenics element, stretch and elongate. As we descend to the bottom, the number of striation of younger fluid doubles (see Figure 4.3 and Figure 4.4). The doubling of striations ceases as the fluid reaches the fifth element. In fact, the number of striations across the fifth and the sixth elements are equal. Liu [57] has observed a similar phenomenon and claims that the false diffusion is responsible for the broadening of striations and the inhibition of the doubling of striations after the fourth element.

As the Reynolds number of the flow is increased to 100, the inertial forces appear to dominate over the viscous forces. The distribution of the mean age across the first element is similar to the one observed for the laminar flow. As we move from left to right within the second element, it is noticeable that the striation not only stretch but also bend inwards in the clockwise direction (refer to the second row of Figure 4.5). The inward bending of striations in the counterclockwise direction can be seen in the third row. The direction of bending of striation coincides with the rotational motion of the fluid within the element. As we move from top to bottom, the striations fade away due to false diffusion [57]. However, pockets of younger and older fluid can still be seen. As the fluid advances further in the direction of the flow, the pockets of older fluid disappear and larger region of cross section is filled with fluid having age similar to molecular age at that cross section. At the end of the sixth element (the image on the far right in the last row) two oval regions of younger fluid (dark blue regions) diagonally opposite to each other can be seen.

At Re = 12 000, the flow becomes chaotic and the regions of older aged fluid almost disappear. The mean age distribution of fluid in the first element shown at the top row of Figure 4.11 denotes the evolution of inwardly folded circular structures on either side of the element. Notice that these structures develop in the diagonally

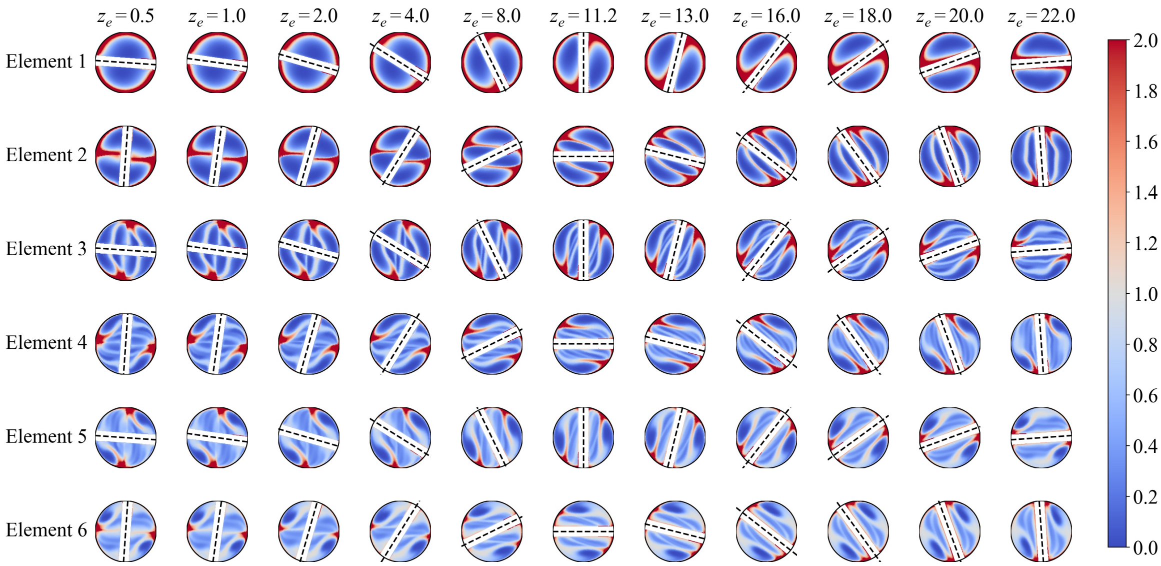

Figure 4.3: The evolution of spatial distribution of mean age distribution for flow corresponding to $Re = 1$ across the Kenics mixer, z_e represents the normal distance of the $x - y$ plane from the trailing edge of the respective element in mm.

opposite corners and then slowly migrate towards the center. As we move from left to right across the second element, these structures fade although similar structures are created at the center. As we move further in the direction of fluid flow more of these folding structures develop on either side of the elements; the mean age distribution becomes more uniform. This indicates strong radial mixing. A large area within any cross section in the sixth element for turbulent flows has $a/\overline{\alpha_z} \approx 0$. This indicates that occurrence of fluid bypassing and short circuiting is more probable in case of turbulent flows compared to laminar flow for which $a/\overline{\alpha_z} \approx 1$.

The spatial distribution of mean age also reveals mixing in the region after the mixer. Figure 4.12 shows mean age distribution at different cross sections located after the trailing edge of the sixth element ($z/D = 10.63$). At $Re = 1$, the distortion of striations is minimal and the stagnation region created due to the trailing edge of the sixth element (Figure 4.1), represented by a thin tilted line of older aged fluid passing through the center, remains unchanged until the outlet. Mixing of the fluid after the end of the mixer will be minimal in viscosity-dominated flows. As inertia starts to dominate ($Re = 100$), we observe bending of striations: the tilted line which

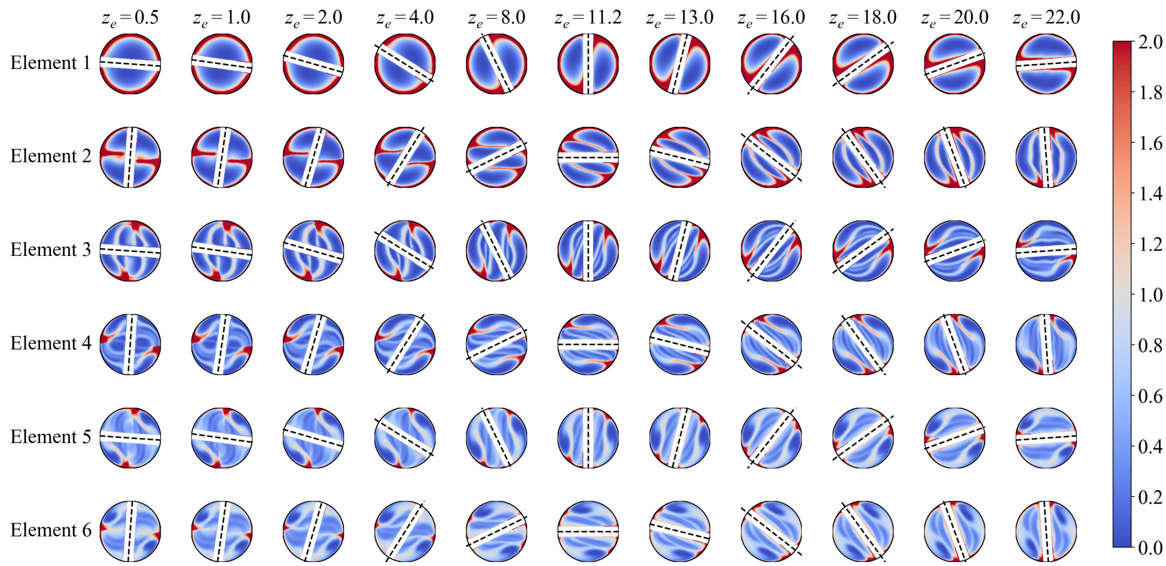

Figure 4.4: The evolution of mean age distribution for $Re = 10$

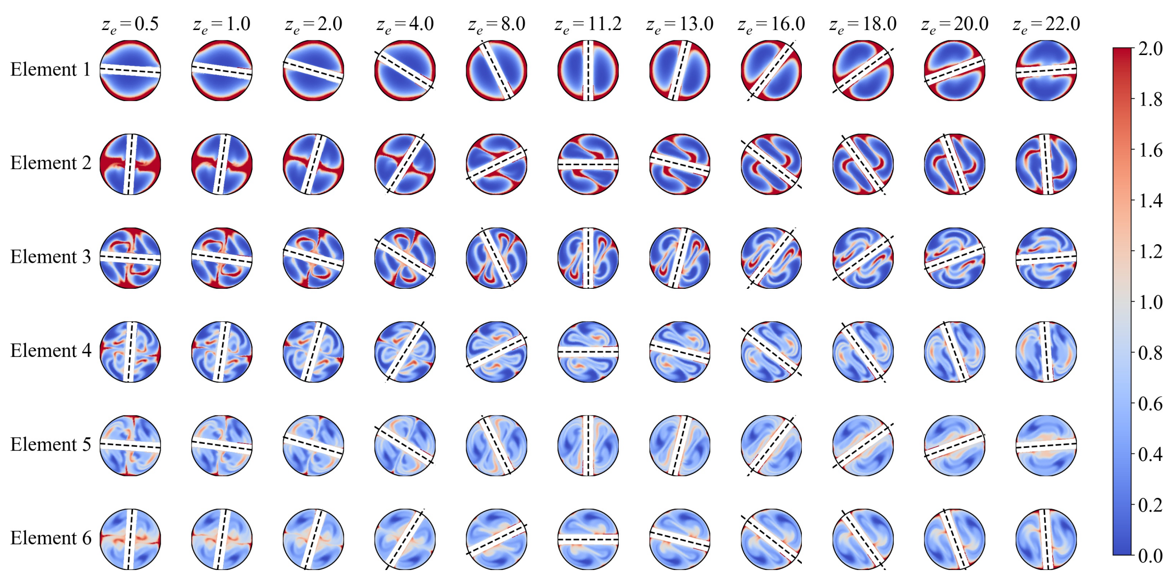

Figure 4.5: The evolution of mean age distribution for $Re = 100$

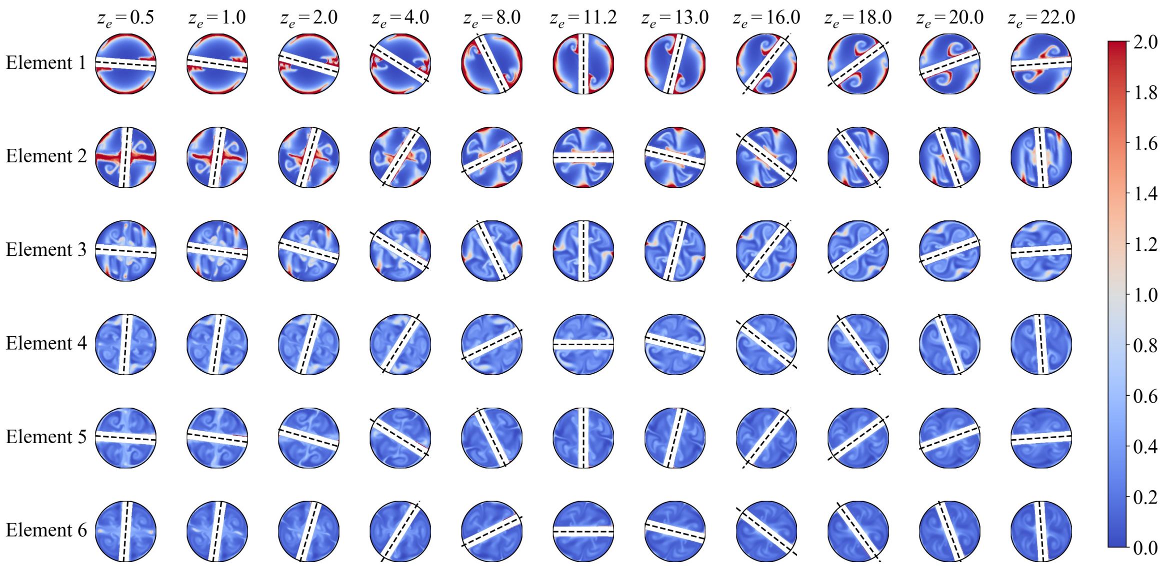

Figure 4.6: The evolution of mean age distribution for $Re = 1000$

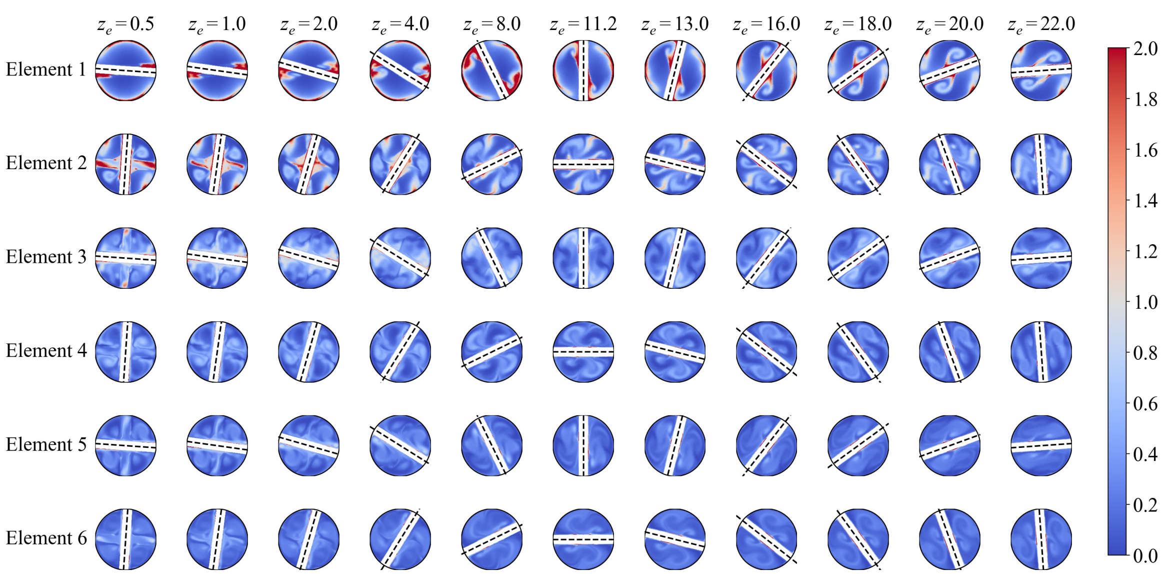

Figure 4.7: The evolution of mean age distribution for $Re = 5069$

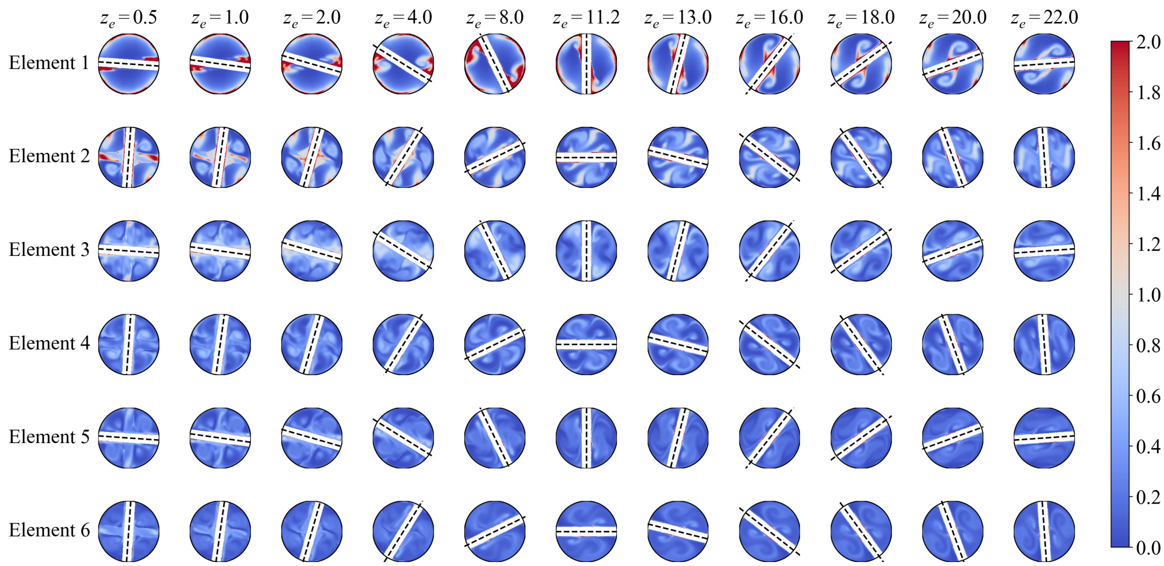

Figure 4.8: The evolution of mean age distribution for $Re = 6843$

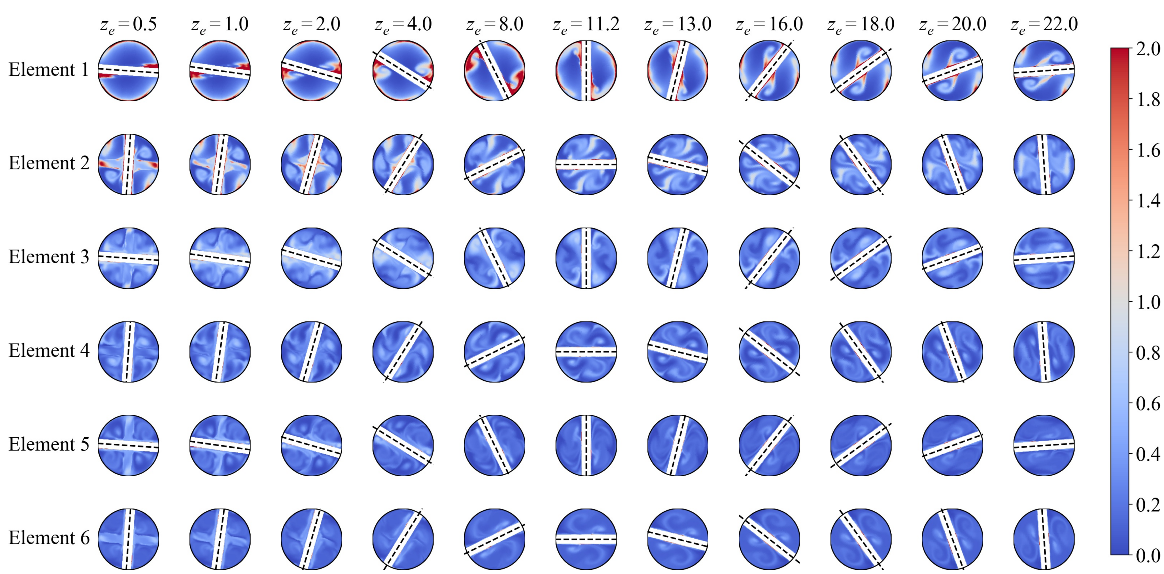

Figure 4.9: The evolution of mean age distribution for $Re = 9504$

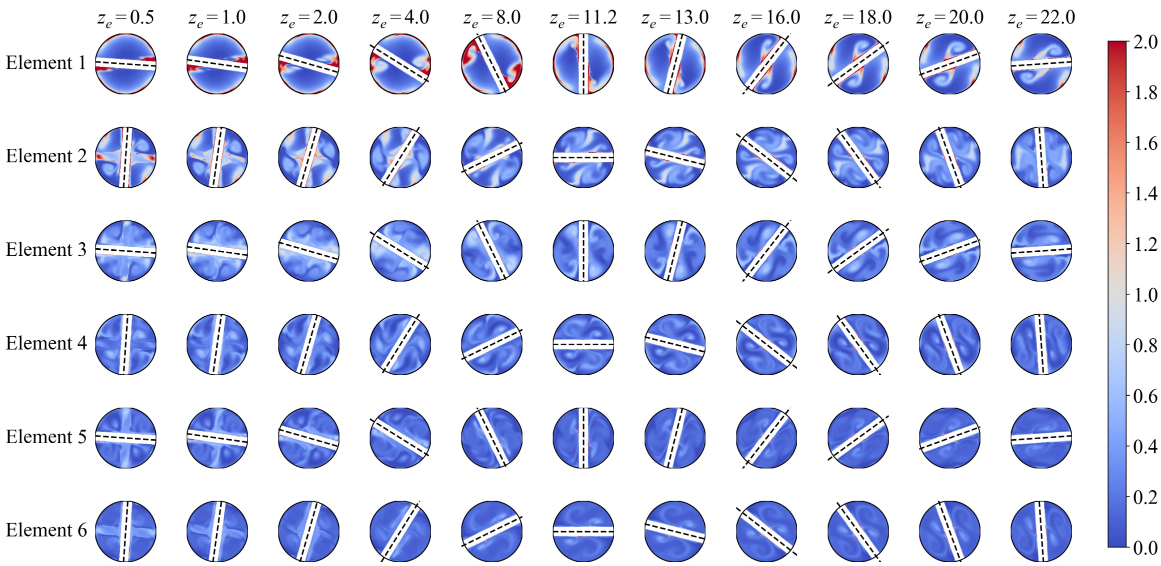

Figure 4.10: The evolution of mean age distribution for $Re = 10391$

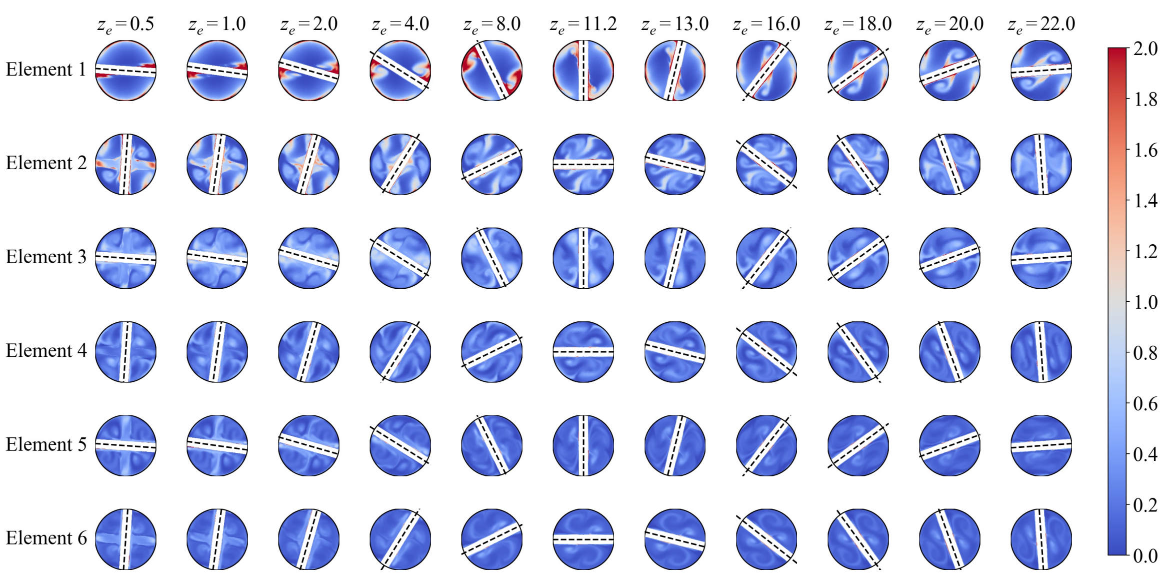

Figure 4.11: The evolution of mean age distribution for $Re = 12000$

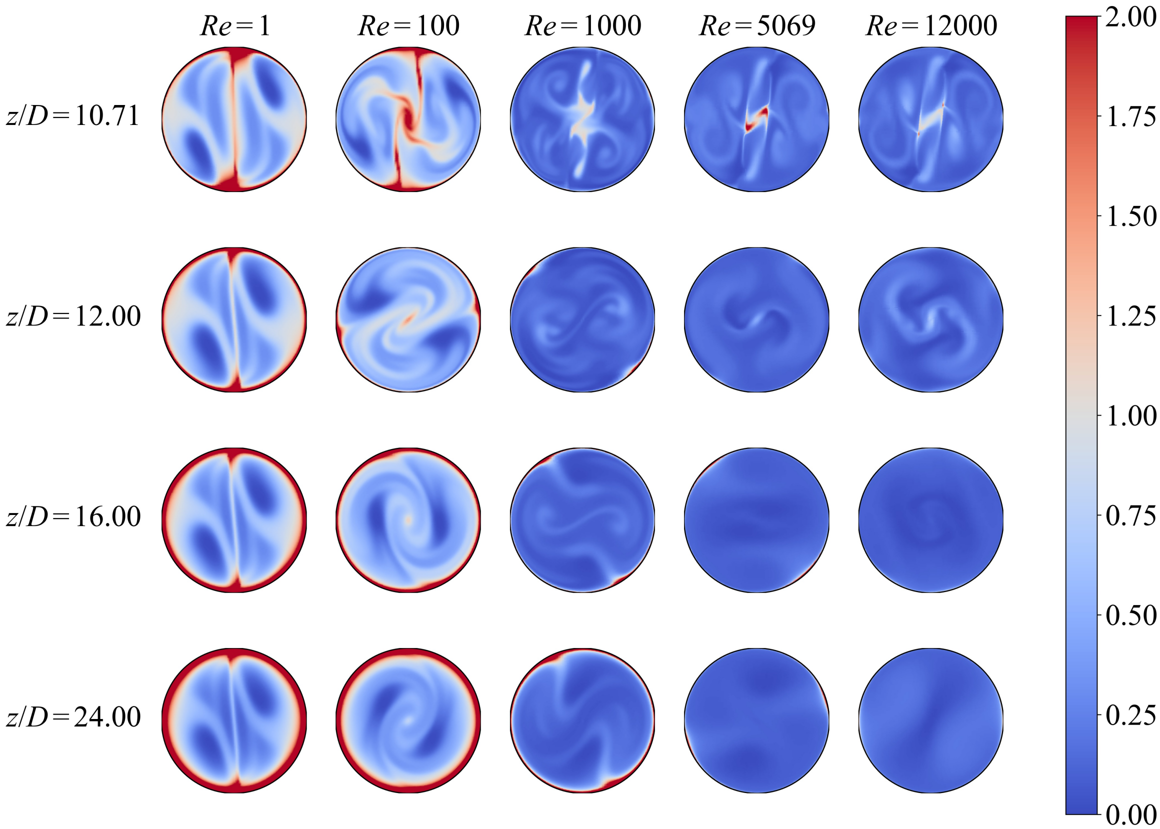

Figure 4.12: Cross sectional view of the mean age distribution on various $x - y$ planes after the trailing edge of sixth element. The Figure shows the effect of tangential velocity, U_{tan}, on to the distribution of mean age.

was unaffected for the case of $Re = 1$ is now distorted.

The stagnation region at the end of the sixth element can also be seen at the top row of Figure 4.12. At $Re = 100$ we observe a circular region of older aged fluid at the center. For the cases of turbulent flow, we see two segregated regions of older aged fluid at the center. The regions move apart as the Reynolds number of the flow increases. Unlike for the case of $Re = 1$, the mean age distribution becomes more uniform as we move from top to bottom. This gain in uniformity of the mean age distribution even after the mixer can be attributed to the rotational motion of the fluid.

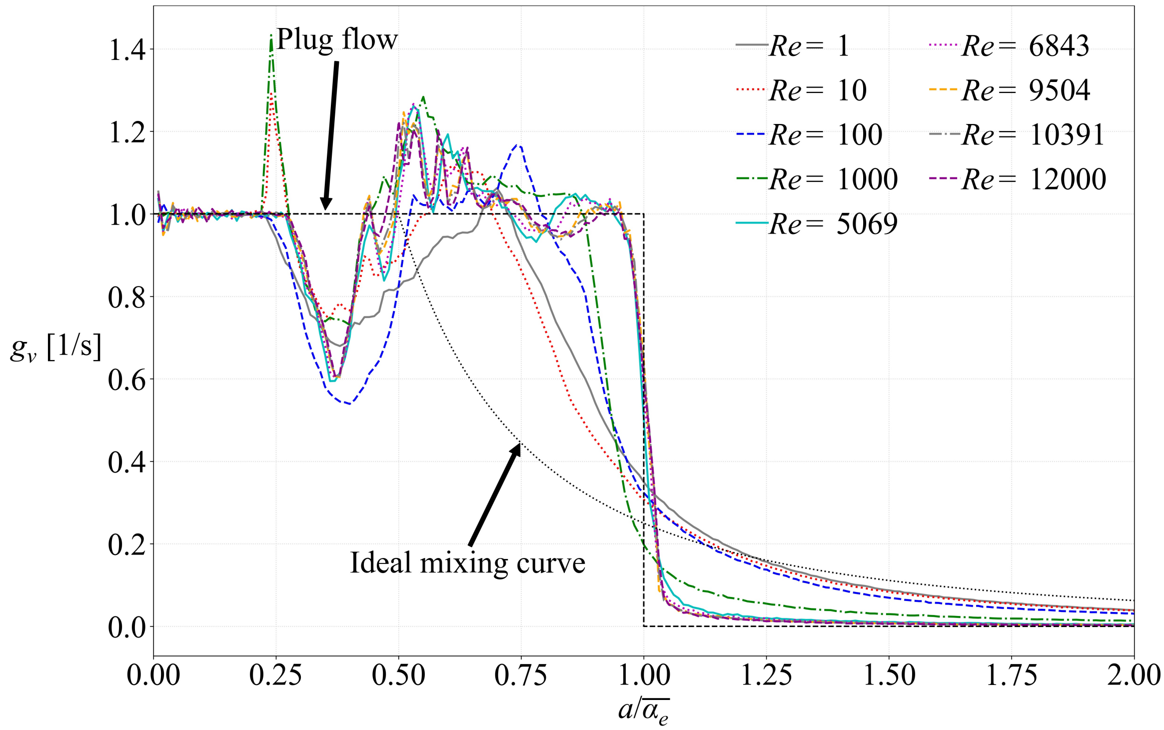

Figure 4.13: Mean age frequency distribution for flow corresponding to different Reynolds number. The deviation from ideal and pipe flow can be seen.

4.3 Mean Age Frequency Distribution

A frequency distribution can be obtained from the complete three dimensional mean age distribution obtained over the numerical grid. This spatial distribution can help characterize the spatial non uniformity in the mixing such as by-passing, re-circulation or short-circuiting of fluid [32].

4.3.1 Surface Averaged Mean Age Frequency Distributions

The effect of mixing elements on the mean age distribution can be observed by plotting the surface based frequency distribution of mean age, g_s, defined by Equation 2.24 at different cross sections of the mixer. Figure 4.14 shows g_s at different $(x - y)$ cross-sections at four of Reynolds numbers. The magnitude of the mean age is normalized by the average molecular age of the fluid, $\overline{\alpha_z}$, at the corresponding $(x - y)$ plane. The plug flow is shown by a black dashed vertical line, i.e $a/\alpha = 1$. For laminar flow

($Re = 1$), the distribution of mean age is represented by a straight horizontal line for the cross-sections near $z/D = 0$, indicating that the frequency of regions having magnitude of mean age $a/\overline{\alpha_z} < 1$ is approximately equivalent to that of regions having normalized mean age above unity. For turbulent flows, the zones of higher and lower mean age can be observed. The span of the distribution also gets narrower with an increase in the height of peaks as the Reynolds number of the flow is increased, indicating uniformity. Note that as the Reynolds number of the flow is increased the peaks tend to approach $a/\alpha = 1$. This indicates that the probability of mean age being equal to molecular age at any given point in the respective cross-section is higher for turbulent flows. It can also be stated that the flow has a tendency to approach plug flow for higher Reynolds number flow. Note that at $Re = 5069$, the peak is achieved at $z/D = 12$, and the frequency distribution of the mean age at this location is bi-modal. The peak on the left corresponds to a value of mean age below the average molecular age whereas the peak on the right indicates a value of mean age above the molecular age. The value of g_s on the right is higher than the one on the left. The region of cross section having age higher than molecular age could represent zones of stagnant or slow moving fluid.

At $Re = 12\ 000$, the maximum value of g_s is achieved at $z/D = 16$ which is relatively far from the end of the mixer. Irrespective of the Reynolds number of the flow the peak in the surface based frequency distribution of mean age is achieved after the sixth element. As the Reynolds number increases the axial location, z/D, corresponding to the maximum uniformity, moves further away from the trailing edge of the sixth element. The uniformity of mean age slowly wanes after the peak in uniformity has been achieved. The peaks start flattening and the mean age distribution becomes segregated again. This can be observed in Figure 4.14.

The analysis of frequency distribution of mean age revealed the closeness of flow to ideal flows at any given cross section of the flow. The distribution of mean age has the potential to quantify zones of lower and higher mean age and their variation as

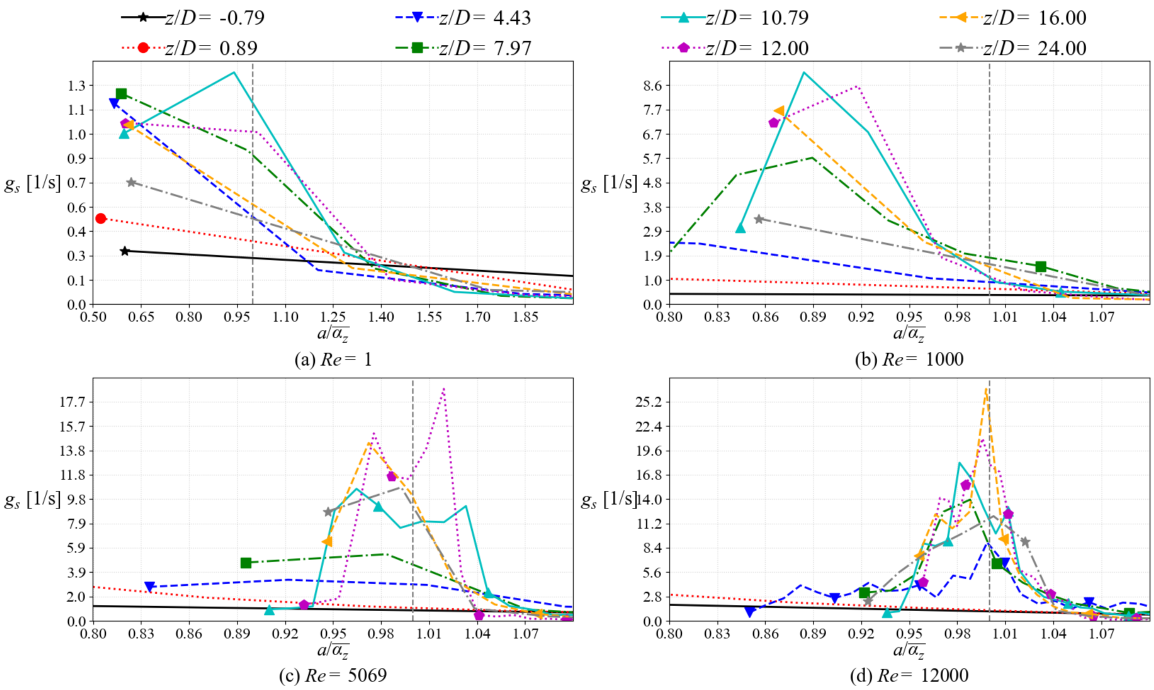

Figure 4.14: Surface averaged frequency distribution in different cross-sections ($x-y$ planes) across the Kenics mixer for different flow regimes.

the flow passes through the mixer.

4.4 Variance of Mean Age

The variance of mean age on any given cross section as defined by Liu [57] is given by Equation 2.31. The variances are often used to quantify the scalar mixing within a continuous flow vessel. Figure 4.15 shows the variance of mean age at different cross sections along the Kenics mixer. The difference in variance of age for the fully developed flow before the leading edge of the first element is noticeable. This difference in variance of age is the result of different velocity profiles corresponding to different Reynolds number flows. For the case of turbulent flows the reduction in variance of age is strongly correlated with increase in Reynolds number. For the case of laminar flows, however the variance of age corresponding to the $Re = 100$ is greater than the one observed for the case of $Re = 10$ and is almost equal to variance of age for the case of $Re = 1$. A similar observation is also made by Liu [57] for laminar flow across the Kenics micromixer. Liu [57] attributes this anomaly to the difference in the degree of inertia of the flow.

A reduction in variance of age is observed with the passage of each element irrespective of the Reynolds number of the flow. Although higher the Reynolds number higher the reduction in variance of age in the axial flow direction. Liu [57] makes a similar observation for laminar flows as well and in the present study we figured out that a similar trend is observed for turbulent flows.

The interesting part revealed by the present study is the increment in variance of age after a certain distance away from the Kenics mixer. For the flows in laminar and transition regime a steady increase in variance of age is observed. For the case of turbulent flow, a steady increment in variance of age is followed by a decrement. As the Reynolds number of the flow increases these fluctuations become smoother. The variance of age at the exit is approximately equal for the case of three largest Reynolds number flows in the study. This trend in variance of age is also in coherence with the behaviour of maximum value of g_s across the Kenics mixer, shown in Figure 4.16.

4.5 Machine Learning to Analyse Mixing via Mean Age

The above given visual analysis of mean age distribution provides a way to compare the mixing phenomenon within the static mixer, however, it does not provide a quantitative assessment. The mean age distribution across the $x - z$ plane (Figure 4.1) and the $x - y$ cross sections (Figure 4.3 to 4.11) show the variation in regions of low and high mean as the Reynolds number of the flow changes. However, these visual comparison fails to draw a line between the regions associated with low or high mean age, neither do they quantitatively predict the variation or mean of age distribution in these regions. The surface average frequency distributions somewhat shows how these regions change by demonstrating the type of distribution that overlays any given cross

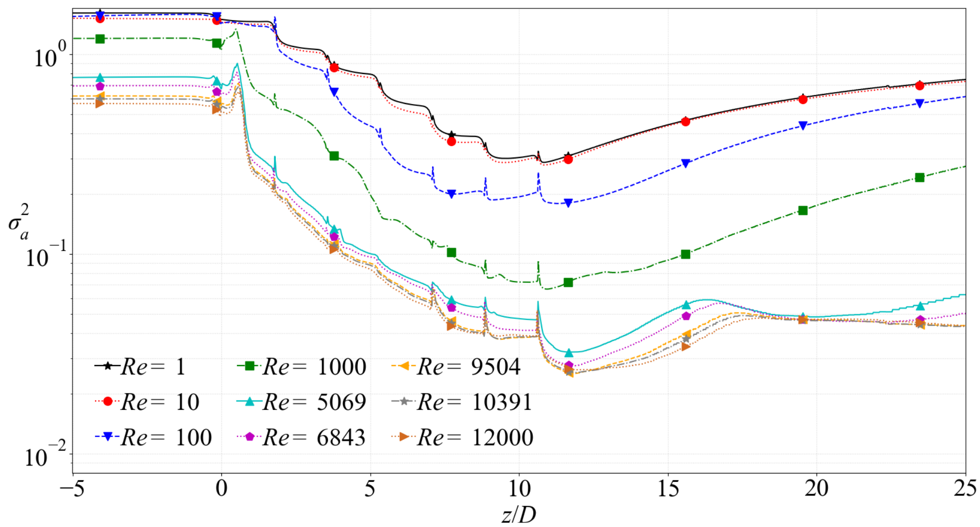

Figure 4.15: Variance of mean age on a cross section perpendicular to flow versus axial direction i.e. z.

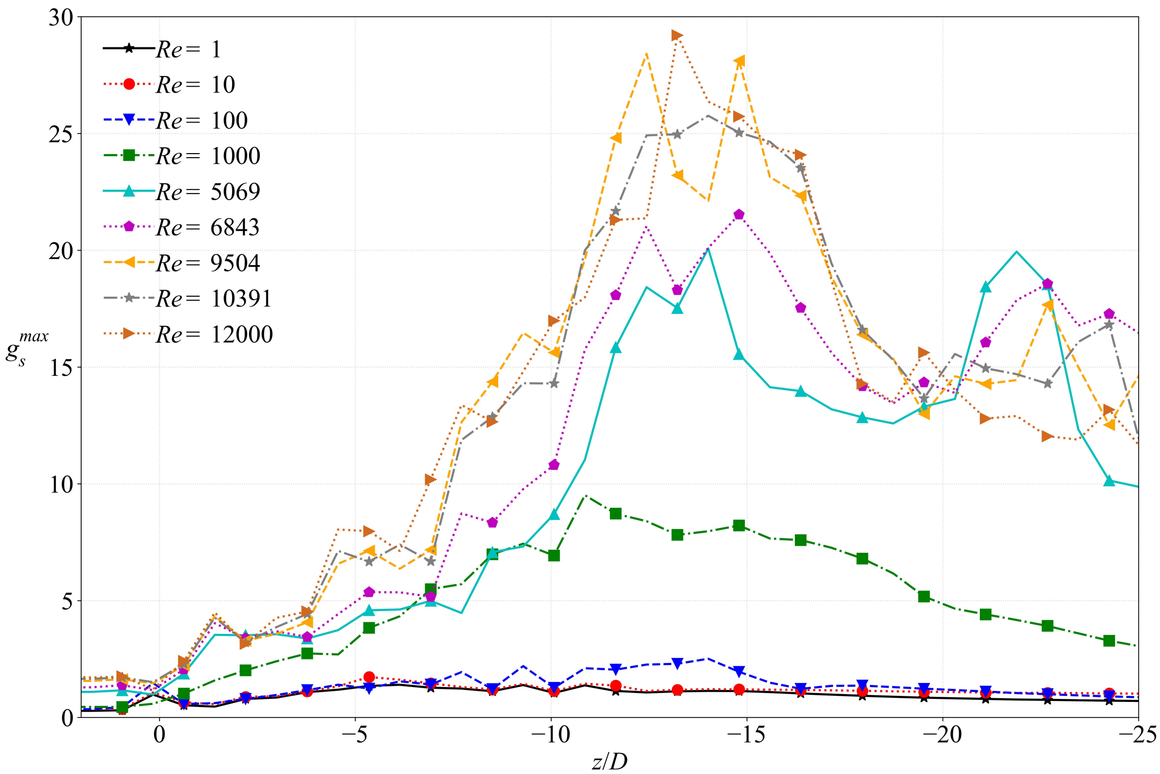

Figure 4.16: Peak value of g_s in the axial flow direction.

section. However they also fail to provide the quantitative parameters that define a distribution i.e. the moments of a distribution.

If an underlying distribution is Gaussian, then the moments of the distribution can be evaluated in a simplistic manner [66]. However, things become complicated when the underlying distribution is random and does not necessarily follow any standard distributions like Gaussian distributions. Looking at the surface average distribution and histograms in the above section we can safely establish that the distribution of mean age does not follow a Gaussian curve. In fact the mean age distribution for higher Reynolds number flows (i.e. above Reynolds of 1000) can be seen as a combination of many Gaussian curves with different mean and variance. Such a distribution can also be coined as a multi-modal distribution.

If we can identify the distributions that form these multi-modal distributions then we can evaluate mean and variance of mean age distribution specific to certain location on any given cross section. This information can help exactly identify the regions where adverse mixing conditions are being created and henceforth we can also deduce the reasons behind this adverse mixing and take measures to prevent it.

There are various ways to identify the distributions that could possibly constitute the multi-modal distributions [67]. A review onto such methods is out of the scope of this literature. However as it has been established by the previous literature that the distribution of the quantities (i.e disperse phase within the mixer) can generally be described by a normal distribution we assume that the current multi-modal distribution would also be composed from multiple Gaussian curves.

Taking the following assumption in to account we used the Gaussian Mixture Model (GMM) from the Python's Sci-Kit Learn [68] library. The implementation of the model by Sci-Kit Learn allows for the flexibility of automating the prediction of Gaussian curves and is therefore a part of Machine Learning models.

4.5.1 Histogram

Before we move forward to using machine learning to demarcate different Gaussian clusters of mean age distribution that constitute the multi-modal distribution, it is important that we observe the raw distribution with the help of histograms. This will help visualise the data and know whether there is a need for using GMM. Also the histograms will show us whether the the prior distribution is in coherence with the surface averaged mean age distribution presented in Section 4.3.1.

The stacked histograms (i.e. different histograms stacked on top of each other [69]) for the distribution of mean age on a cross section normal to the direction of the flow are shown in Figure 4.17, 4.18, 4.19 and 4.20. These histogram are normalised by the area the curve. In all the four figures the tallest distribution is observed for the Reynolds number of 12000. The height of peaks reduce as the Reynolds number of the flow reduces. This observation is in coherence with the fact that as the Reynolds number for the flow increases the mean age on any given cross section approaches the molecular age, α. It can also be noticed that distribution also approaches the molecular age as we move along the axial direction of the flow. These facts observed are in coherence with the ones deduced by analysing the surface averaged frequency distribution of mean age.

Figure 4.17 shows the distribution of mean age on section located mid-way along the first element. The distribution is linear for the Reynolds number flows in the laminar regions and becomes slightly peakier for the flow corresponding to the Reynolds of 12000. Figure 4.18 shows stacked histogram on a section located mid way along the third Kenics element. As observed earlier the distribution gets even more peaky however it still remains linear for the low Reynolds number flows in laminar region. The Figure 4.19 and 4.20 show the distribution of mean age on a cross section 2 mm and 15 mm away from the trailing edge of the sixth Kenics element respectively. As mentioned above the distribution of mean age get peakier as we move along in the direction of Kenics mixer. It must also be observed that the peak is highest for the flow corresponding to the Reynolds of 12000 and the height reduces as the Reynolds number of the flow reduces.

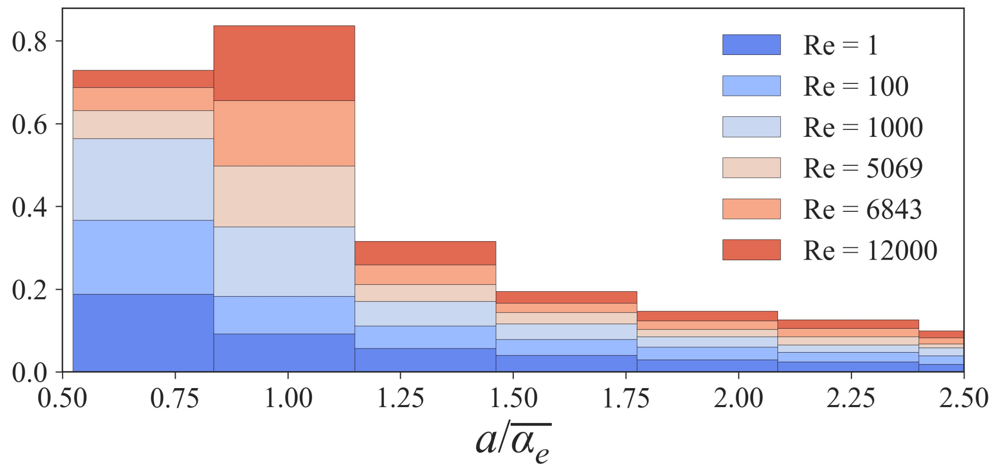

Figure 4.17: Stacked histogram depicting the frequency distribution of mean age for different Reynolds number flows on a cross section in $x - y$ plane at $z = 11.25$mm

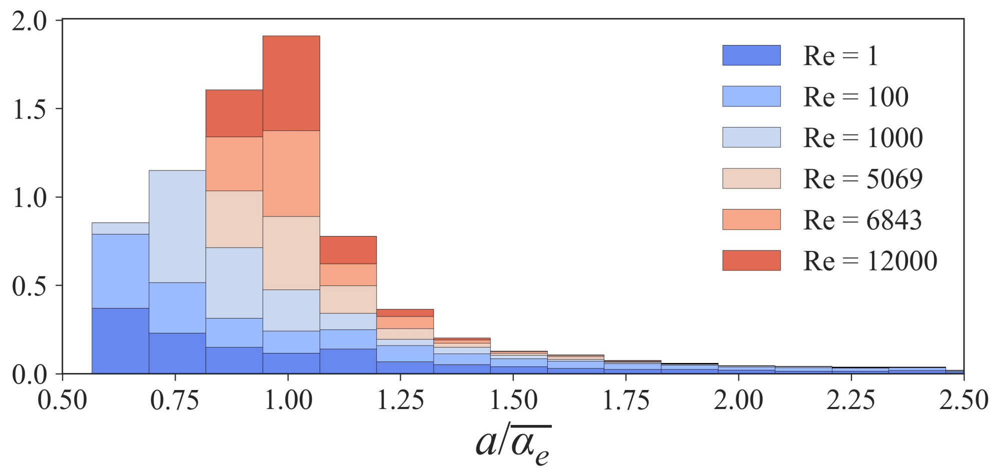

Figure 4.18: Stacked histogram depicting the frequency distribution of mean age for different Reynolds number flows on a cross section in $x - y$ plane at $z = 56.25$mm

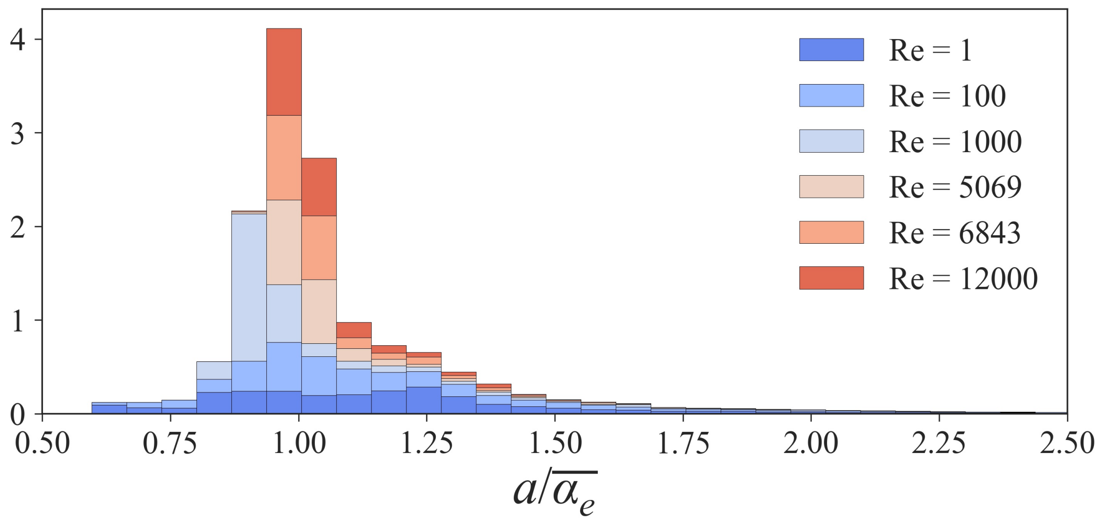

Figure 4.19: Stacked histogram depicting the frequency distribution of mean age for different Reynolds number flows on a cross section in $x-y$ plane at $z = 137$mm

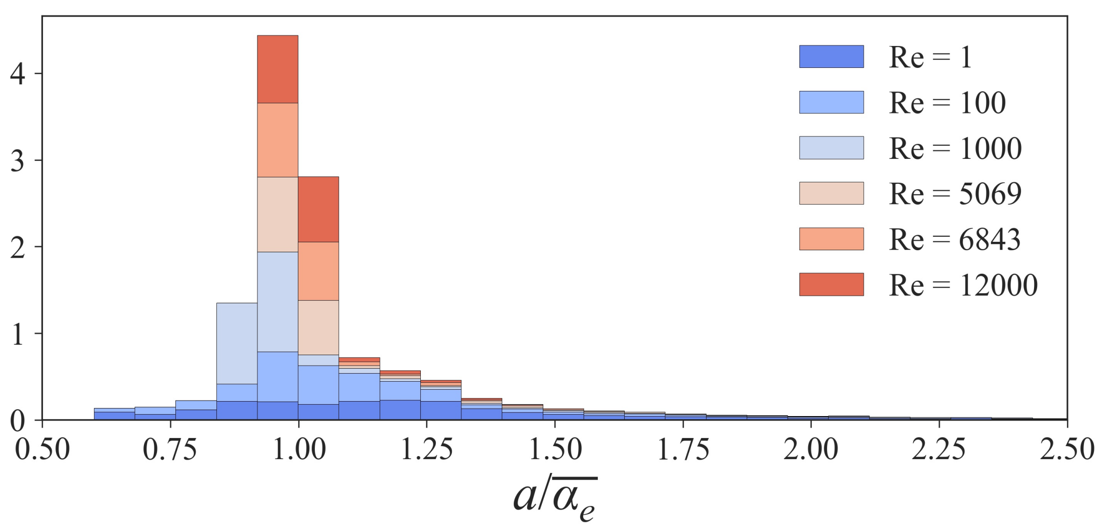

Figure 4.20: Stacked histogram depicting the frequency distribution of mean age for different Reynolds number flows on a cross section in $x-y$ plane at $z = 150$mm

4.5.2 Gaussian Mixture Model

A Gaussian mixture model (GMM) is a probabilistic model that assumes that the given distribution is a mixture of a finite number of Gaussian curves with unknown parameters [67]. A machine learning library Sci-Kit Learn [70] was used to implement GMM on various cross sections of the Kenics mixer. It was assumed prior to the application of GMM that the mean age distribution on any given cross section is a sum of 10 different Gaussian curves.

Figure 4.21 shows the application of GMM to fit the mean age distribution obtained on four different cross sections across the Kenics mixer for flow corresponding to the $Re = 1$. The Figure 4.21a and Figure 4.21b corresponds to mean age distribution mid-way along the first Kenics element and the third Kenics element, respectively. The bottom two figures, Figure 4.21c and Figure 4.21d correspond to the mean age distribution on a cross section 2 mm and 15 mm away from the trailing edge of the sixth element. The contour plot of velocity and mean age are also shown on the right hand side of each figure. The contour plot of velocity magnitude is normalised by the inlet velocity, U_{in}. The contour plot of mean age shows the regions of a cross section corresponding to the different Gaussian curves that were obtained using GMM to fit the mean age distribution. The region on the cross section corresponding to the Gaussian curve marked by dashed blue line is represented by the lowest level of the mean age color-bar, the curve marked by dashed orange color is represented by the second level of the color bar and the green dashed Gaussian curve represents the third level of the color bar for the mean age distribution. The topmost level of color-bar is reserved for the regions occupied by other seven Gaussian curves. All the Gaussian curves and the histogram (the light grey region) are normalised by area under the curve to obtain a probability distribution. Similar Figures for the mean age distribution obtained via numerical simulations for the flow corresponding to the Reynolds of 10, 100, 1000, 5069, 6843, 9504, 10391 and 12000 are shown in

Figure 4.22, 4.23, 4.24, 4.25, 4.26, 4.27, 4.28 and 4.29, respectively.

One of the most interesting observation that can be made from these figures is that how high velocity regions are associated with younger aged fluid. The figures also show that a larger part of older aged fluid which forms the tail of the distribution (shown by the green dashed curve for the case of laminar flows) is attached closely to the walls. This observation was also made visually by looking at the evolution of mean age in Figure 4.3 for the flow corresponding to the Reynolds of 1. However, with the help of GMM we can quantify the observation. The Gaussian curves pertaining to the older aged distribution (green dashed curve) has a large standard deviation along with a large mean (shown in the top right corner of Figure 4.21). The striations observed in Figure 4.3 can also be seen in Figure 4.21b. However with the help of GMM now we can quantify this fact. The average mean age of fluid within the striations is around $0.674\overline{\alpha_e}$, whereas fluid surrounding the striations have a mean age of $1.058\overline{\alpha_e}$. The ratio between the average mean age in the two regions is approximately 1.57. For the case of $Re = 10$ this ratio between the same is 1.59 and for the flow corresponding to $Re = 100$ it reduces to 1.53 and it further reduces to 1.23 for the transitional flow ($Re = 1000$). This observation was visually recorded by noticing disappearance of striations as the flow becomes chaotic. As the Reynolds number of the turbulent flow increases the ratio between the mean of Gaussian curves approaches unity.

The disappearance of striations and the decrement in the ratio of the means of the Gaussian curves is a direct causation of higher intermingling of particles due to chaotic turbulence which results in an almost equal dissipation of kinetic energy across the fluid domain which in turn forces the fluid volumes to have approximately equal mean age irrespective of there location. It can also be assumed that the radial mixing in case of turbulent flows will be higher compared to the laminar flows.

For the case of turbulent flows, the distribution of mean of age can longer be represented by three Gaussian curves as can be seen in the Figure 4.25b, 4.26b, 4.27b, 4.28b and 4.29b. The shape of regions occupied by the mean age corresponding to

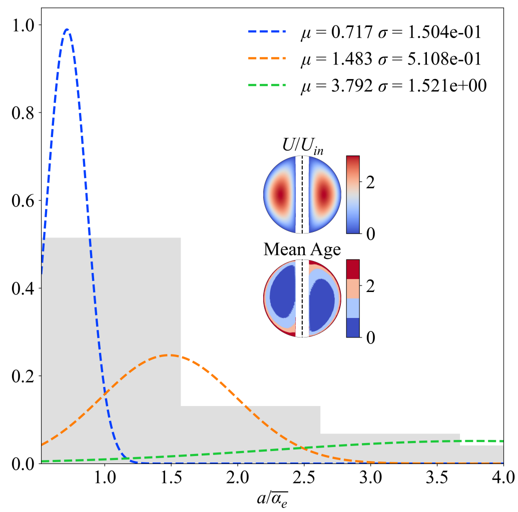

(a) $z = 0.89D$

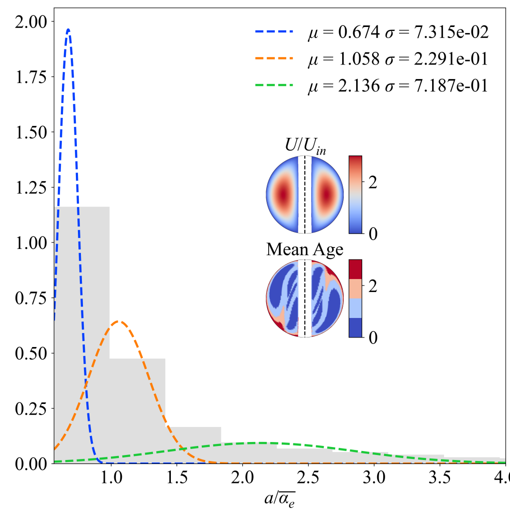

(b) $z = 4.43D$

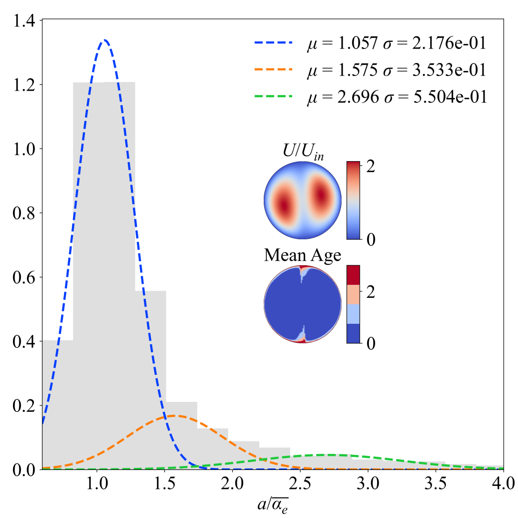

(c) $z = 10.79D$

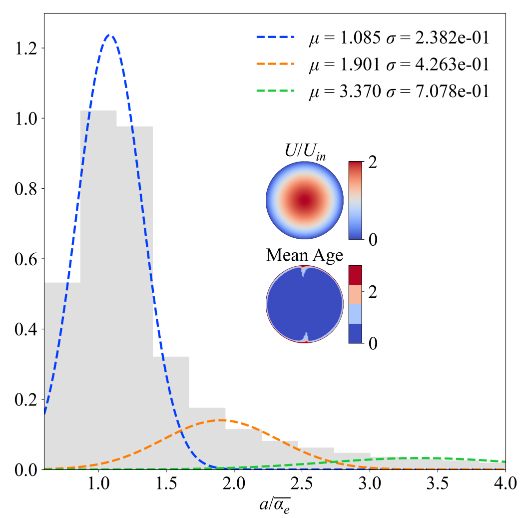

(d) $z = 11.81D$

Figure 4.21: The GMM model is used to identify the distribution of mean age as a sum of different Gaussian curves.The dominant blue curve alone is enough to represent the distribution of mean age on any given cross section for the creeping flow ($Re = 1$).

these Gaussian curves is also different from what was observed for the case of laminar flows. These changes in shapes can also be noticed from the evolution of mean age shown in Figure 4.7, 4.8, 4.9, 4.10 and 4.11. However with the help of GMM we were able to reveal the average mean age and standard deviation of fluid volumes that comprise these different shapes.

Rahmani *et al.* [23] discovered that for the case of turbulent flows small islands of

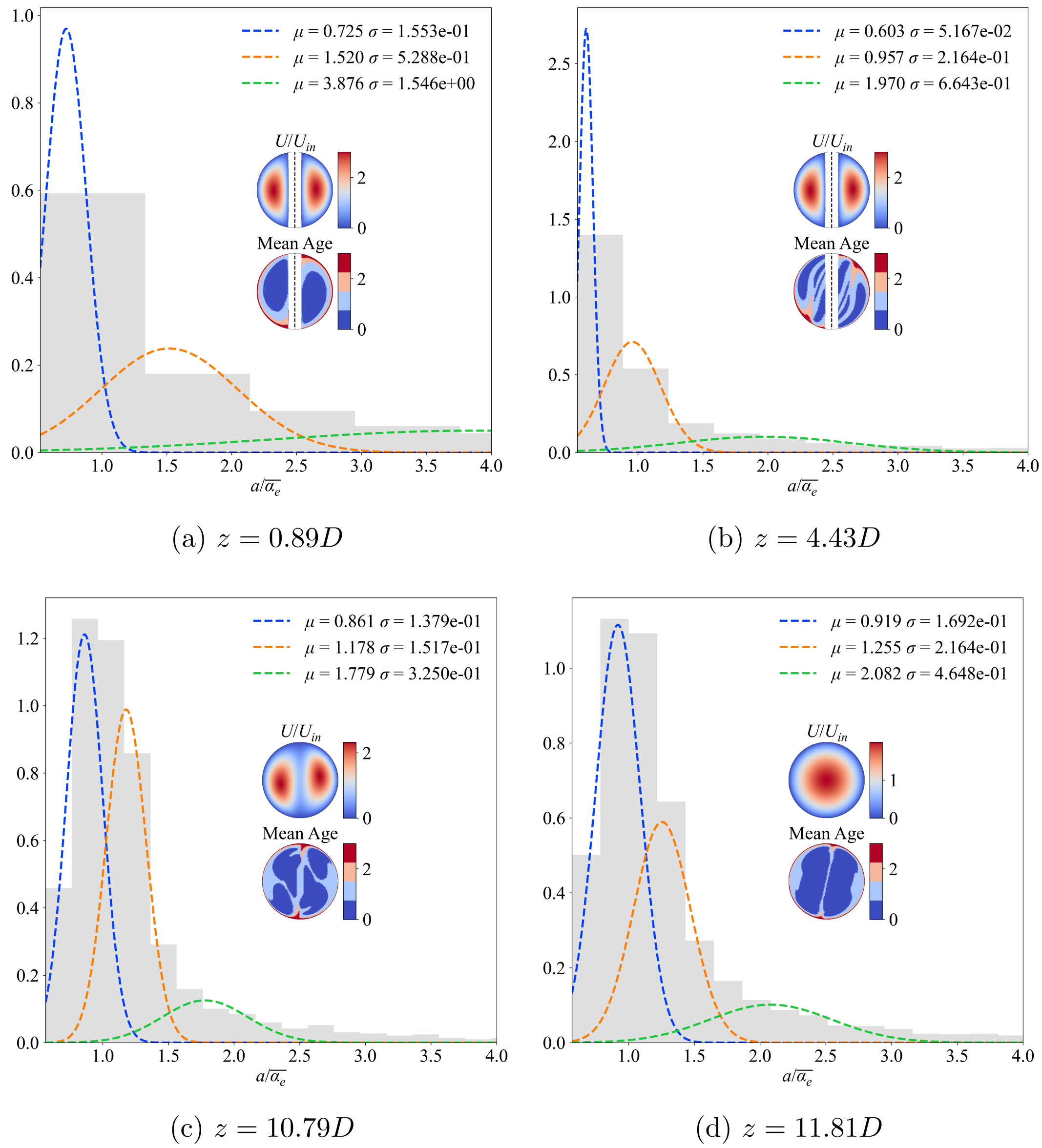

Figure 4.22: The GMM model is used to identify the distribution of mean age as a sum of different Gaussian curves.The dominant blue curve alone is enough to represent the distribution of mean age on any given cross section for the laminar flow ($Re = 10$).

particles were observed. A similar observation can be made for turbulent flows by looking at the contour plots of mean age distributions in the Figures 4.25b. A similar conclusion was also made by looking at the vector plots of velocity in Figure 3.11. However with the help of GMM now we can observe the mean and standard deviations of mean age of fluid volumes in these regions.

The GMM was also used to fit Gaussian curves onto the distribution of mean

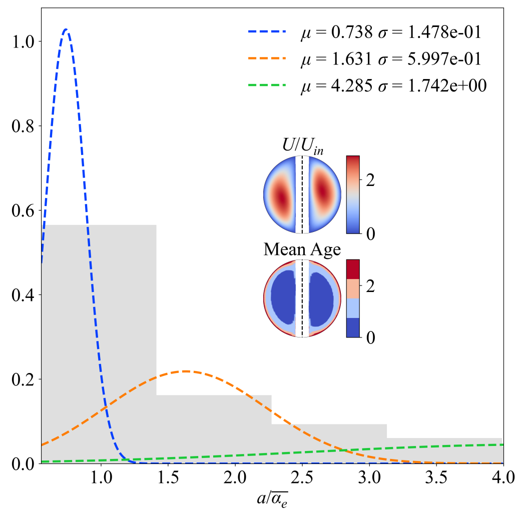

(a) $z = 0.89D$

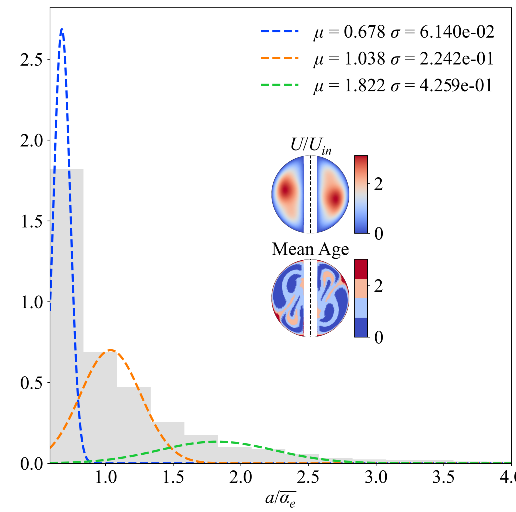

(b) $z = 4.43D$

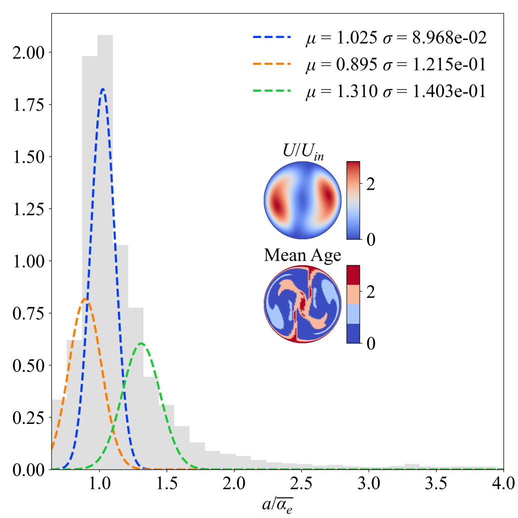

(c) $z = 10.79D$

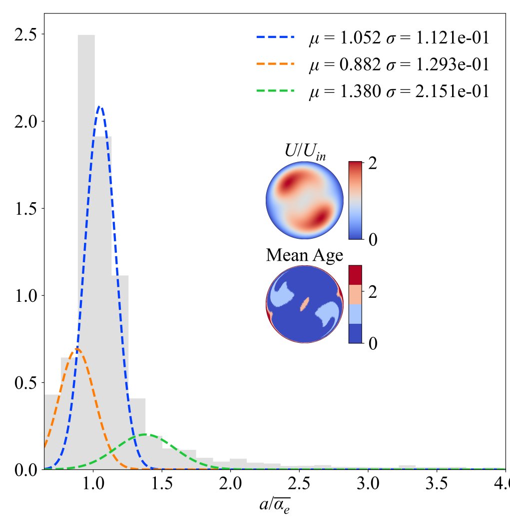

(d) $z = 11.81D$

Figure 4.23: The GMM model is used to identify the distribution of mean age as a sum of different Gaussian curves.The dominant blue curve alone is enough to represent the distribution of mean age on any given cross section for the laminar flow ($Re = 100$).

age observed after the sixth element of Kenics mixer. The bottom two curves in Figures 4.21 to 4.29, reveal how the rotational movement imparted to the fluid due to helical surface of the Kenics mixer affects the mean age distribution. For the case of creeping flow the region at the center is occupied by the younger aged fluid represented by the blue curve whose mean approaches close to unity. As the Reynolds number of the flow is increased to 10 (Figure 4.22). The region represented by the

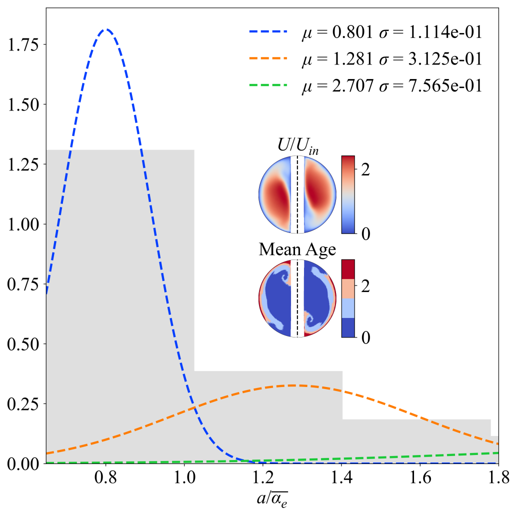

(a) $z = 0.89D$

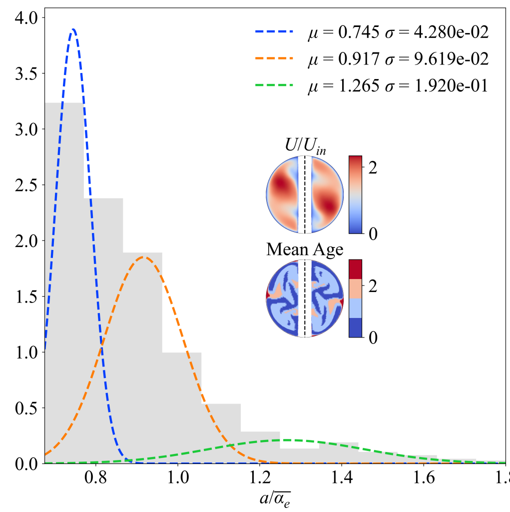

(b) $z = 4.43D$

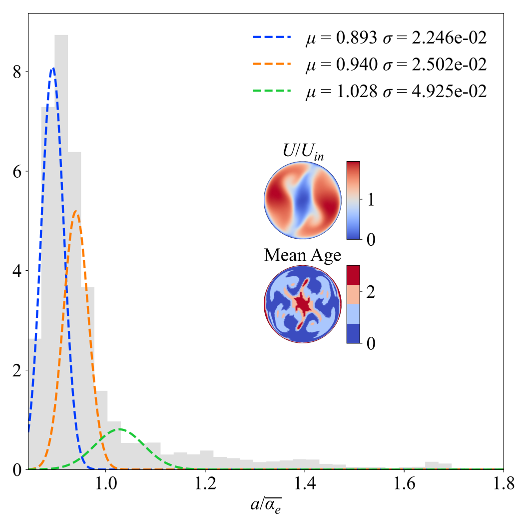

(c) $z = 10.79D$

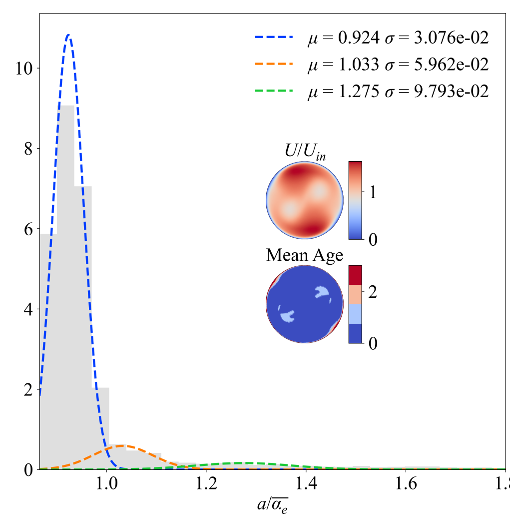

(d) $z = 11.81D$

Figure 4.24: The GMM model is used to identify the distribution of mean age as a sum of different Gaussian curves.The dominant blue curve alone is enough to represent the distribution of mean age on any given cross section for the transitional flow regime ($Re = 1000$).

blue curve dissociates into four different regions surrounded by a slightly older fluid (Figure 4.22c). The regions combine as we move further in the axial direction leaving out only two separate islands of older fluid with a thin strip of slightly older fluid between the two (Figure 4.22d). For the case of Reynolds number of 100 we observe that unlike low Re flows the region at the center is occupied by subsequently older

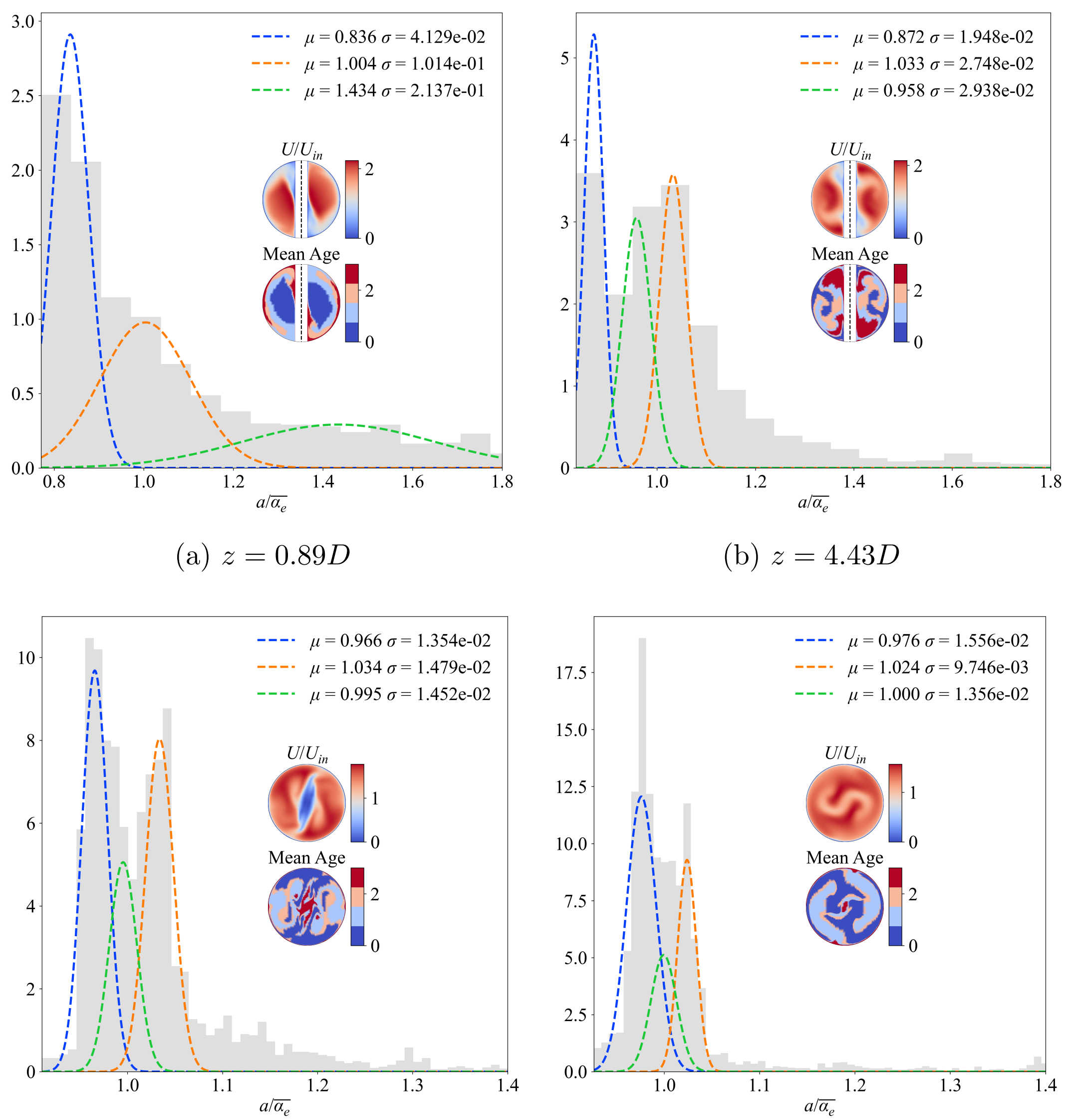

(a) $z = 0.89D$

(b) $z = 4.43D$

(c) $z = 10.79D$

(d) $z = 11.81D$

Figure 4.25: The GMM model is used to identify the distribution of mean age as a sum of different Gaussian curves.The dominant blue curve alone is not enough to represent the distribution of mean age on any given cross section for the turbulent flow regime ($Re = 5069$).

fluid (red region in contour plot of mean age in Figure 4.23c). This stark change in the distribution of mean age for high Reynolds number flows can be attributed to the presence of low velocity region entailing the end of the 2 mm thick Kenics element. The region of older fluid fades as we move along in the axial direction (Figure 4.23d) as the tangential motion of fluid imparted to it due to helical shape of the Kenics

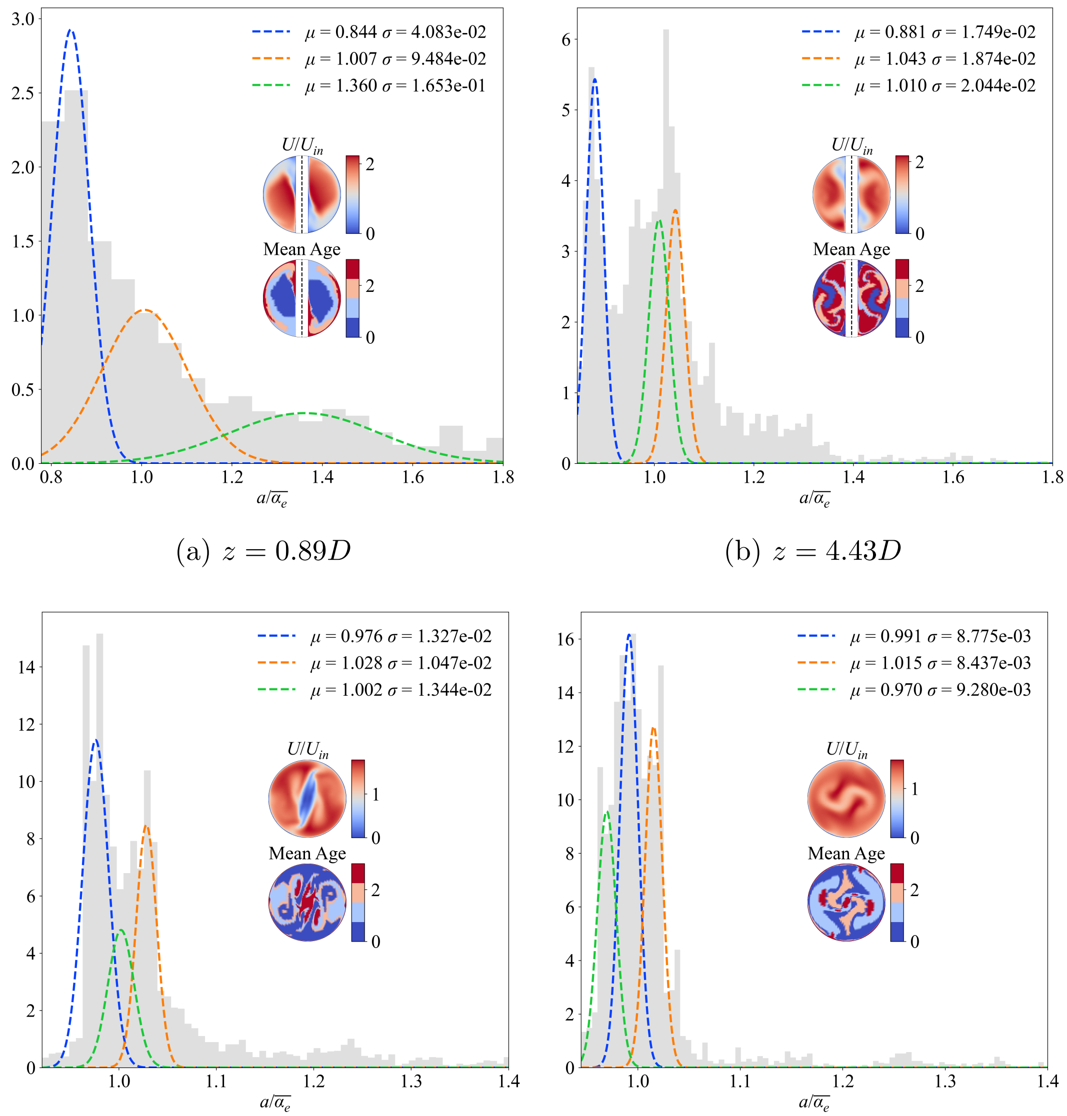

(a) $z = 0.89D$

(b) $z = 4.43D$

(c) $z = 10.79D$

(d) $z = 11.81D$

Figure 4.26: The GMM model is used to identify the distribution of mean age as a sum of different Gaussian curves.The dominant blue curve alone is not enough to represent the distribution of mean age on any given cross section for the transitional flow regime ($Re = 6843$).

element will force the radial intermingling of particles hence forcing them to achieve similar velocity and henceforth similar mean age.

This region of older aged fluid entailing the sixth Kenics element is observed for all the turbulent flow cases simulated (Figures 4.25 to 4.29). It is also interesting to note that the region of low velocity coincides with the region of older aged fluid

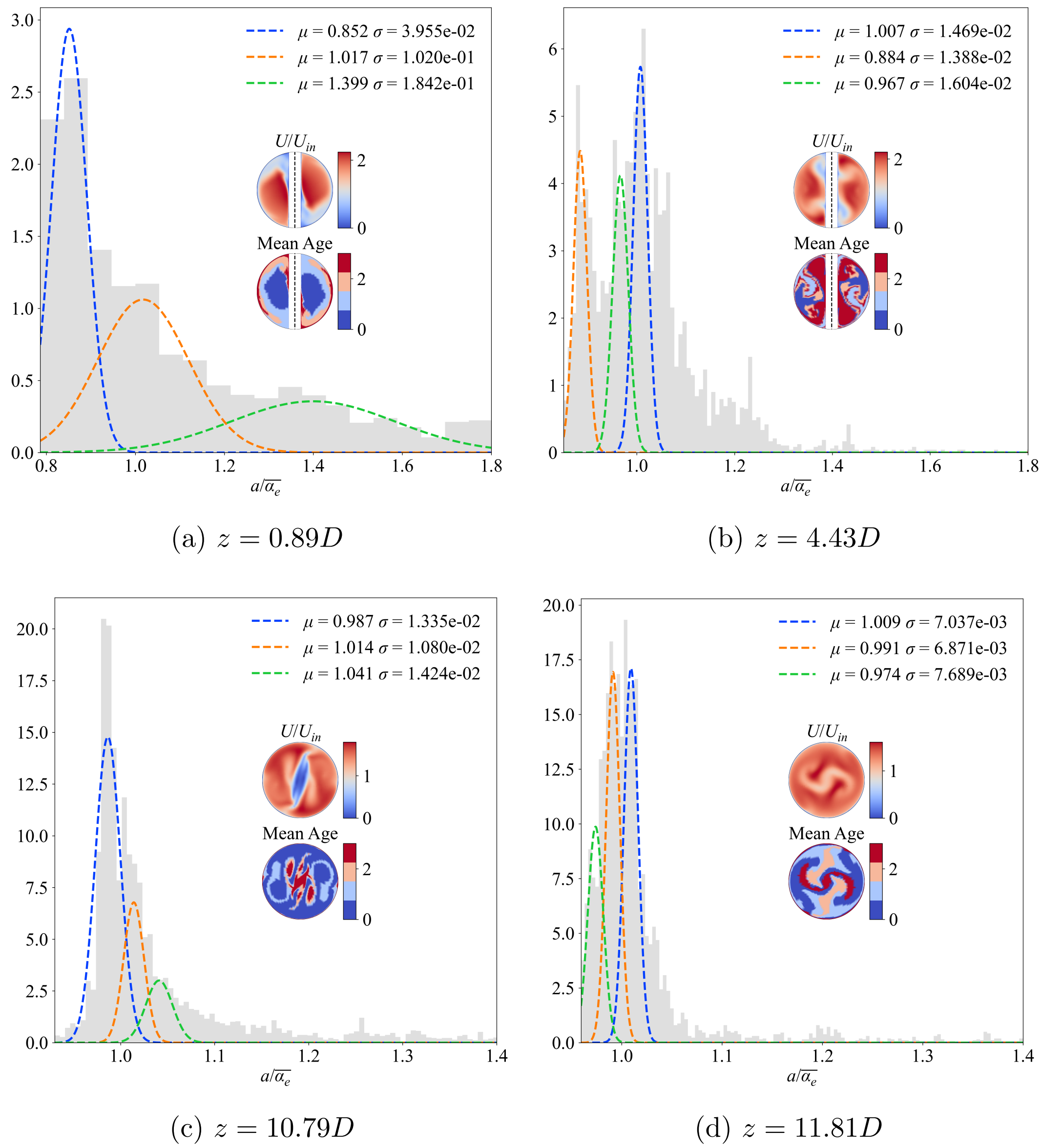

Figure 4.27: The GMM model is used to identify the distribution of mean age as a sum of different Gaussian curves.The dominant blue curve alone is not enough to represent the distribution of mean age on any given cross section for the transitional flow regime ($Re = 9504$).

observed at the center. As we move further in axial direction the region occupied by older aged fluid disappears.

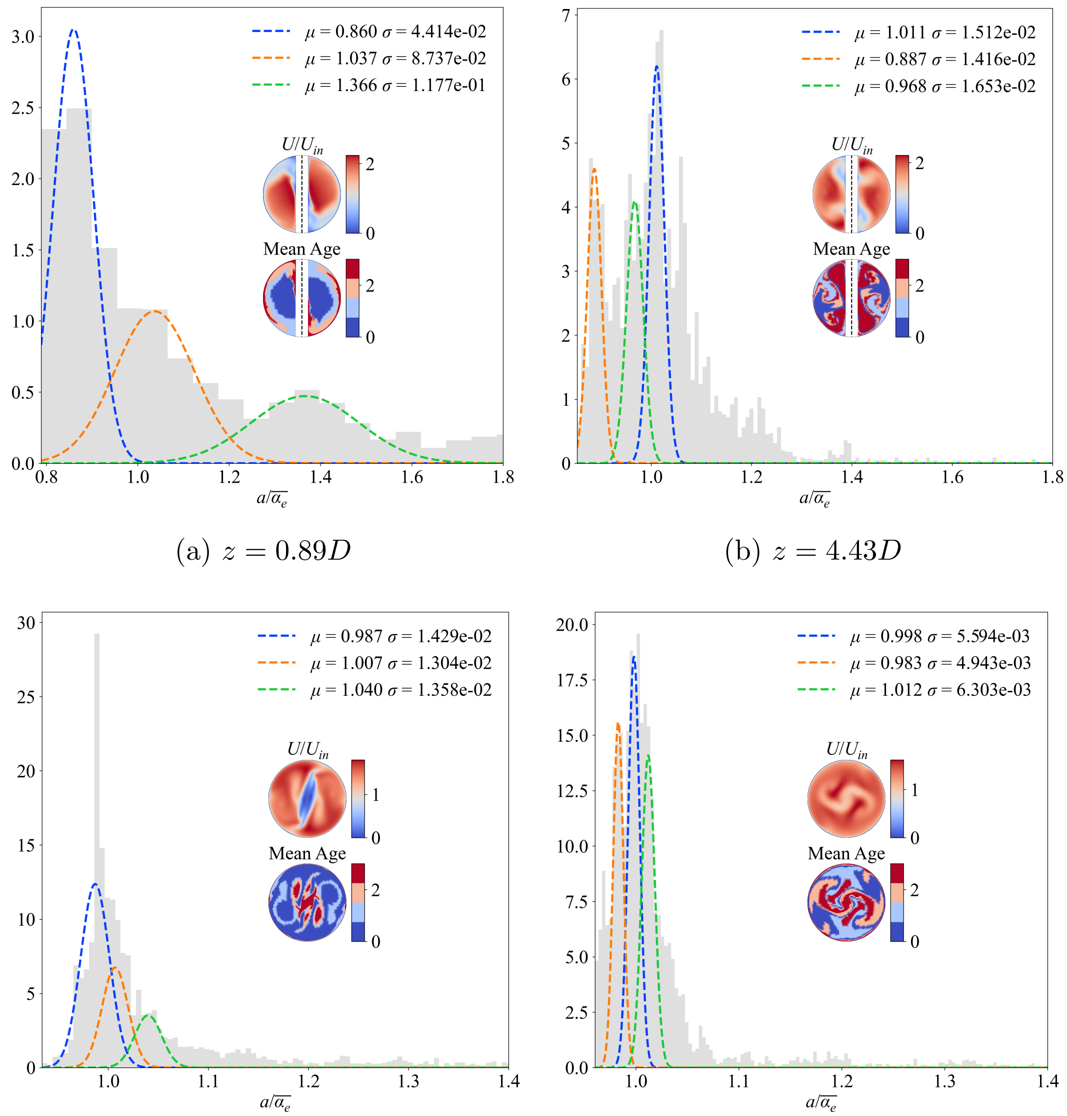

(a) $z = 0.89D$

(b) $z = 4.43D$

(c) $z = 10.79D$

(d) $z = 11.81D$

Figure 4.28: The GMM model is used to identify the distribution of mean age as a sum of different Gaussian curves.The dominant blue curve alone is not enough to represent the distribution of mean age on any given cross section for the transitional flow regime ($Re = 10391$).

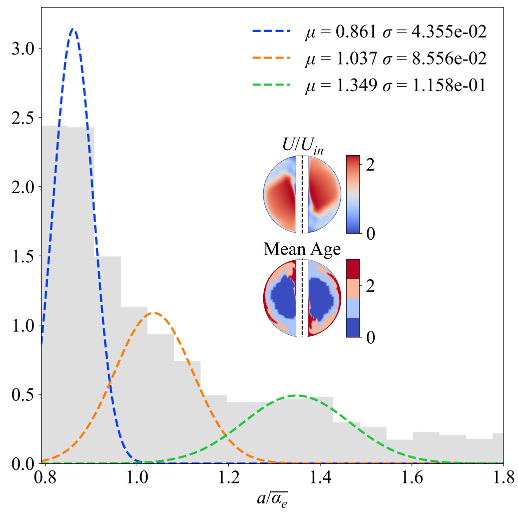

(a) $z = 0.89D$

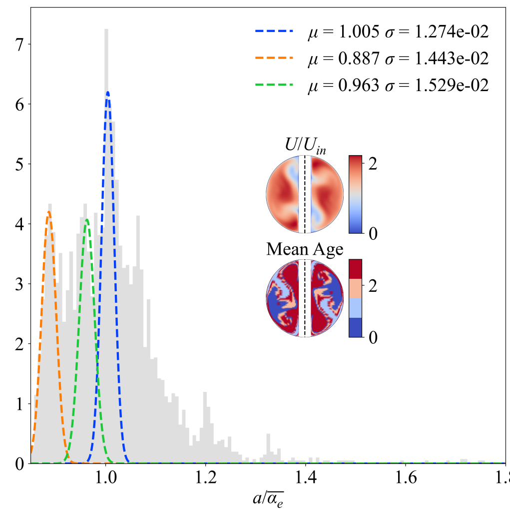

(b) $z = 4.43D$

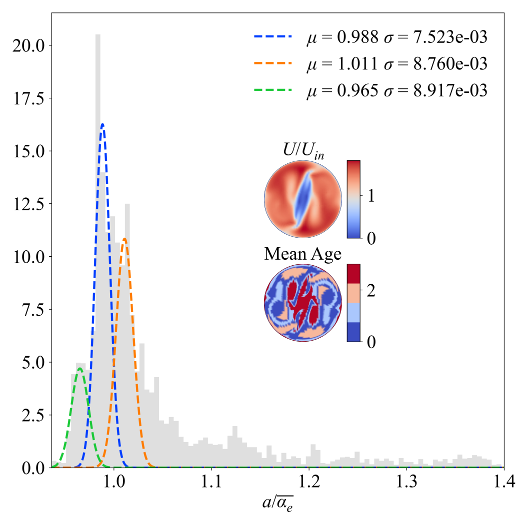

(c) $z = 10.79D$

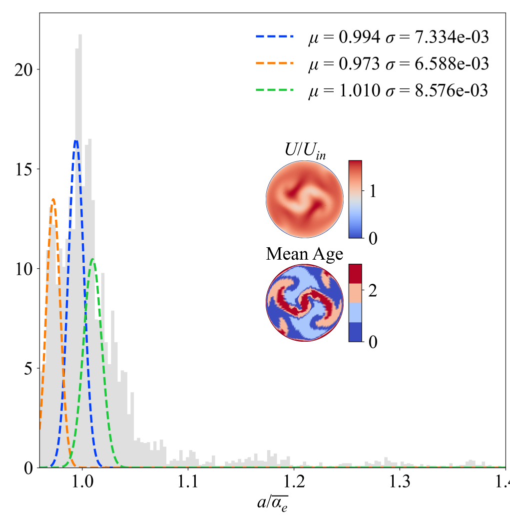

(d) $z = 11.81D$

Figure 4.29: The GMM model is used to identify the distribution of mean age as a sum of different Gaussian curves.The dominant blue curve alone is not enough to represent the distribution of mean age on any given cross section for the transitional flow regime ($Re = 12000$).

4.6 Summary

In this chapter we have shown how mean age distribution across the Kenics mixer can be qualitatively and quantitatively visualised to assess mixing within the Kenics mixer. The frequency distribution of mean age was evaluated across the volume of mixer and on various cross sections to assess adverse mixing within the Kenics mixer. The discovery of bi-modal surface averaged distribution of mean age on certain cross sections for the case of turbulent flows paved way for a more deeper quantitative analysis. For doing so, we resorted to machine learning and used the Gaussian mixture models (GMM) to identify the various Gaussian curves that would constitute a multi-modal distribution of mean age. An elegant use of the state of the art Machine learning models along with innovative visualisations to study the mean age distribution through the Kenics mixer for various flow regimes is presented.

Chapter 5

Conclusion

In this study, CFD was used to perform simulations of steady, incompressible and isothermal flow through a six element Kenics mixer using a commercial software, STAR-CCM+, on four different structured grids generated using Ansys ICEM. The flow was simulated in laminar, turbulent and transitional flow regimes over four different grids.

Three different RANS models: Realizable $k-\varepsilon$, EB $k-\varepsilon$ and Reynolds stress model were used to simulate turbulence. The impact of different turbulent models and the spatial grid on turbulent flow field predictions have also been identified. It was observed that the Realizable $k-\varepsilon$ predicts a higher magnitude of volume averaged turbulent kinetic energy, $\overline{\varepsilon}$ and the Reynolds stress model predicts a larger magnitude of pressure drop across the mixer when compared to other turbulent models. The Reynolds stress model model performed better on the grid D when compared to other turbulent models. When compared to existing literature the Reynolds stress model predicted the pressure drop and turbulence parameters across the mixer with higher accuracy.

The velocity and pressure field were evaluated on a range of Reynolds number flows in the laminar and turbulent regime using the Reynolds stress model. The pressure drop across the Kenics mixer in the laminar and turbulent flow regimes was compared to the existing correlations. For laminar flow, the maximum deviation from the experimental values was less than 9%. For the case of turbulent flows, a larger deviation from the experimental values was observed. The velocity fields at different Reynolds numbers was evaluated and analysed to assess the effects of convection on the mixing capability of the mixer in laminar and turbulent regime.

The spatial distributions of mean age reveal the generation, stretching, splitting and recombination of the lamellar structures. The phenomena vary for laminar and turbulent flows. For the case of creeping flow, lamellar structures are preserved due to the domination of viscous forces over inertial forces. The systematic folding and stretching of these structures is revealed as the flow velocity increases. Geometry of the mixing inserts plays a major role in defining the way in which striations are distorted. The clockwise and counterclockwise twist in the Kenics mixer influences the direction of folding of lamellar structures. As the flow becomes turbulent the striations disappear.

The spatial distribution of mean age also reveal the presence of dead zones within the mixer. The mean age distribution provides location of regions with older aged fluid, which can be associated with dead zones. The location of dead zones coincide with the stagnation zones revealed by the contour plots of velocity magnitude. The mean age distribution provides additional information on the nature of these stagnation zones which can be helpful in revealing whether the mixing in these regions is high or low.

The spatial distribution of mean age after the mixer was analysed to assess mixing in the pipe after the mixer. The driving force for mixing in that region is the rotational motion of the fluid imparted to it by the helical shape of the Kenics element. For the case of creeping flow, the mean age distribution after the mixer remains unchanged, whereas for the convection dominated flows the distribution of mean age varies vigorously in the axial direction.

To quantify visual observations, the surface based frequency distribution of mean age was evaluated at various cross sections at different Reynolds numbers. This quantity can be used to estimate the deviation of the flow though the mixer from the ideal plug flow. It also reveals the nature of the distribution: for turbulent flows, we outlined multi-modal distributions of mean age, whereas it tends to be linear for laminar flows. These multi modal distributions were further divided into multiple Gaussian curves and regions pertaining to these distributions were also identified using machine learning.

The presence of Kenics element increases the uniformity in mean age irrespective of the Reynolds number. As *Re* increases, a larger degree of uniformity in the mean age distribution is achieved. This phenomenon is visually depicted by scalar plots and quantitatively by the surface based frequency distribution of mean age. The decay of mean age reveals that the axial mixing is improved as the Reynolds number increases.

5.1 Future Work

Despite the innovative work presented in the current thesis, the definiteness of the critical observations deduced by visualising mean age, yet rely on several assumptions. In the current study we neglected diffusion by assigning a very high value to molecular diffusivity and the turbulent Schmidt number. A detailed study into the effect of diffusivity on the mean age distribution might paint a more accurate picture of mixing analysis via mean age. We also restricted our study to one type of static mixer, i.e. Kenics mixer, analysis of more mixers could reveal the efficacy of mean age distribution in predicting mixing.

In this study we also discovered the occurrence of multi modal distribution for various turbulent Reynolds number flows which contradicting to a well established view that the concentration of a dispersed phase is most likely defined by a Gaussian curve [19], [38], [71]. The reason behind the occurrence of these multi modal distribution can be attributed to the geometry of mixer and the chaotic turbulent flow field. However a more deeper study might reveal interesting reasons behind these multi modal distributions. A recent study by Forte *et al.* [38] reveals that a bi-modal distribution of liquid droplets was obtained when two immiscible liquids were mixed using a six element Kenics mixer. The mean age distributions for flows corresponding to $Re = 5069$ and $Re = 6843$ also presented with a bi modal distribution of mean age at certain cross sections. It is possible that with the help of mean age theory we might be able to predict the presence of multi modal distributions and could curb its occurrence if needed for better mixing of two quantities.

Bibliography

[1] A. Ghanem, T. Lemenand, D. Della Valle, and H. Peerhossaini, “Static mixers: Mechanisms, applications, and characterization methods - A review,” *Chemical Engineering Research and Design*, vol. 92, no. 2, pp. 205–228, 2014.

[2] F. Strieff and J. Rogers, “Don't overlook static mixer reactors,” *Chemical Engineering*, vol. May, pp. 76–82, 1994.

[3] R. K. Thakur, C. Vial, K. D. Nigam, E. B. Nauman, and G. Djelveh, “Static mixers in the process industries - a review,” *Chemical Engineering Research and Design*, vol. 81, no. 7, pp. 787–826, 2003.

[4] E. L. Paul, V. A. Atiemo-Obeng, and S. M. Kresta, Eds., *Handbook of Industrial Mixing*. Hoboken, NJ, USA: John Wiley & Sons, Inc., 2003.

[5] C. M. Khalde, V. Ramanan, J. S. Sangwai, and V. V. Ranade, “Passive Mixer cum Reactor Using Threaded Inserts: Investigations of Flow, Mixing, and Heat Transfer Characteristics,” *Industrial and Engineering Chemistry Research*, vol. 59, no. 9, pp. 3943–3961, 2020.

[6] J. Arimond and L. Erwin, “A Simulation of a Motionless Mixer,” *Chemical Engineering Communications*, vol. 37, no. 1-6, pp. 105–126, 1985.

[7] D. M. Hobbs and F. J. Muzzio, “The Kenics static mixer: A three-dimensional chaotic flow,” *Chemical Engineering Journal*, vol. 67, no. 3, pp. 153–166, 1997.

[8] W. F. Van Wageningen, D. Kandhai, R. F. Mudde, and H. E. Van Den Akker, “Dynamic flow in a kenics static mixer: An assessment of various CFD methods,” *AIChE Journal*, vol. 50, no. 8, pp. 1684–1696, 2004.

[9] E. Lang, P. Drtina, F. Streiff, and M. Fleischli, “Numerical simulation of the fluid flow and the mixing process in a static mixer,” *International Journal of Heat and Mass Transfer*, vol. 38, no. 12, pp. 2239–2250, 1995.

[10] H. S. Song and S. P. Han, “A general correlation for pressure drop in a Kenics static mixer,” *Chemical Engineering Science*, vol. 60, no. 21, pp. 5696–5704, 2005.

[11] R. K. Rahmani, T. G. Keith, and A. Ayasoufi, “Numerical simulation of turbulent flow in an industrial helical static mixer,” *International Journal of Numerical Methods for Heat & Fluid Flow*, vol. 18, no. 6, pp. 675–696, 2008.

[12] V. Kumar, V. Shirke, and K. Nigam, "Performance of Kenics static mixer over a wide range of Reynolds number," *Chemical Engineering Journal*, vol. 139, no. 2, pp. 284–295, 2008.

[13] C. Habchi, T. Lemenand, D. D. Valle, and H. Peerhossaini, "Turbulent mixing and residence time distribution in novel multifunctional heat exchangers-reactors," *Chemical Engineering and Processing: Process Intensification*, vol. 49, no. 10, pp. 1066–1075, 2010.

[14] M. Coroneo, G. Montante, and A. Paglianti, "Computational Fluid Dynamics Modeling of Corrugated Static Mixers for Turbulent Applications," *Industrial & Engineering Chemistry Research*, vol. 51, no. 49, pp. 15 986–15 996, 2012.

[15] M. Stec and P. M. Synowiec, "Study of fluid dynamic conditions in the selected static mixers part I- research of pressure drop," *Canadian Journal of Chemical Engineering*, vol. 95, no. 11, pp. 2156–2167, 2017.

[16] M. Stec and P. M. Synowiec, "Study of fluid dynamic conditions in the selected static mixers part II-determination of the residence time distribution," *Canadian Journal of Chemical Engineering*, vol. 95, no. 12, pp. 2410–2422, 2017.

[17] M. Stec and P. M. Synowiec, "Study of fluid dynamic conditions in the selected static mixers part III—research of mixture homogeneity," *Canadian Journal of Chemical Engineering*, vol. 97, no. 4, pp. 995–1007, 2019.

[18] H. Medina, M. Thomas, T. Eldredge, and A. Adebanjo, "The M Number: A Novel Parameter to Evaluate the Performance of Static Mixers," *Journal of Fluids Engineering, Transactions of the ASME*, vol. 141, no. 12, 2019.

[19] S. M. Kresta, A. W. Etchells III, and D. S. Dickey, Eds., *Advances in Industrial Mixing: A Companion to the Handbook of Industrial Mixing*. Hoboken: John Wiley & Sons Inc, 2016.

[20] P. V. Danckwerts, "The definition and measurement of some characteristics of mixtures," *Applied Scientific Research, Section A*, vol. 3, no. 4, pp. 279–296, 1952.

[21] A. Kukukova, J. Aubin, and S. M. Kresta, "A new definition of mixing and segregation: Three dimensions of a key process variable," *Chemical Engineering Research and Design*, vol. 87, no. 4, pp. 633–647, 2009.

[22] G. Montante, M. Coroneo, and A. Paglianti, "Blending of miscible liquids with different densities and viscosities in static mixers," *Chemical Engineering Science*, vol. 141, pp. 250–260, 2016.

[23] R. K. Rahmani, T. G. Keith, and A. Ayasoufi, "Three-Dimensional Numerical Simulation and Performance Study of an Industrial Helical Static Mixer," *Journal of Fluids Engineering*, vol. 127, no. 3, p. 467, 2005.

[24] D. Hobbs and F. Muzzio, "Reynolds number effects on laminar mixing in the Kenics static mixer," *Chemical Engineering Journal*, vol. 70, no. 2, pp. 93–104, 1998.

[25] K. Abou Hweij and F. Azizi, "Hydrodynamics and residence time distribution of liquid flow in tubular reactors equipped with screen-type static mixers," *Chemical Engineering Journal*, vol. 279, pp. 948–963, 2015.

[26] M. Sheoran, A. Chandra, H. Bhunia, P. K. Bajpai, and H. J. Pant, "Residence time distribution studies using radiotracers in chemical industry—A review," *Chemical Engineering Communications*, vol. 205, no. 6, pp. 739–758, 2018.

[27] M. Liu and J. N. Tilton, "Spatial distributions of mean age and higher moments in steady continuous flows," *AIChE Journal*, vol. 56, no. 10, pp. 2561–2572, 2010.

[28] M. Liu, "Age distribution and the degree of mixing in continuous flow stirred tank reactors," *Chemical Engineering Science*, vol. 69, no. 1, pp. 382–393, 2012.

[29] M. Coroneo, G. Montante, A. Paglianti, and F. Magelli, "CFD prediction of fluid flow and mixing in stirred tanks: Numerical issues about the RANS simulations," *Computers and Chemical Engineering*, vol. 35, no. 10, pp. 1959–1968, 2011.

[30] P. V. Danckwerts, "Continuous flow systems. Distribution of residence times," *Chemical Engineering Science*, vol. 2, no. 1, pp. 1–13, 1953.

[31] J. N. Baléo and P. Le Cloirec, "Numerical simulation of the spatial distribution of mean residence time in complex flows through porous media," *Progress of Theoretical Physics Supplement*, vol. 138, no. 138, pp. 690–695, 2000.

[32] M. Liu, "Quantitative characterisation of mixing in stirred tank reactors with mean age distribution," *The Canadian Journal of Chemical Engineering*, vol. 89, no. 5, pp. 1018–1028, 2011.

[33] M. Liu, "Computational study of convective-diffusive mixing in a microchannel mixer," *Chemical Engineering Science*, vol. 66, no. 10, pp. 2211–2223, 2011.

[34] E. Immonen, "CFD optimization of jet fan ventilation in a car park by fractional factorial designs and response surface methodology," *Building Simulation*, vol. 9, no. 1, pp. 53–61, 2016.

[35] T. T. Tran, T. T. Vo, S. C. Cho, D. H. Lee, and W. R. Hwang, "A stir casting system for drawdown of light particles in manufacturing of metal matrix composites," *Journal of Materials Processing Technology*, vol. 257, pp. 123–131, 2018.

[36] D. C. Russ and R. E. Berson, "Mean age theory in multiphase systems," *Chemical Engineering Science*, vol. 141, pp. 1–7, 2016.

[37] Simcenter STAR-CCM+, *Simcenter STAR-CCM+*, 2020.

[38] G. Forte, E. Brunazzi, and F. Alberini, "Effect of residence time and energy dissipation on drop size distribution for the dispersion of oil in water using KMS and SMX+ static mixer," *Chemical Engineering Research and Design*, vol. 148, pp. 417–428, 2019.

[39] S. B. Pope, *Turbulent Flows*, 11. IOP Publishing, 2001, vol. 12, pp. 2020–2021.

[40] H. Versteeg, W. Malalasekera, G. Orsi, J. H. Ferziger, A. W. Date, and J. D. Anderson, *An Introduction to Computational Fluid Dynamics - The Finite Volume Method*. 1995, p. 267. arXiv: arXiv:1011.1669v3.

[41] T. H. Shih, W. W. Liou, A. Shabbir, Z. Yang, and J. Zhu, "A new k-ε eddy viscosity model for high reynolds number turbulent flows," *Computers and Fluids*, vol. 24, no. 3, pp. 227–238, 1995.

[42] F. Billard and D. Laurence, "A robust k-ε-$\overline{\nu^2} \setminus k$ elliptic blending turbulence model applied to near-wall, separated and buoyant flows," *International Journal of Heat and Fluid Flow*, vol. 33, no. 1, pp. 45–58, 2012.

[43] B. E. Launder, G. J. Reece, and W. Rodi, "Progress in the development of a Reynolds-stress turbulence closure," *Journal of Fluid Mechanics*, vol. 68, no. 3, pp. 537–566, 1975.

[44] F. G. Schmitt, "About Boussinesq's turbulent viscosity hypothesis: historical remarks and a direct evaluation of its validity," 2008.

[45] F. Billard, A. Revell, and T. Craft, "Application of recently developed elliptic blending based models to separated flows," *International Journal of Heat and Fluid Flow*, vol. 35, pp. 141–151, 2012.

[46] M. M. Gibson and B. E. Launder, "Ground effects on pressure fluctuations in the atmospheric boundary layer," *Journal of Fluid Mechanics*, vol. 86, no. 3, pp. 491–511, 1978.

[47] B. E. Launder, *Second-moment closure: present... and future?* 1989.

[48] S. V. Patankar and D. B. Spalding, "A calculation procedure for heat, mass and momentum transfer in three-dimensional parabolic flows," *International Journal of Heat and Mass Transfer*, vol. 15, no. 10, pp. 1787–1806, 1972.

[49] E. Shima, K. Kitamura, and T. Haga, "Green-Gauss/weighted-least-squares hybrid gradient reconstruction for arbitrary polyhedra unstructured grids," *AIAA Journal*, vol. 51, no. 11, pp. 2740–2747, 2013.

[50] V. Venkatakrishnan, "On the accuracy of limiters and convergence to steady state solutions," in *31st Aerospace Sciences Meeting*, Reston, Virigina: American Institute of Aeronautics and Astronautics, 1993.

[51] Ansys, *Ansys ICEM*.

[52] B. E. Launder and D. B. Spalding, "The numerical computation of turbulent flows," *Computer Methods in Applied Mechanics and Engineering*, vol. 3, no. 2, pp. 269–289, 1974.

[53] P. V. Danckwerts, "Local residence-times in continuous-flow systems," *Chemical Engineering Science*, vol. 9, no. 1, pp. 78–79, 1958.

[54] D. B. Spalding, "A note on mean residence-times in steady flows of arbitrary complexity," *Chemical Engineering Science*, vol. 9, no. 1, pp. 74–77, 1958.

[55] M. Sandberg, "What is ventilation efficiency?" *Building and Environment*, vol. 16, no. 2, pp. 123–135, 1981.

[56] G. Montante and F. Magelli, "Liquid homogenization characteristics in vessels stirred with multiple Rushton turbines mounted at different spacings: CFD study and comparison with experimental data," *Chemical Engineering Research and Design*, vol. 82, no. 9 SPEC. ISS. Pp. 1179–1187, 2004.

[57] M. Liu, "Age distribution in the kenics static micromixer with convection and diffusion," *Industrial and Engineering Chemistry Research*, vol. 51, no. 20, pp. 7081–7094, 2012.

[58] P. D. Berkman and R. V. Calabrese, "Dispersion of viscous liquids by turbulent flow in a static mixer," *AIChE Journal*, vol. 34, no. 4, pp. 602–609, 1988.

[59] C. D. Grace, "Static mixing and heat transfer," *Chemical and Process Engineering*, vol. 52, no. 7, p. 57, 1971.

[60] M. H. Pahl and E. Muschelknautz, "Statische Mischer und ihre Anwendung," *Chemie Ingenieur Technik*, vol. 52, no. 4, pp. 285–291, 1980.

[61] A. Cybulski and K. Werner, "Static mixers - criteria for applications and selection," *International chemical engineering*, vol. 26, no. 1, pp. 171–180, 1986.

[62] P. Joshi, K. D. Nigam, and E. B. Nauman, "The Kenics static mixer: new data and proposed correlations," *The Chemical Engineering Journal and The Biochemical Engineering Journal*, vol. 59, no. 3, pp. 265–271, 1995.

[63] W. E. Genetti, "Laminar flow heat transfer with inline mixers inserts," *Chemical Engineering Communications*, vol. 14, no. 1-2, pp. 47–57, 1982.

[64] V. Kumar, V. Shirke, and K. Nigam, "Performance of Kenics static mixer over a wide range of Reynolds number," *Chemical Engineering Journal*, vol. 139, no. 2, pp. 284–295, 2008.

[65] J. Šír and Z. Lecjaks, "Pressure drop and homogenization efficiency of a motionless mixer," *Chemical Engineering Communications*, vol. 16, no. 1-6, pp. 325–334, 1982.

[66] L. E. Wagner and D. Ding, "Representing Aggregate Size Distributions as Modified Lognormal Distributions," *Transactions of the ASAE*, vol. 37, no. 3, pp. 815–821, 1994.

[67] A. Moitra, "Gaussian Mixture Models," in *Algorithmic Aspects of Machine Learning*, Cambridge University Press, 2018, pp. 107–131.

[68] M. Simcik, M. C. Ruzicka, A. Mota, and J. A. Teixeira, "Smart RTD for multiphase flow systems," *Chemical Engineering Research and Design*, vol. 90, no. 11, pp. 1739–1749, 2012.

[69] Indratmo, L. Howorko, J. M. Boedianto, and B. Daniel, "The efficacy of stacked bar charts in supporting single-attribute and overall-attribute comparisons," *Visual Informatics*, vol. 2, no. 3, pp. 155–165, 2018.

[70] D. Cournapeau, F. Pedregosa, V. Michel, O. Grisel, M. Blondel, P. Prettenhofer, R. Weiss, J. Vanderplas, D. Cournapeau, F. Pedregosa, G. Varoquaux, A. Gramfort, B. Thirion, O. Grisel, V. Dubourg, A. Passos, M. Brucher, M. Perrot andÉdouardand, A. Duchesnay, and Duchesnay Edouard, "Scikit-learn: Machine Learning in Python," *Journal of Machine Learning Research*, vol. 12, no. 7, pp. 2825–2830, 2011.

[71] O. Levenspiel, *Chemical reaction engineering*. Wiley, 1999, p. 668.

[72] O Byrde and M. L. Sawley, "Optimization of a Kenics static mixer for non-creeping flow conditions," *Chemical Engineering Journal*, vol. 72, no. 2, pp. 163–169, 1999.

[73] H. Weltens, H. Bressler, F. Terres, H. Neumaier, and D. Rammoser, "Optimisation of catalytic converter gas flow distribution by CFD prediction," in *SAE Technical Papers*, SAE International, 1993.

Appendix A: Residence Time Distribution

A.1 Introduction

As defined by Danckwerts [30], residence time is the amount of time required by the fluid molecule to traverse from the point of injection to the outlet of the system. A distribution of these residence times also well known as the residence time distribution (RTD) is commonly defined by an "E-curve". To estimate the RTD of a closed system (i.e with one inlet and one outlet), a small amount of tracer is injected into the system. Then the exit concentration of the tracer at the outlet, $C(t)$, is measured until the injected tracer is completely washed out from the system. The time during which it happens is denoted as t_∞. The "E-curve", or the distribution, is mathematically represented as follows:

$$E(t) = \frac{C(t)}{\int\limits_0^{t_\infty} C(t)dt} \tag{A.1}$$

The first moment of the distribution determines the average amount of time spent by a fluid molecule within the system, i.e. the mean residence time τ_m:

$$\tau_m = \int\limits_0^\infty tE(t)dt \tag{A.2}$$

The second and the third moments of the curve determine the variance, γ^2, and the skewness, s_k, of the distribution, respectively, and are calculated as follows:

$$\gamma^2 = \int\limits_0^\infty (t-\tau_m)^2 E(t)dt \tag{A.3}$$

$$s_k = \frac{\int\limits_0^\infty (t-\tau_m)^3 E(t)dt}{\tau_m^3} \tag{A.4}$$

Using these quantities, we can assess the mixing performance of the system, for instance, by evaluating the coefficient of variance, $CoV = \gamma/\tau_m$, of the distribution. A CoV of zero indicates complete distributive mixing, whereas CoV of one indicates total segregation.

A.2 Evaluating Residence Time Distribution

In this study, we used simulations of a passive scalar flow to determine the RTD curve. The passive scalar behaves as a contaminant and does not affect the dynamics of the flow. The transport of the passive scalar is governed by the following transient convection-diffusion equation

$$\frac{\partial C}{\partial t} + \nabla \cdot (\mathbf{U}C) = \nabla \cdot (D\nabla C) + S_C \tag{A.5}$$

where D is the diffusivity coefficient, and S_C is the source term. The linear eddy diffusivity model [37] is used to estimate the diffusivity coefficient:

$$D = \frac{\mu}{\sigma_m} + \frac{\mu_t}{\sigma_t} \tag{A.6}$$

where σ_m is the molecular Schmidt number and σ_t is the turbulent Schmidt number. Since the purpose of the study is to assess the effect of convection and turbulence rather than mixing due to molecular diffusion, the molecular Schmidt number was fixed to a value of 10^{10} m^2/s meaning that molecular diffusion is negligibly small. The contribution of molecular diffusion i.e μ/σ, to the overall tracer dispersion process is expected to be small for turbulent flows [14]. The turbulent Schmidt number was set to 0.7 which is commonly suggested in the literature [14], [56].

The flow fields obtained from the steady state simulations of the flow in the mixer were used as initial conditions for the passive scalar simulations. The simulation was switched to a transient mode. Then the passive scalar was injected at 2 mm before the leading edge of the first Kenics element during $\Delta t = 0.01$ seconds by maintaining the value of the source term, S_C, equal to unity. The initial concentration of the scalar in the entire domain was set to zero. The amount of scalar concentration C_{out} at the outlet was tracked as a function of time until it reached zero values at the outlet of the domain.

The false diffusion arising from the numerical discretization of Equation (A.5) was mitigated by using high-quality grid D and small time steps [72]. A second order spatial discretization scheme and a second order implicit temporal discretization scheme were used. The time step was set to 10^{-4} with 10 inner iterations per time step. The solution convergence was ensured by achieving the residual level below 10^{-4}.

A.3 Results and Discussion

The residence time distribution functions, $E(t)$, obtained for the turbulent flows in the Kenics mixer corresponding to the Reynolds number of 5069, 6843, 9504, 10 391 and 12 000 are shown in Figure A.1. With the increase in the Reynolds number of the flow the RTD curves reach a higher maximum along with a reduced span along the $x-$axis. Figure A.1 indicates that as the Reynolds number increases, the fluid spends less time within the mixer. The second observation is that with the wider span of the curve (lower Reynolds number) there is more deviation between the amount of time fluid parcels spends within the device.

The span of the RTD curve can be quantified by evaluating variance, γ^2, using Equation A.4. The variance of the RTD curves are given in Table A.1 for the flow in the mixer and empty pipe. These observations are consistent with the observations of: the RTD is a strong function of the Reynolds number and flow in static mixers cannot be considered as an ideal plug flow where the amount of time each fluid element stays inside the system remains identical [71] [15]. Increase in the Reynolds number leads to decrease of the variance. The reason for this can be attributed to the flattening of the velocity profile in the turbulent flow regime as shown in Figure 3.14 which results in a parallel motion of particles across a larger fraction of the flow area.

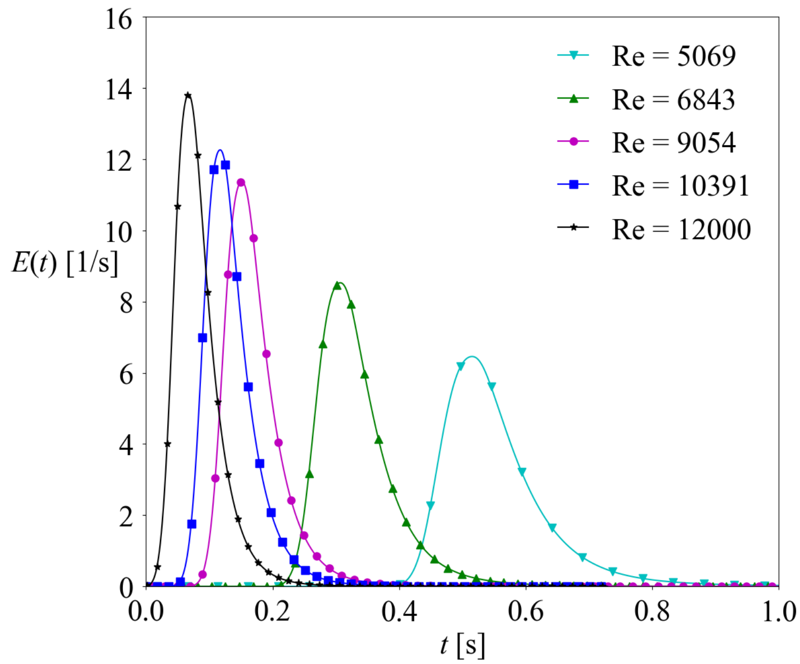

Figure A.1: E-curves for Kenics mixer

Table A.1: Variance of RTD

Re	5069	6843	9504	10391	12000
Pipe	1.60×10^{-2}	9.78×10^{-3}	4.20×10^{-3}	3.24×10^{-3}	2.12×10^{-3}
Kenics mixer	8.37×10^{-3}	4.30×10^{-3}	2.15×10^{-3}	1.79×10^{-3}	1.37×10^{-3}

The RTD curves for the flow through the mixer corresponding to the Reynolds numbers of 5069 and 12 000 are plotted alongside with the RTD curves of a pipe flow in Figure A.2a. The peak of the E-curve for a pipe flow is higher with a smaller overall span at the bottom implying that the flow of particles is more streamlined i.e parallel in case of turbulent pipe flow. This is expected as the absence of obstacles, i.e. Kenics elements, will result in a less disturbed flow (refer to the velocity profile of pipe flow in Figure 3.14). However, the tails of RTD curves for pipe flow extend longer than those for Kenics mixer implying larger skewness, S_k, for RTD's corresponding to pipe flow [27]. The magnitudes of skewness for RTD's curves is tabulated in Table A.3 alongside CoV and mean residence time. A long tail also implies longer time for the entire passive scalar to was out of the system. This can be further elaborated by a cumulative residence time distribution (CRTD).

A dimensionless form of the RTD function corresponding to the Reynolds numbers of 5069 and 12 000 is presented in Figure A.2b. Time was dimensionalised with τ_m (see Equation A.2) $\theta = t/\tau_m$. Abou Hweij and Azizi [25] states that a larger axial dispersion at higher Reynolds number can be observed by an increased span and smaller peak in a dimensionless RTD curve. A similar deduction can be made from Figure A.2b. This diffusive effect in the scalar concentration can be marked as the direct causation of increase in distribution of momentum across different directions in turbulent flows (Shown by scalar plots in Figure 3.13). However such an observation can not be made from the normalised RTD curves for pipe flow where a higher Reynolds number flow is still accompanied by taller peaks and smaller span.

A CRTD curve also specifies the fraction of concentration within the device at any moment in time and can be evaluated using Equation (A.7).

$$F(t) = \int_0^t E(t)dt \tag{A.7}$$

The maximum and minimum amount of time spent by a molecule within the system can also be revealed by evaluating cumulative residence time distribution (CRTD). The CRTD curves for the pipe flow and flow through the mixer at different Reynolds numbers are shown in Figure A.4. The passive scalar is completely washed out of the system when $F(t) = 1$. The time at which $F(t)$ approaches unity is given in Table A.2. As can be seen from the results, this time is higher for the pipe flow compared to the flow in the mixer. The presence of longer tail at the end of the RTD curve for pipe flow results in a higher magnitude of time required by the last volume element to was out of the system. The quantitative comparison the tail of an RTD curve can be done by evaluating skewness, S_k of the curve. The skewness of RTD curves for flows across two different systems at various Reynolds numbers are presented in Table A.3.

Table A.2: The amount of time required (in seconds) to wash out of the system

Re	Pipe	Kenics mixer
5069	1.83	1.57
6843	1.61	1.08
9504	1.06	7.33×10^{-1}
10391	9.25×10^{-1}	6.63×10^{-1}
12000	7.48×10^{-1}	5.67×10^{-1}

The reduction in mean residence time, τ_m, with the increase of the Reynolds number is shown in Figure A.6. The mean residence time for the pipe flow is consistently lower than for the flow in the mixer for each Reynolds number. The ratio between the mean residence time for pipe flow and the flow in the mixer ranges between 1.045 to 1.071. At higher Reynolds numbers it is expected that the ratio of mean residence times across different flow systems will approach unity [16]. The study carried out by Abou Hweij and Azizi [25] points out that RTD analysis could help reveal the existence of dead volumes or occurrence of channeling or bypassing within the device. For that the mean residence time obtained from "E-curves" is compared with the theoretical one in Figure A.6. A theoretical residence time, τ, is the ratio of the volume of the device to the volume flow rate of the system. The theoretical residence time for both pipe and the Kenics mixer is approximately similar as the volume of inserts

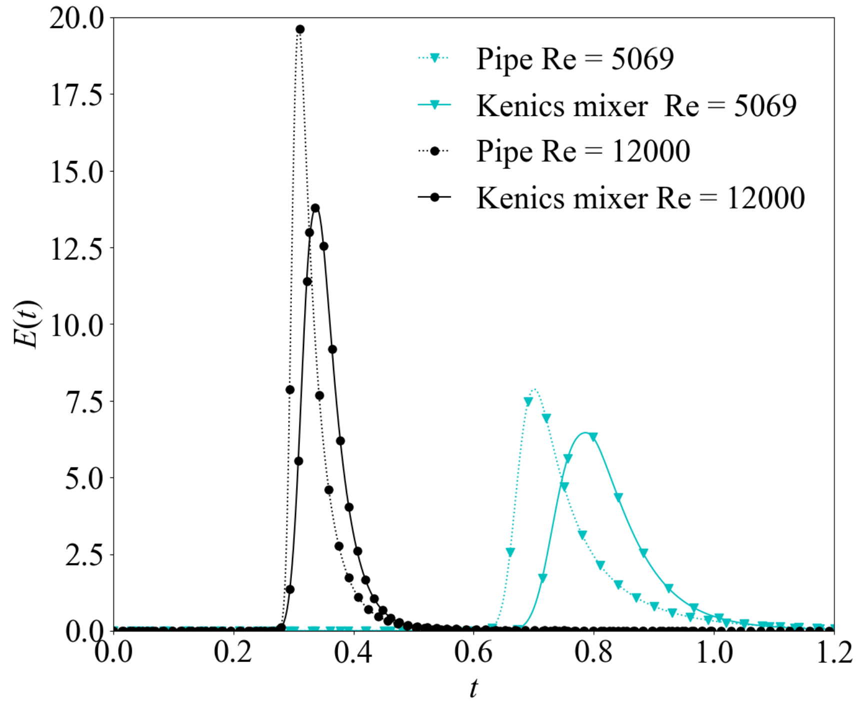

(a) Residence time distribution

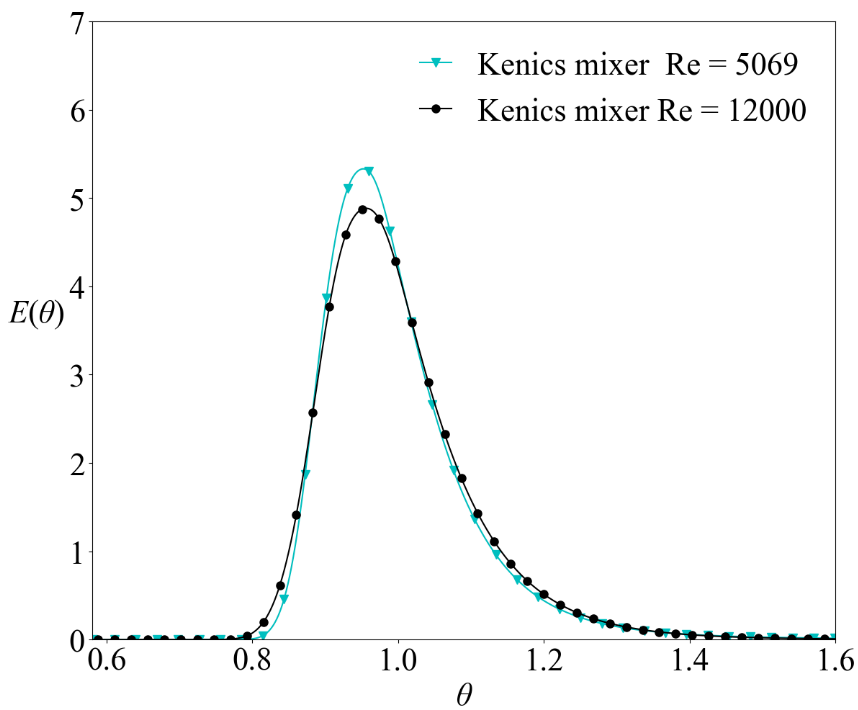

(b) Normalised Residence time distribution

Figure A.2: RTD curves

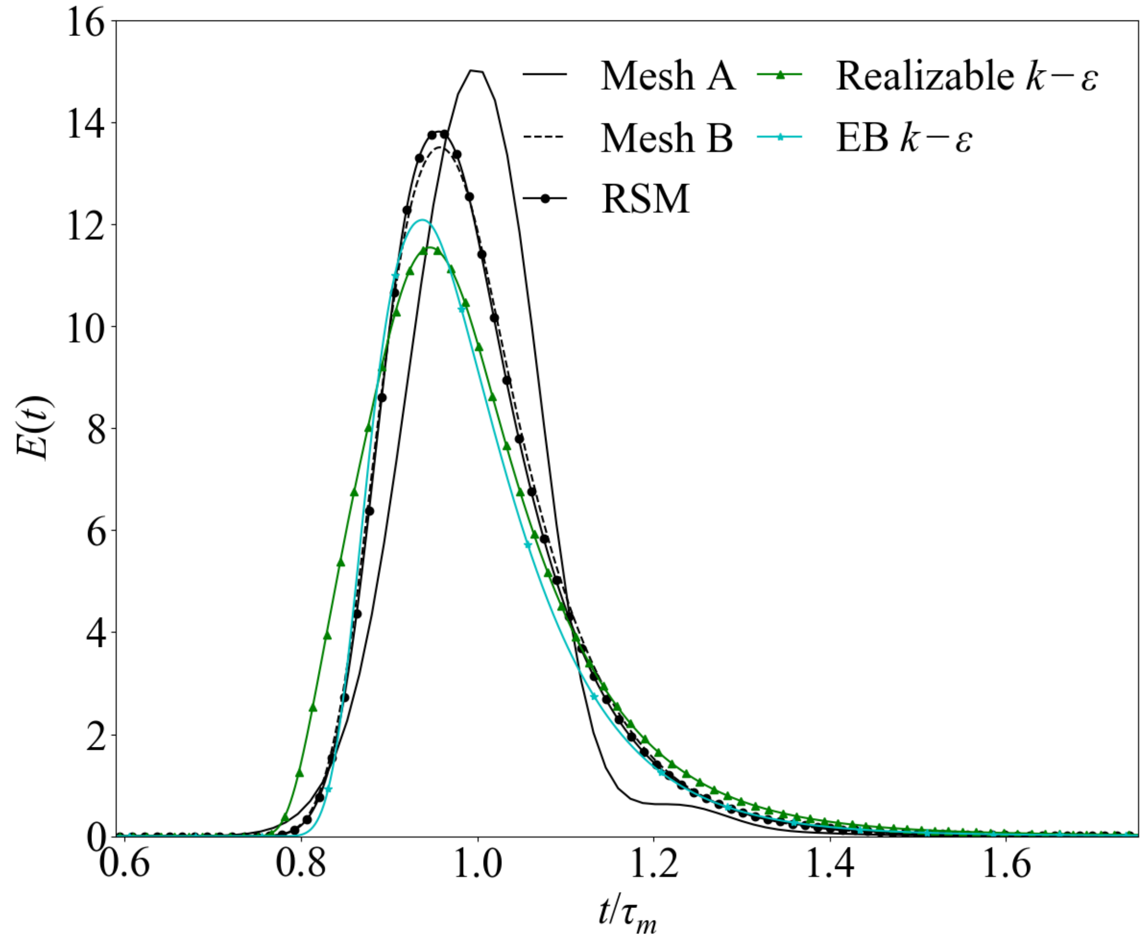

Figure A.3: Residence time distribution obtained on different grids and turbulent models

is very small in magnitude compared to the volume of the domain extending from the point of injection up till the outlet. The higher value of mean residence time for Kenics mixer when compared to the theoretical residence time indicates absence of dead zones, short circuiting, bypassing or channeling of flow [16]. The theoretical residence time for pipe is approximately equal to that of obtained via CFD. The equality of the two indicates that the flow passes undisturbed unlike the Kenics mixer. However, a digression from theoretical residence time seems to be appearing as the flow becomes more chaotic and turbulent.

Another important aspect revealed by the RTD analysis is the deviation from the ideal flows. There are three ideal cases. The first one being the piston flow or ideal plug flow. The second one being the laminar flow in an empty pipe and the third one being the ideal mixing flow within a continuous stirred tank reactor (CSTR). The plug flow and CSTR flows are the extreme for a well-designed reactor within the turbulent flow. To reveal the deviation of the flow across the Kenics mixer and pipe from the ideal behaviour we plot, $F(\theta)$ curves in Figure A.7. It can be observed that niether of the systems follow idealised curves. It is also noticeable that the $f(\theta)$ curves for pipe closely resemble to that of Kenics mixer.

The extent of radial mixing can be quantified by evaluating the magnitude of CoV. Ther CoV for different RTD curves are given in Table A.3. For both pipe

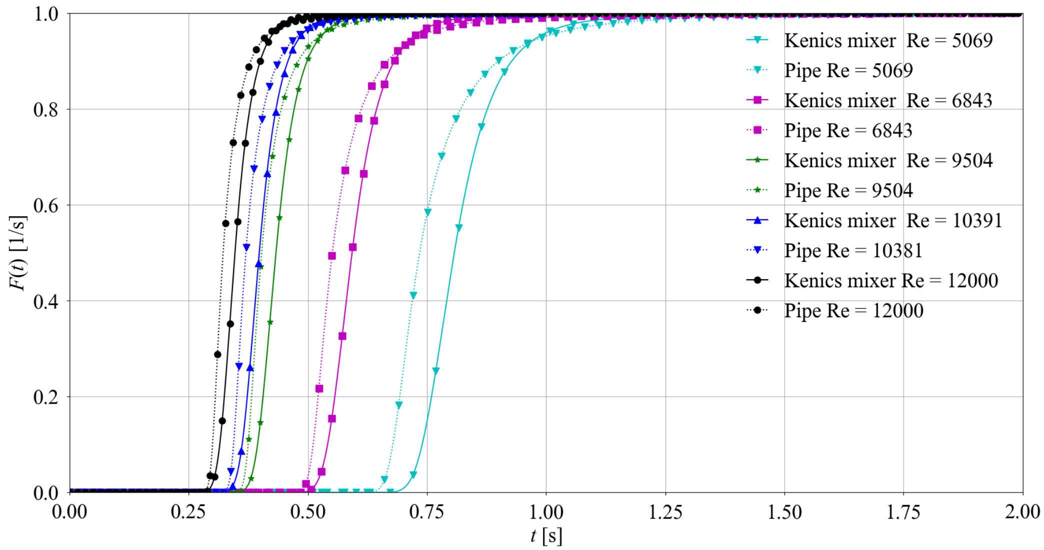

Figure A.4: Cumulative Residence time distribution for pipe and Kenics mixer

and mixer flows, the increase in axial velocity of the flow results in a decrement in the value of CoV. Although the reduction is more prominent in case of a pipe flow. As expected the CoV of RTD distribution obtained for Kenics mixer flows is on an average approximately 45 percent smaller than that of pipe irrespective of the Reynolds number of the flow. The presence of Kenics inserts certainly enhances mixing characteristics of the system. However the rise in CoV with increase Reynolds number of the flow is not substatial. The CoV of the flows corresponding to Reynolds of 10 931 and 12 000 is approximately similar.

Table A.3: Features that extracted from the moments of the RTD curve.

	Kenics mixer			Pipe		
Re	τ_m	CoV	S_k	τ_m	CoV	S_k
5069	8.25×10^{-1}	1.11×10^{-1}	1.64×10^{-1}	7.71×10^{-1}	1.64×10^{-1}	2.54×10^{-1}
6843	6.05×10^{-1}	1.08×10^{-1}	1.58×10^{-1}	5.78×10^{-1}	1.71×10^{-1}	2.94×10^{-1}
9054	4.42×10^{-1}	1.05×10^{-1}	1.43×10^{-1}	4.20×10^{-1}	1.54×10^{-1}	2.65×10^{-1}
10391	4.06×10^{-1}	1.04×10^{-1}	1.39×10^{-1}	3.85×10^{-1}	1.48×10^{-1}	2.50×10^{-1}
12000	3.53×10^{-1}	1.05×10^{-1}	1.38×10^{-1}	3.34×10^{-1}	1.38×10^{-1}	2.25×10^{-1}

The skewness and CoV of the curves in Figure A.1 alongside τ_m is shown in Table A.4 for different turbulent models and grids. The mean, standard deviation and skewness for the RTD curves at different Reynolds number is given in A.3 The RTD curves for flows corresponding to different Reynolds numbers are shown in Figure A.1. The same is shown on a normalised time scale in Figure A.5. It can be seen that with increment in Reynolds number the curves become steeper with reduction in deviation about the mean residence time. A reduction in mean residence time with increment in RTD is shown in Figure A.6.

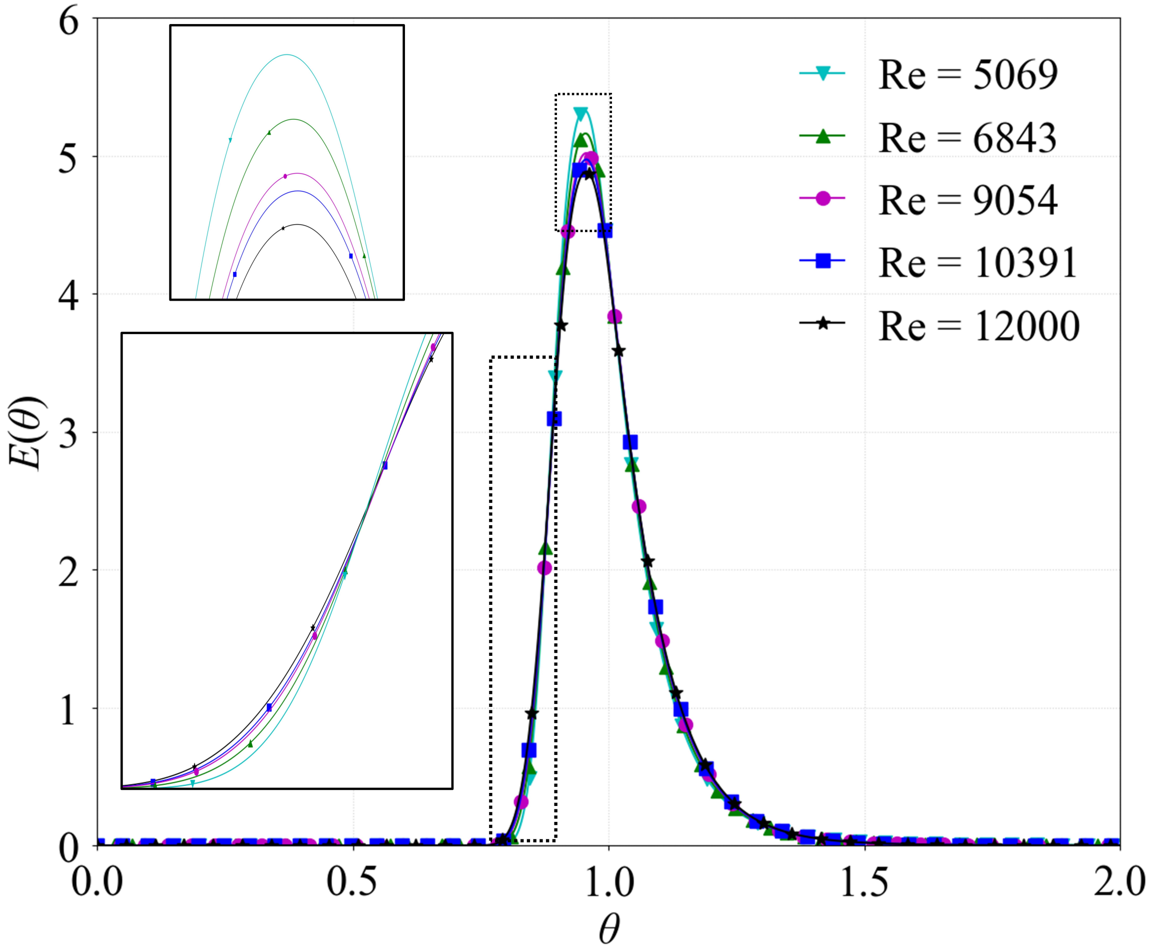

Figure A.5: Normalised Residence time distribution obtained for different Reynolds number flows

Table A.4: Moments of RTD curve predicted by simulating passive scalar on flow fields obtained using various turbulence models.

Grid	Turbulence model	τ_m	CoV	s_k
A	RSM	3.57×10^{-1}	8.44×10^{-2}	8.40×10^{-1}
B	RSM	3.49×10^{-1}	1.02×10^{-1}	1.06
C	RSM	3.53×10^{-1}	1.05×10^{-1}	1.1
C	Realizable $k-\varepsilon$	3.51×10^{-1}	1.37×10^{-1}	1.59
C	EB $k-\varepsilon$	3.98×10^{-1}	1.21×10^{-1}	1.20

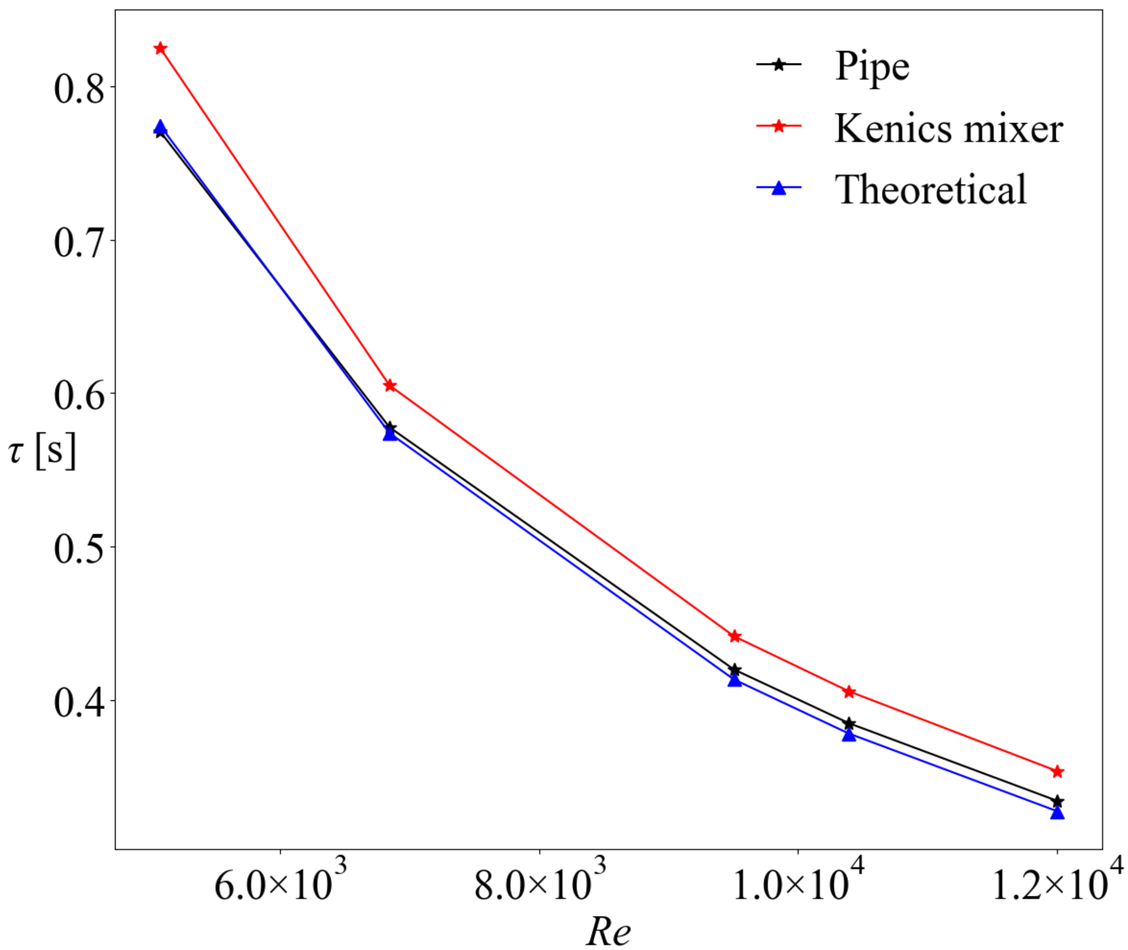

Figure A.6: Variation in Mean residence time as Reynolds number is increased

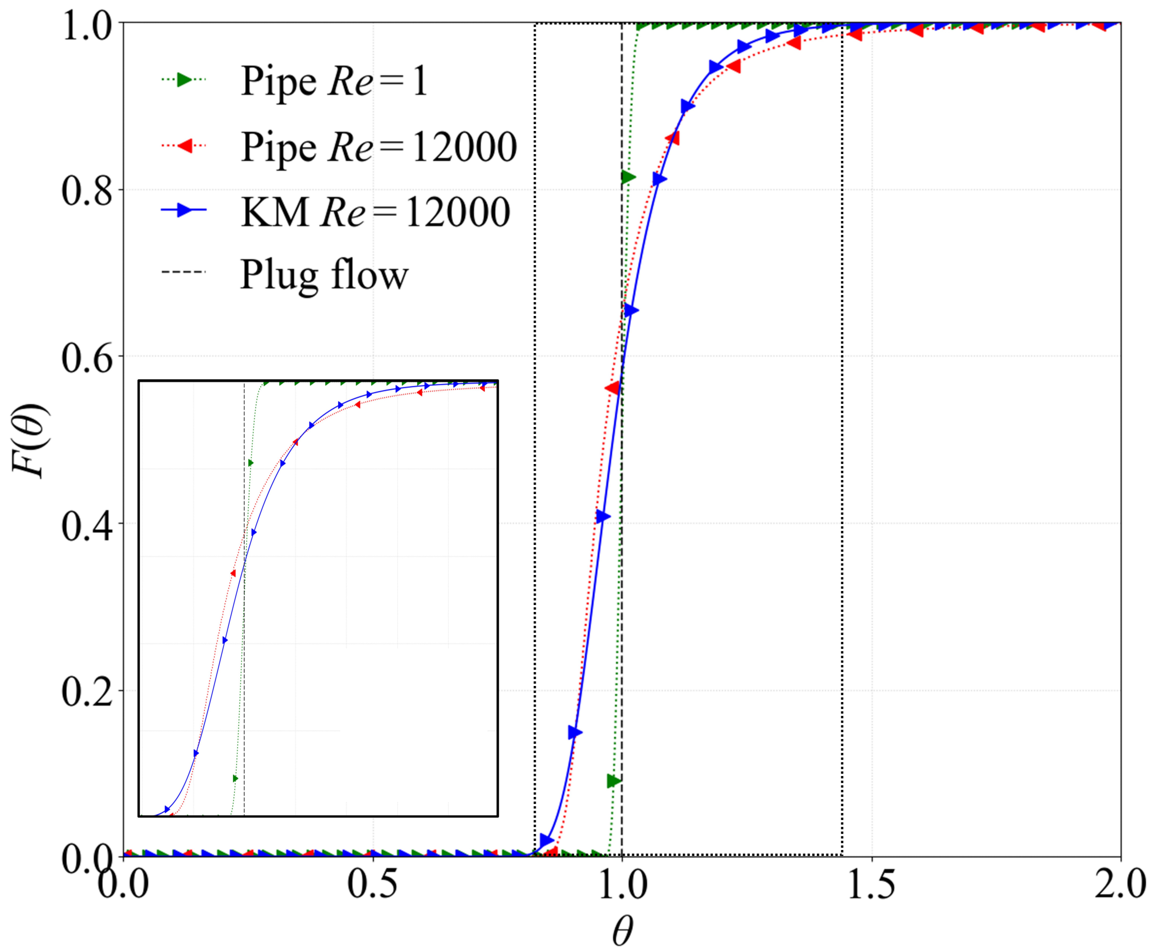

Figure A.7: Comparing Mixing

A.3.1 Blending Time

The amount of time required by a fluid to blend within a confined space can be predicted by evaluating change in volume uniformity of passive scalar. The volume uniformity of any scalar describes the distribution of a certain quantity in a given volume [73]. The volume uniformity of passive scalar is evaluated at each time step using Equation A.8 over a volume domain extending from the end of sixth element up till the outlet. The plots of same are presented in Figure A.8. A linear rise in volume uniformity is observed in the case of all the simulated cases, the effect of grid and turbulence model is shown more clearly by the gradient of volume uniformity in Figure A.9. In an ideal case a well mixed region can be indicated by volume uniformity equivalent to unity. The semi-log plots in Figure A.9 demonstrate a reduction in the change of change of volume uniformity requiring an infinite amount of time for ω to reach unity given the numerical errors are non existent. It is widely excepted that a volume domain with ω greater than 0.95 can be considered well mixed. The time required to achieve ω equal to 0.95 is represented as the blending time or $\omega_{0.95}$. The $\omega_{0.95}$ for all the simulated cases are shown in Table A.5. A mesh Independence can be observed as the difference between the $\omega_{0.95}$ of two systematically refined grid reduces.

The time required to achieve $\omega_{0.95}$ for various turbulent Reynolds number cases is shown in Figure A.10. An inverse relation between the blending time and the Reynolds number can be observed. The variation in volume uniformity with time for different Reynolds number can be seen in Figure A.11.

$$\omega = 1 - \frac{\sum_j V_j |\Phi_j - \Phi_v|}{2|\Phi_v| \sum_j V_j} \tag{A.8}$$

Table A.5: Blending time

Mesh	Turbulence Model	$\omega_{0.95}$ (s)
A	EB $k-\varepsilon$	0.35
B	EB $k-\varepsilon$	0.385
C	EB $k-\varepsilon$	0.3865
D	EB $k-\varepsilon$	0.3620
D	Realizable $k-\varepsilon$	0.368
D	RSM	0.3635

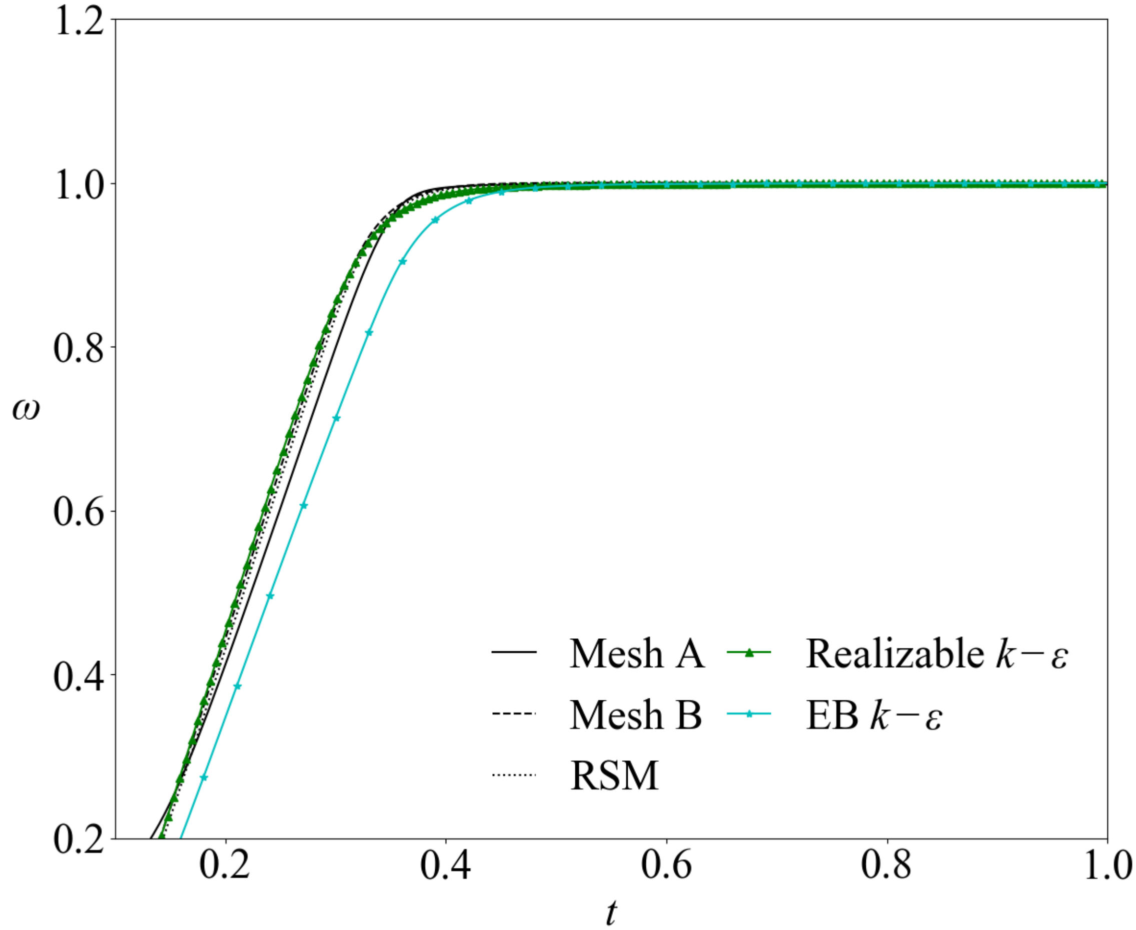

Figure A.8: Volume uniformity of passive scalar

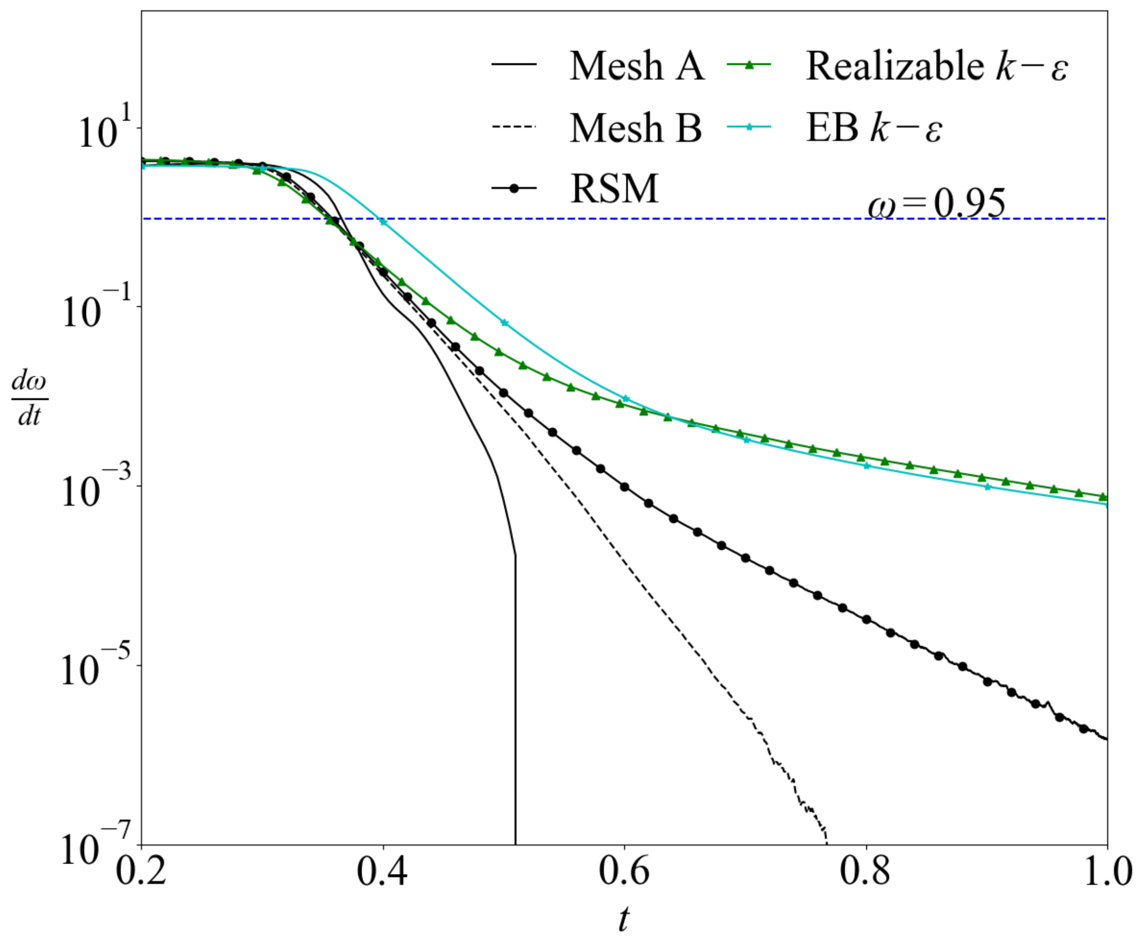

Figure A.9: Change in gradient of volume uniformity with time

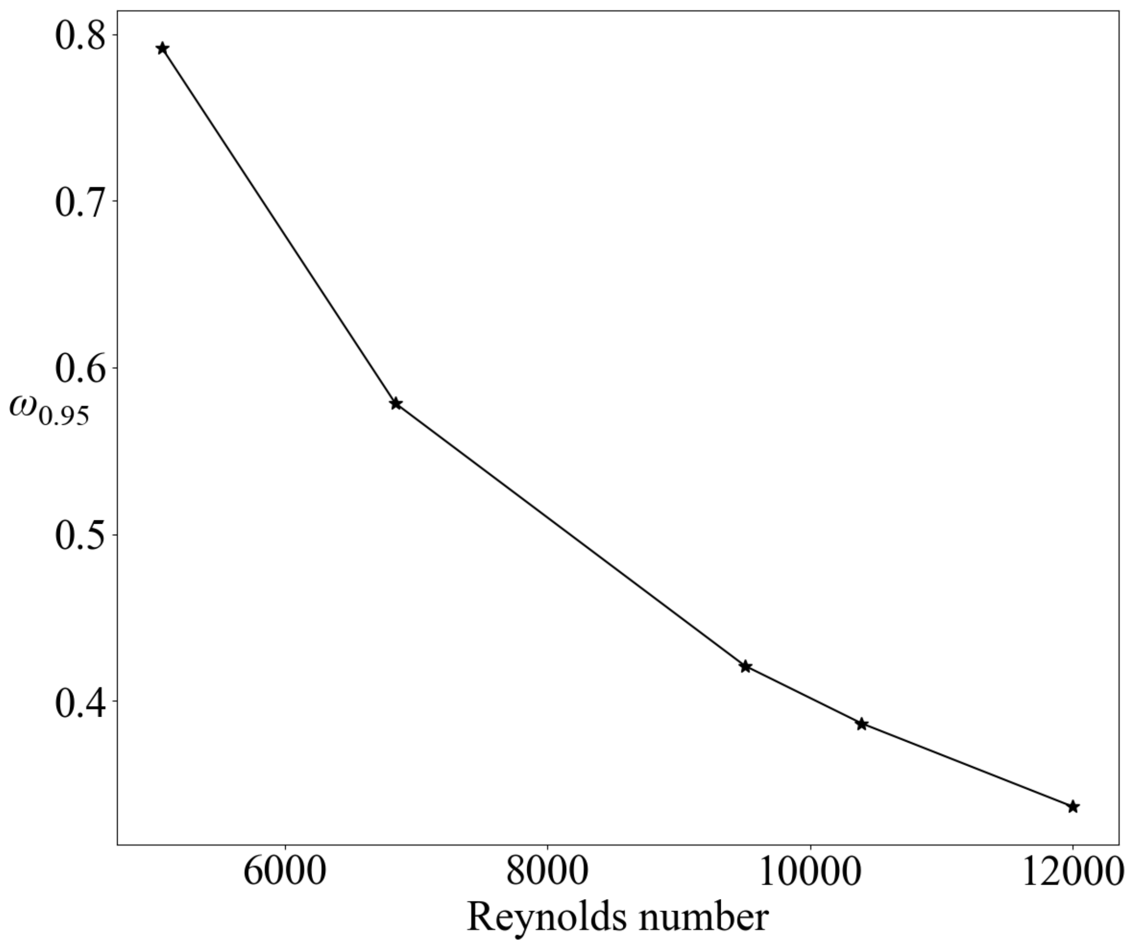

Figure A.10: Blending time as a function of Reynolds number

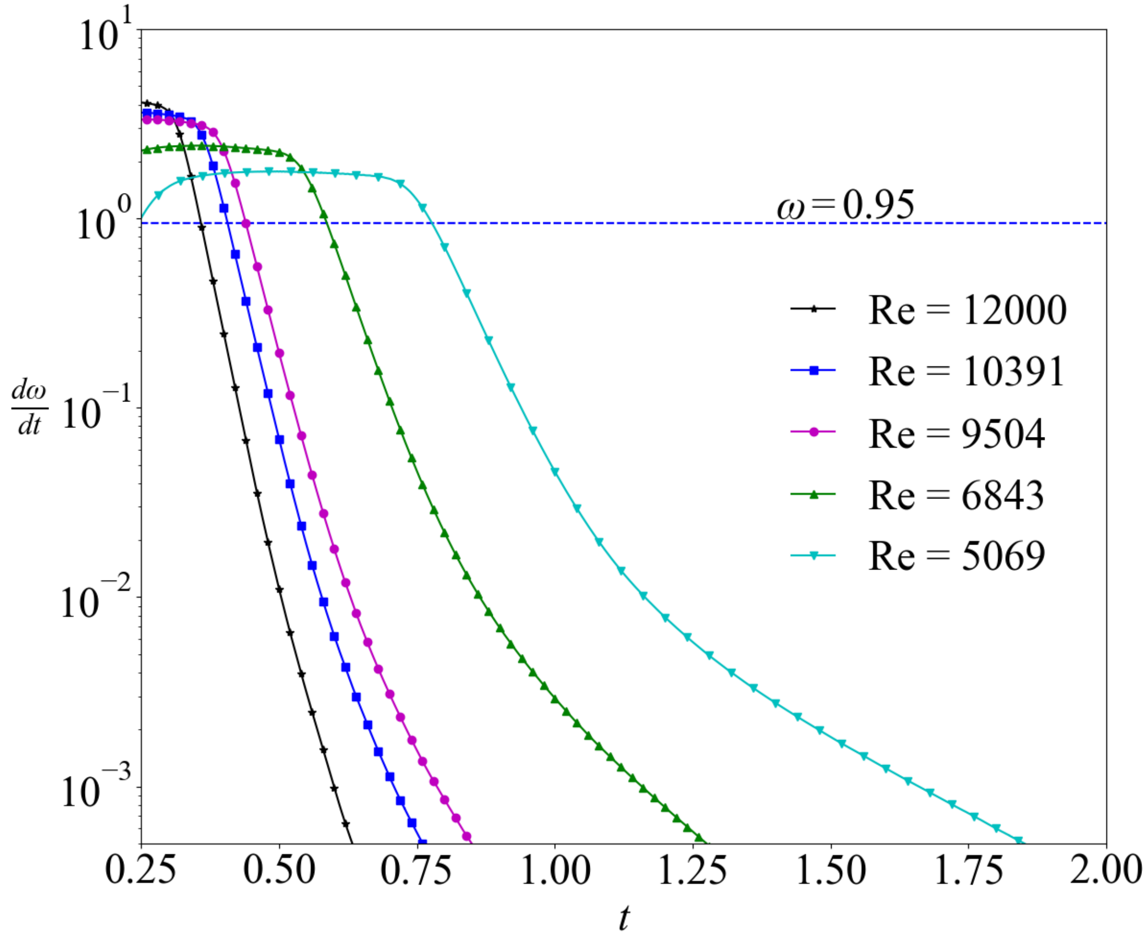

Figure A.11: Change in gradient of volume uniformity with time for different Reynolds number flows

Appendix B: Setting Up Mean Age Simulations in STAR-CCM+

In this Appendix we step by step illustrate on how to obtain Mean Age Distribution using Siemens PLM, STAR-CCM+, version 15 [37]

B.1 Step 1: Load Simulation With A Pre Determined Flow Field

The first step is to load an existing simulation. Make sure that you have already simulated velocity and pressure field either using a steady or unsteady solver. As seen in Figure B.1 We have already loaded an existing simulation. Just for the illustration purposes we have used a coarse grid A to evaluate mean age distribution for a flow corresponding to Reynolds of 12000. As you can see that the velocity and pressure field were determined prior to the evaluation of mean age distribution.

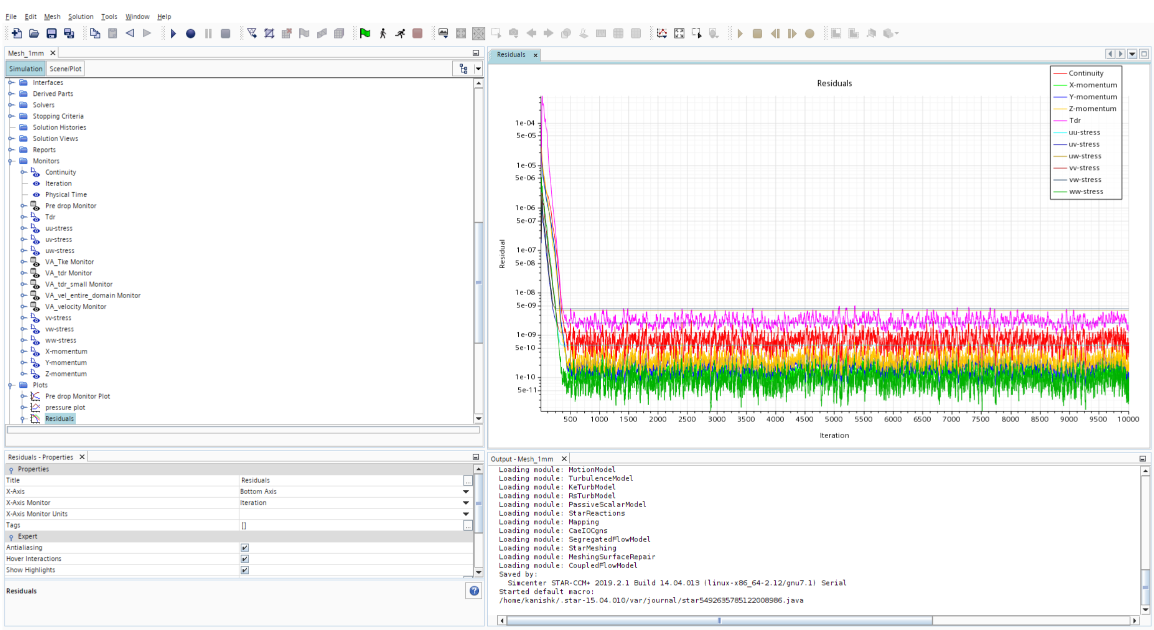

Figure B.1: Showing residuals of the simulation that is loaded into Starccm+.

B.2 Step 2: Setting Up Passive Scalar

The starccm+ provides an inbuilt physics model to simulate a passive scalar. Double click on the *model* under the *physics* node as shown in Figure B.2. A box with a list of different models will appear. From this box select the *Passive Scalar* model, if previously not selected.

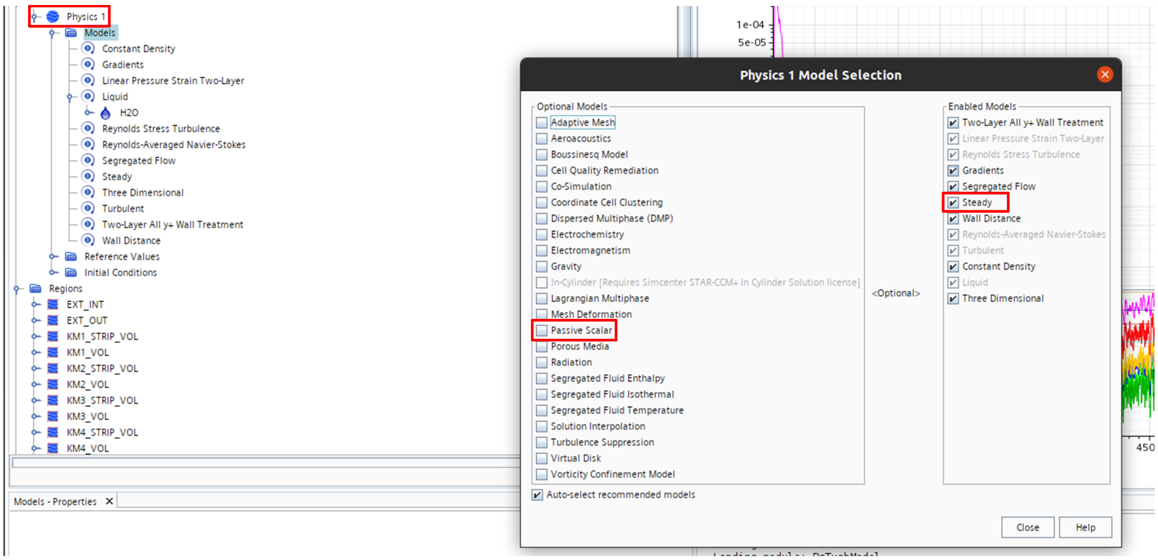

Figure B.2: Selecting a new Passive Scalar model.

Once selected close the pop up box. Once done, you will find a new *Passive Scalar* node under the *Models* node in *Physics 1*. Right click on the *Passive Scalar* and create a new passive scalar named *Mean Age*. See Figure B.3.

Once created the new *Mean Age* scalar node under the *Passive Scalar* node, set the values of Molecular Diffusivity and the Turbulent Schmidt Number to 10^9.

B.3 Step 3: Setting Up Source Term For Passive Scalar Equation

A closer look at the Equation 2.14 reveals that it differs from the convection-diffusion equation only because of a constant source term value set to unity for the case of Equation 2.14. To make passive scalar equation imitate the mean age equation (refer to 2.14) we need to specify a constant source term equal to unity.

For doing so under the regions node, for all the fluid regions change the *Passive Scalar Source Option* under the *Physics Conditions* from *No source active* to *Scalar flux with inferred density* (see Figure B.4). Once the *Source Definition* is defined, set the value of *Passive Scalar Source Density Inferred* under the *Physics Values* node to unity, as shown in Figure B.5.

Make sure that you set the value of source for all the fluid regions in the computational domain.

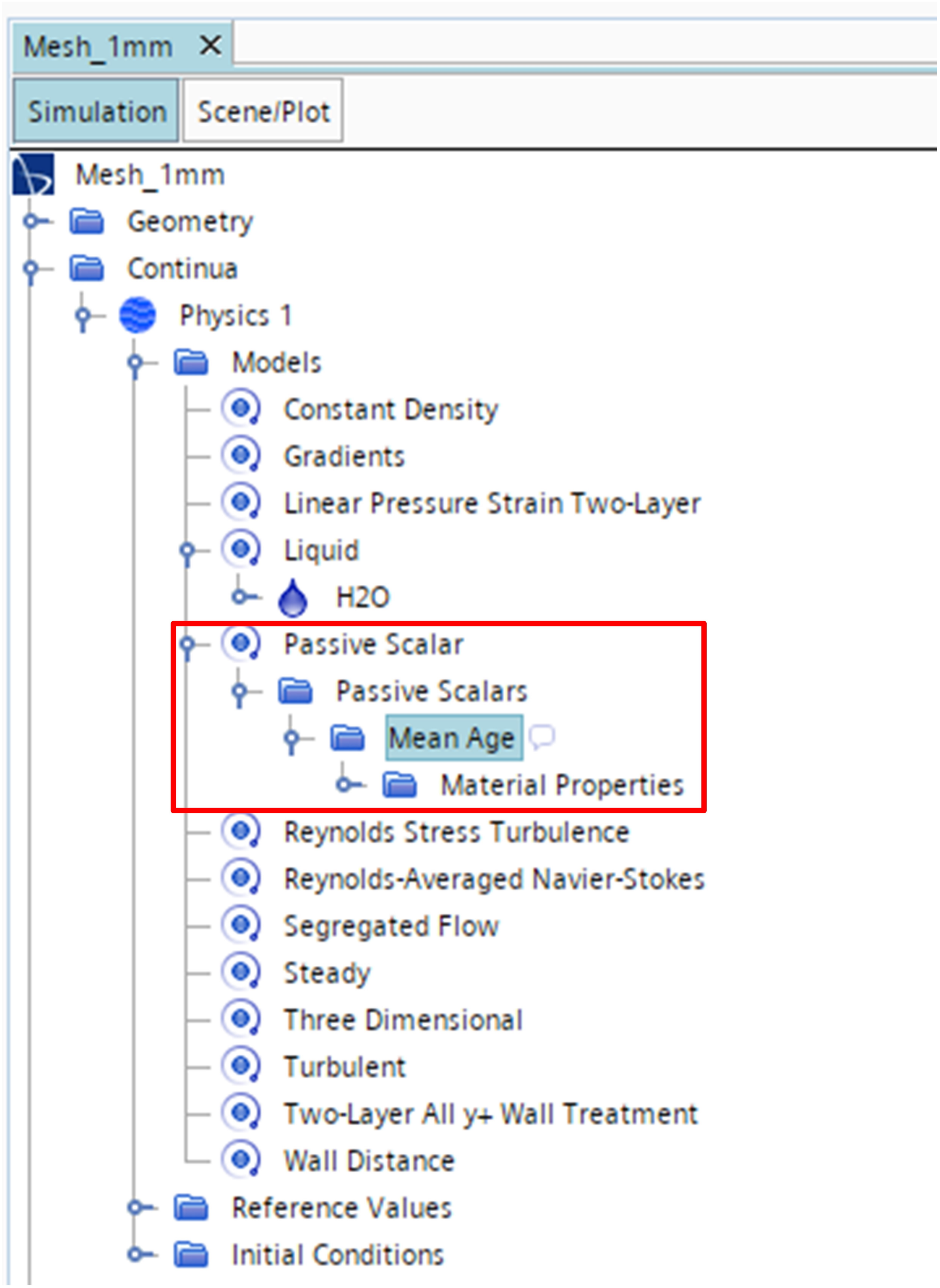

Figure B.3: Creating a new passive scalar for the simulation.

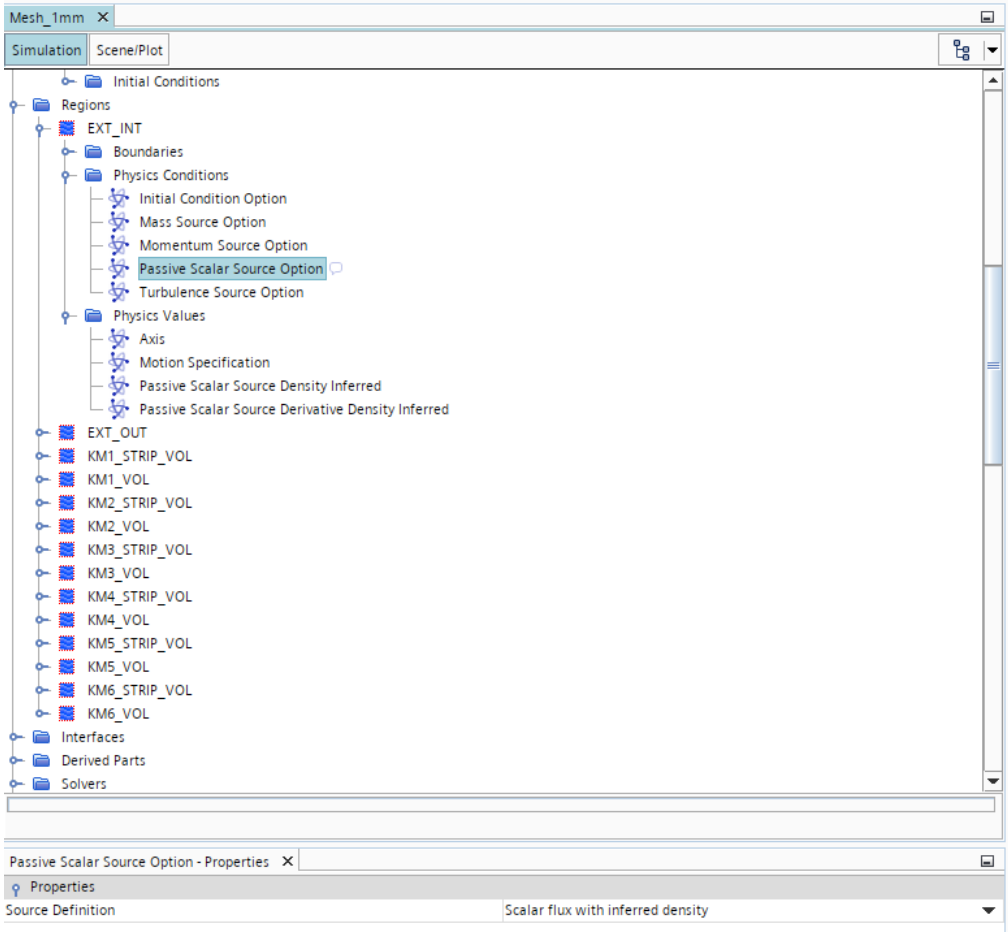

Figure B.4: Changing source definition to mimic mean age equation.

B.4 Step 4: Evaluating Mean Age Distribution

Once everything is setup, click the green flag on the top center to run the simulation. The *Mean Age* residual will show up in the viewer beside. As shown Figure B.6

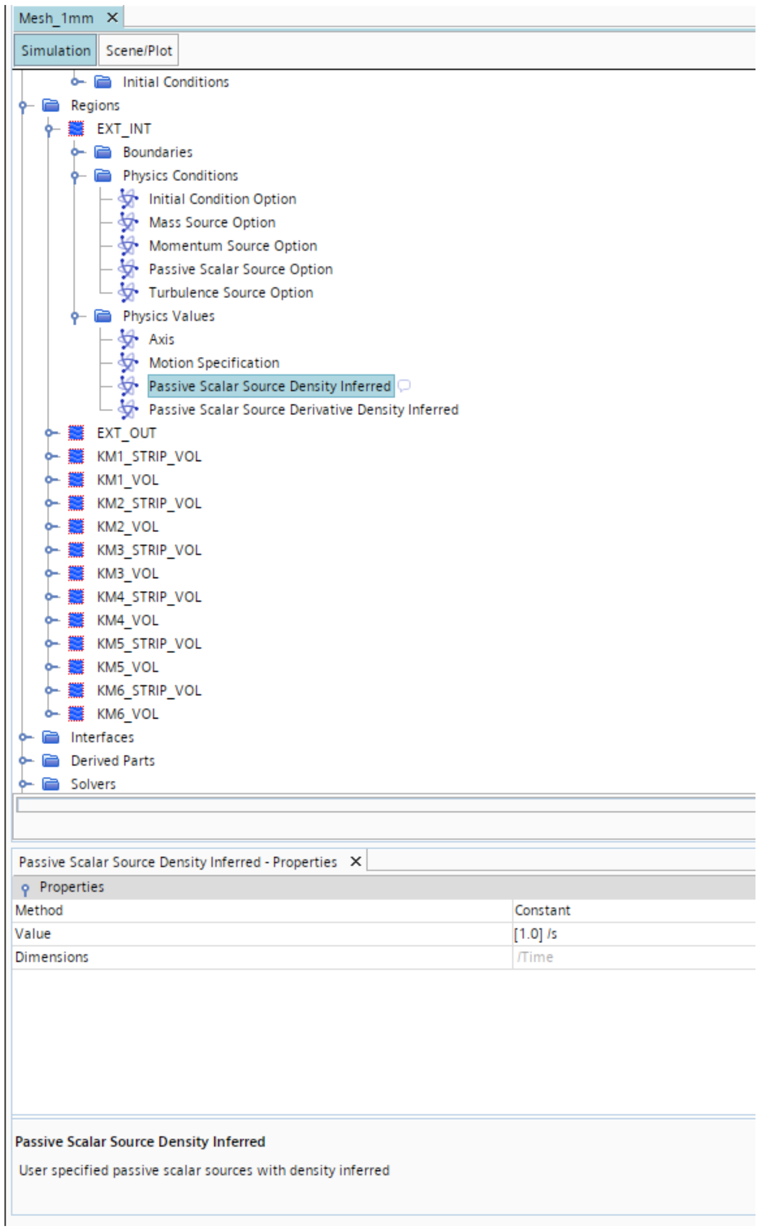

Figure B.5: Setting the value of source term to unity.

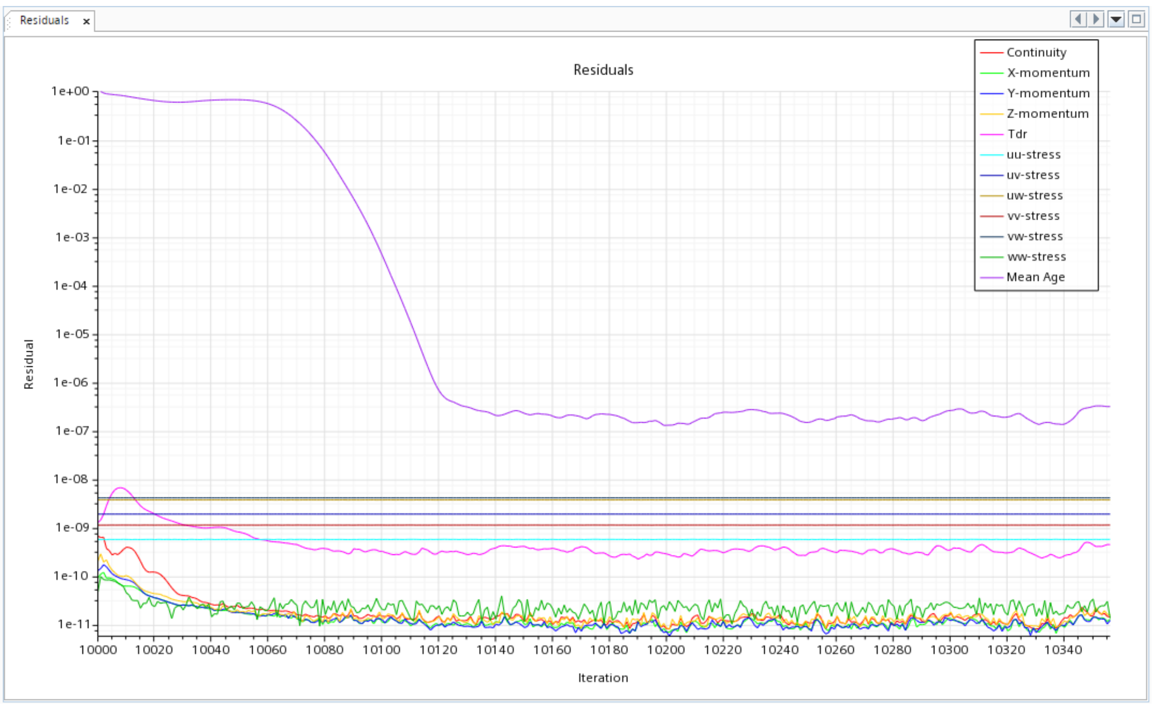

Figure B.6: Residual of mean age equation.